La Rivista del Nuovo Cimento (2022) 45:661–736
https://doi.org/10.1007/s40766-022-00036-z

REVIEW PAPER

Hydrodynamic approach to two-dimensional electron systems

Boris N. Narozhny[1,2]

Received: 30 March 2022 / Accepted: 22 May 2022 / Published online: 14 July 2022

Abstract
The last few years have seen an explosion of interest in hydrodynamic effects in interacting electron systems in ultra-pure materials. One such material, graphene, is not only an excellent platform for the experimental realization of the hydrodynamic flow of electrons, but also allows for a controlled derivation of the hydrodynamic equations on the basis of kinetic theory. The resulting hydrodynamic theory of electronic transport in graphene yields quantitative predictions for experimentally relevant quantities, e.g., viscosity, electrical conductivity, etc. Here I review recent theoretical advances in the field, compare the hydrodynamic theory of charge carriers in graphene with relativistic hydrodynamics and recent experiments, and discuss applications of hydrodynamic approach to novel materials beyond graphene.

Keywords Hydrodynamics · Kinetic theory · Electronic transport · Viscosity · Hall effect · Graphene · Compensated semimetals · Topological materials

1 Hydrodynamics and condensed matter

Collective excitations in solid-state physics—phonons, magnons, plasmons, etc.—are often considered in the long-wavelength (small wavevector) limit with the corresponding observables describing long-distance properties of matter. One way to develop a macroscopic theory reflecting such physics [1] is to combine continuity equations (manifesting conservation laws) with thermodynamic arguments to identify how the entropy of the system responds to local density fluctuations of the conserved quantities. Requiring the total entropy production rate to be non-negative, one may establish

✉ Boris N. Narozhny
boris.narozhny@kit.edu

1 Institut for Theoretical Condensed Matter Physics, Karlsruhe Institute of Technology, 76128 Karlsruhe, Germany

2 National Research Nuclear University MEPhI (Moscow Engineering Physics Institute), 115409 Moscow, Russia

the "constitutive relations" between the macroscopic currents and the external bias. Closing the equations with the help of the thermodynamic relations one can complete the description of the long-wavelength dynamics of the system. The resulting theories are macroscopic since their variables are densities of physical quantities and the corresponding currents. They are also phenomenological since they provide no means of calculating the coefficients in the constitutive relations (i.e., the "generalized susceptibilities"). Such approach is justified at distances that are much larger than any length scales corresponding to the underlying "microscopic" scattering processes, the condition that is very often satisfied in experiments.

The most common equation describing the long-wavelength dynamics in solids is the diffusion equation [1]. In the simplest example, spin diffusion [2, 3] arises in a system of spin-1/2 particles with a velocity- and spin-independent interaction leaving the total magnetization conserved. This behavior has been observed experimentally (see, e.g., Ref. [4]) and is generally expected to be applicable to a wide variety of spin systems (with the possible exception of one-dimensional integrable models, see Refs. [5–8]).

Low-temperature charge transport is also often considered to be diffusive [9]. In the simplest case, charge carriers are assumed to be independent and non-interacting, so that their total number is a conserved quantity, while the dominant relaxation process is the electron–impurity scattering described by the transport mean free time, τ. The latter defines both the diffusion constant and electrical conductivity [10] and is still one of the most important quantities characterizing conductive properties of experimental samples. The diffusive behavior is commonly expected to take place in real metals and semiconductors as long as the sample size is large compared to the mean free path (typically, $\ell = v_F \tau$ with v_F being the Fermi velocity) [11] and at low temperatures, $T\tau \ll 1$ [12] (the units with $\hbar = k_B = 1$ are used throughout this paper).

A common feature of the above theories is the decaying (diffusive) nature of collective modes (defined as the normal modes of the set of linearized macroscopic equations). In contrast, the collective modes in conventional fluids, both classical (e.g., water [13, 14]) and quantum (e.g., ^{3}He [15]), include also sound waves (with the linear dispersion). This crucial difference can be attributed to the momentum conservation. Indeed, the usual description of a fluid (or a gas, see [16]) assumes a system of "particles" (molecules or atoms) interacting by means of local collisions. In the simplest case (of a single-component, monoatomic fluid) the collisions preserve momentum, and hence overall there are three global conserved quantities—the number of particles, energy, and momentum. If, moreover, Galilean invariance is assumed, then the current is defined by the momentum, which is the key point ultimately leading to the existence of the sound-like collective mode.

The macroscopic theory describing the flow of a conventional fluid—namely, hydrodynamics—can be derived in the several ways. One can follow the above prescription using the continuity equations and entropy [1], one can "guess" (or postulate) the constitutive relations based on the Galilean invariance (or, in the relativistic case, Lorentz invariance) [13], or one can use the "microscopic" kinetic theory [16]. The latter approach is justified, strictly speaking, in a dilute gas, but yields the same set of hydrodynamic equations as the more phenomenological methods. This fact is typically attributed to the *universality* of the hydrodynamic approach: the belief that

long-distance properties are largely independent of the short-distance (microscopic) details. As a result, strongly interacting fluids (such as water) can be successfully described by the same hydrodynamic theory as an ideal gas [16].

In condensed matter context, hydrodynamic approaches have been applied to phonons [17] (also see the recent experiment [18] and references therein) and magnons [19], while applications to electronic systems [20–22] have only recently attracted widespread attention [23–25]. This may appear surprising, after all the Fermi Liquid theory originally developed for ^{3}He [15] has become a dominant paradigm in solid-state physics. In ^{3}He, the Fermi Liquid theory can be used to derive the hydrodynamic equations [26], so why cannot the same be done in solids? Unlike helium atoms, electrons in solids exist in the environment created by a crystal lattice and can scatter off both lattice imperfections (or "disorder") and lattice vibrations (phonons). In both cases, their momentum is not conserved. As a result, the electron motion is typically diffusive [9], unless the sample size is smaller than the mean free path and the system is "ballistic" [11]. For most typical scattering mechanisms in solids, the mean free path is strongly temperature dependent. In conventional metals [10], electron–impurity scattering dominates at low temperatures, leading to, e.g., the residual resistance. At high temperatures, the main scattering mechanism is the electron–phonon interaction. In many materials, at least one of these two mechanisms is more effective than electron–electron interaction at any temperature, leaving no room for hydrodynamic behavior. In terms of the associated length scales, this statement can be formulated as $\ell_{ee} \gg \ell_{\rm dis}, \ell_{e-ph}$ (in the self-evident notation). If a material would exist, where the opposite condition were satisfied at least in some temperature range, then one would be justified in neglecting momentum non-conserving processes and applying the hydrodynamic theory. For a long time such a material was not known. In recent years, several extremely pure materials became available bringing electronic hydrodynamics within experimental reach [27–36].

2 Experimental signatures of hydrodynamic behavior

The parameter regime supporting the hydrodynamic behavior can be readily found in systems where the temperature dependence of key length scales (ℓ_{ee}, $\ell_{\rm dis}$, ℓ_{e-ph}, etc.) is sufficiently different. This may happen, for example, in two-dimensional (2D) systems where the electron–electron scattering length varies with temperature as $\ell_{ee} \sim T^{-2}$ (within the typical Fermi Liquid description), while the contribution of acoustic phonon scattering to the electronic mean free path varies as $\ell_{e-ph} \sim T^{-1}$. At the same time, the low-temperature values of ℓ_{ee} are easily surpassed by the mean free path $\ell_{\rm dis}$ in ultra-pure samples. Hence, 2D systems may offer an intermediate temperature window [23, 24, 37, 38], where electron–electron interaction is the dominant scattering process and hence appear to be plausible candidates to support the hydrodynamic behavior. It is then not surprising that many experiments on electronic hydrodynamics were focusing on 2D systems and especially on graphene. The latter is a particularly convenient material [27, 28, 39–43] where the mean free path remains long up to room temperatures, $\max[\ell_{\rm dis}, \ell_{e-ph}] > 1\,\mu$m. At the same time, at $T \geq 150$ K the electron–electron scattering length decreases to $\ell_{ee} \approx 0.1 \div 0.3\,\mu$m. Since the pioneering work

on the nonlocal resistance [27] and Wiedemann–Franz law violation [28], several impressive experiments [39, 41–45] aimed at uncovering the hydrodynamic behavior of the electronic system in graphene. In particular, it was suggested that a viscous hydrodynamic flow in electronic systems might exhibit enhanced, higher-than-ballistic conduction [39, 44, 45]. More recently, several breakthrough experiments [30, 34, 44–54] demonstrated various distinct imaging techniques making it possible to "observe" the electronic flow in graphene "directly".

Hydrodynamic flow of electrons in solids should be observable not only in graphene, but in any material that is clean enough to satisfy the condition that the electron–electron scattering length is much shorter than the disorder mean free path. In particular, modern semiconductor technology allows fabricating ultra-high-mobility heterostructures [30, 32, 36, 55–57], a noticeable improvement since the original observation of the Gurzhi effect [58].

At the same time, the hydrodynamic behavior might be observable in a wide range of novel materials including the 2D metal palladium cobaltate [29], topological insulators (where the conducting surface states may exhibit hydrodynamic behavior), and Weyl semimetals [59, 60]. The latter systems have attracted considerable attention since they exhibit a solid-state realization of the Adler–Bell–Jackiw chiral anomaly [61–65]. One of the hallmark manifestations of the anomaly in Weyl systems [59, 66] is the recently observed negative magnetoresistance [64, 67]. Observation of relativistic Weyl hydrodynamics in these systems is the next milestone in the field.

2.1 Gurzhi effect

In his pioneering work [17, 20, 21], Gurzhi considered an idealized problem of the electric current flowing in a thin, clean wire. In this case, there are two competing scattering processes: the electron scattering off the walls of the wire (i.e., system boundaries) and the electron–electron interaction, either direct or effective (e.g., phonon-mediated). Assume that at the lowest temperatures, the electron–electron scattering length is longer than the width of the wire, $\ell_{ee} \gg d$. Then boundary scattering will dominate leading to the approximately temperature-independent resistivity, $\rho \sim 1/d$. Now, the electron–electron scattering length ℓ_{ee} is inversely proportional to some power of temperature (for the direct electron–electron interaction $\ell_{ee} \propto T^{-2}$ [20], while for the phonon-mediated interaction $\ell_{ee} \propto T^{-5}$ [21], see Fig. 1). As the temperature increases, ℓ_{ee} will eventually become smaller than d. In the limit $\ell_{ee} \ll d$, the resistivity will be determined by the electron–electron scattering, $\rho \sim \ell_{ee}/d^2$ [20, 21] and hence will decrease with the increasing temperature. This effect can be seen as the electronic analogy of the crossover between the Knudsen (molecular) flow and the Poiseuille (viscous) flow in a rarefied gas driven through a tube [68].

The above conclusion crucially depends on the assumption that the effective mean free path d^2/ℓ_{ee} is much smaller than the length scale $\ell_{\rm dis}$ describing bulk momentum-relaxing processes (i.e., electron–impurity or electron–phonon scattering). Then the electronic momentum is approximately conserved and one can introduce the hydrodynamic description (the expression for ρ follows from the standard expression for the kinematic viscosity, $\nu = v_F \ell_{ee}/3$ [20]).

Once the effective mean free path due to electron–electron interaction exceeds the disorder scattering length, $d^2/\ell_{ee} \gg \ell_{\rm dis}$, the system becomes diffusive and the resistivity resumes its usual growth with temperature. Hence, $\rho(T)$ is expected to exhibit a minimum, see Fig. 1, the result now known as the Gurzhi effect.

A direct observation of the Gurzhi effect in metals is hindered by several factors: in addition to the electron–impurity and electron–phonon scattering, Umklapp scattering, nonspherical Fermi surface shapes, or Kondo effect may all contribute to the temperature dependence of the resistivity. An elegant way around these obstacles was suggested by de Jong and Molenkamp [58]. They used 2D wires defined electrostatically in the two-dimensional electron gas (2DEG) in semiconductor (GaAs/AlGaAs) heterostructures. Given the weakness of the electron–phonon coupling in this system, it was possible to control the electronic temperature selectively without changing the temperature of the whole sample by passing a *dc* current. The resulting measurement exhibited a minimum in the differential resistance as a function of the current, see Fig. 1, which was argued to be equivalent to the Gurzhi effect. More recently, the observed decrease of resistivity with increasing temperature typical of the Gurzhi effect ($\rho \sim T^{-2}$) was reported in Ref. [32].

2.2 Nonlocal transport measurements

The "modern era" in electronic hydrodynamics was announced in the three back-to-back Science papers in 2016 reporting the negative vicinity resistance [27] and Wiedemann–Franz law violation [28] in graphene, as well as hints of the hydrodynamic behavior in [29] in $PdCoO_2$. These groundbreaking experiments opened the door for further studies focusing on unconventional aspects of electronic transport in ultra-pure materials.

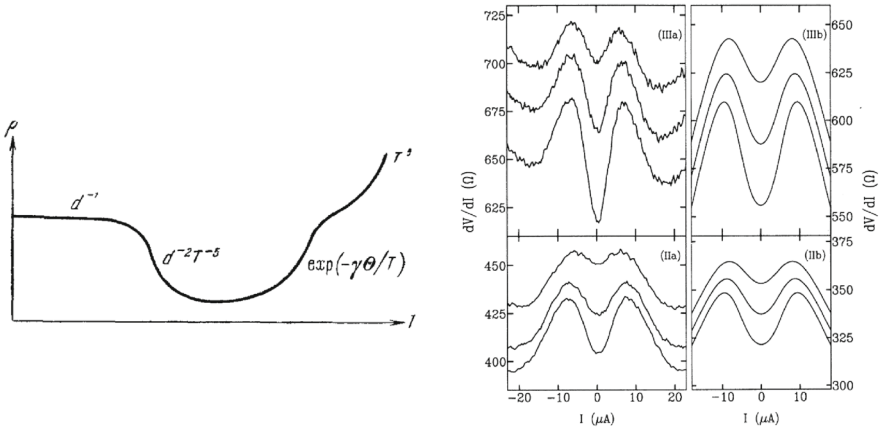

Fig. 1 Gurzhi effect. Left panel: a sketch of the theoretically predicted resistance minimum (reprinted with permission from Ref. [17]; copyright (1968) Uspekhi Fizicheskikh Nauk). Right panel: experimental (IIa and IIIa) and theoretical (IIb and IIIb) differential resistance dV/dI as a function of the current I at the lattice temperatures $T = 4.5,\ 3.1,\ 1.8$ K, from top to bottom (reprinted with permission from Ref. [58]; copyright (1995) by the American Physical Society)

Conventional experiments aimed at uncovering inner workings of solids often rely on transport measurements [10, 16], the tool that proved to be indispensable throughout the history of condensed matter physics. In a traditional experiment one measures a current–voltage characteristic and extracts linear response functions determined by properties of the unperturbed system. A basic quantity that can be measured in this way is the Ohmic resistance R. At the simplest level, R can be described by the Drude theory [10, 71], which essentially amounts to writing down classical equations of motion of charge carriers in applied electric and magnetic fields with a phenomenological friction term.

A more intricate question concerns the spatial distribution of the electric current density, which is most relevant in small samples (chips) with multiple leads. Here the current density may exhibit complex patterns depending on the external bias, electrostatic environment, chip geometry, and magnetic field. One way to detect such patterns is provided by nonlocal transport measurements [72–78], i.e., by measuring voltage drops between various leads that are spatially removed from the source and drain, see Fig. 2. These techniques were devised to study ballistic propagation of charge carriers in mesoscopic systems, but recently they were applied to investigate possible hydrodynamic behavior in ultra-pure conductors [23, 24, 27, 41, 42].

Nonlocal resistance measurements have also been used to study edge states accompanying the quantum Hall effect [70, 79–83]. While the exact nature of the edge states has been a subject of debate, the nonlocal resistance, R_{NL}, appears to be an intuitively clear consequence of the fact that the electric current flows along the edges of the sample. Such a current would not be subject to exponential decay [69] exhibited by the bulk charge propagation leading to a much stronger nonlocal resistance.

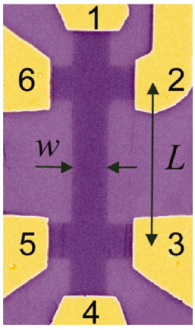

Fig. 2 Hall bar geometry for nonlocal transport measurements. Traditional four-terminal measurement involves passing a current between leads 1 and 4, while measuring the voltage drop between leads 2 and 3. The resulting resistance $R_{23,14} = V_{23}/I_{14}$ is related to the longitudinal resistivity, $\rho_{xx} = R_{23,14}W/L$, where W and L are the width and length of the Hall bar. In contrast, a nonlocal measurement consists of passing a current between, e.g., 2 and 6, while measuring the voltage between leads 3 and 5. In the case of usual diffusive transport, such voltage should be exponentially suppressed [69], $R_{NL} = R_{35,26} \sim \rho_{xx} \exp(-\pi L/W)$. (From Ref. [70]. Reprinted with permission from AAAS)

2.2.1 Giant nonlocality in magnetic field

While traditional studies of electronic transport tended to focus on low temperatures, more recent experimental work has been gradually shifting towards measurements at nearly room temperatures [27, 41, 42, 70, 77]. A detailed analysis of the nonlocal resistance in a wide range of parameters (temperatures, carrier densities, and magnetic fields) was performed in Ref. [70] using graphene samples.

At low temperatures and in strong magnetic fields, graphene exhibits the quantum Hall effect (QHE) with well-defined plateaus in Hall resistivity corresponding to regions of the carrier density where $\rho_{xx} = 0$. At the same densities, the nonlocal resistance also remains zero, but in between the QHE zeros may reach values as high as 1 kΩ. At high temperatures, all but one such peaks disappear. The remaining peak at charge neutrality exhibits behavior that appears to be inconsistent with the QHE interpretation. In particular, the strong signal persists at near room temperatures, way beyond the QHE regime with the peak value $R_{NL} \approx 1.5\,\mathrm{k\Omega}$ at $B = 12\,\mathrm{T}$ and $T = 300\,\mathrm{K}$, three times higher than that at $T = 10\,\mathrm{K}$, see Fig. 3.

The unexpected "giant" nonlocality in neutral graphene was originally explained by diffusion of the mismatched spin-up and spin-down quasiparticles in the presence of the Zeeman splitting [70]. This interpretation was disputed in Ref. [84] where the effect was not observed in the nearly parallel field (the Zeeman splitting is independent of the field direction). Moreover, the magnitude of the effect proposed in Ref. [70] was disputed in Ref. [85], where the residual quasiparticle density due to Zeeman splitting (at $T = 0$ and $B = 10\,\mathrm{T}$) was estimated to be $\rho_Q \approx 2.2 \times 10^6\,\mathrm{cm}^{-2}$ leading to a nonlocal resistance that is much weaker than the data of Ref. [70].

The alternative explanation suggested in Ref. [85] was based on the "two band" phenomenology of the electronic system in neutral graphene [86–88]. Indeed, at the charge neutrality point, the conductance and valence bands in graphene touch. At finite temperatures, both bands contain mobile carriers leading to a two-component nature

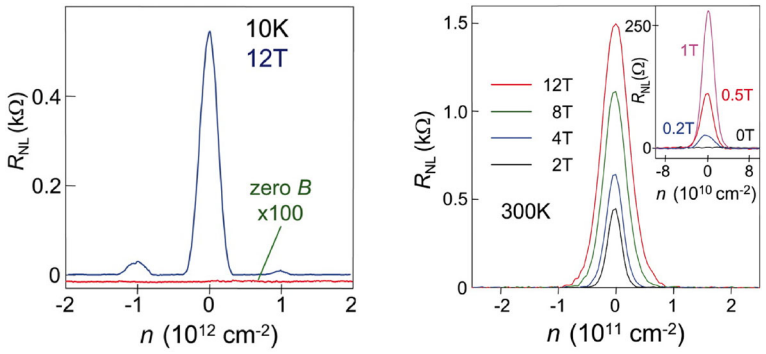

Fig. 3 Nonlocal resistance in graphene. Left panel: QHE regime at $T = 10\,\mathrm{K}$ and $B = 12\,\mathrm{T}$ (the red curve indicates that no signal could be detected at $B = 0$ within the experimental resolution; the curve is downshifted for clarity and magnified). Right panel: high-temperature regime, $T = 300\,\mathrm{K}$. (From Ref. [70]. Reprinted with permission from AAAS)

of the electronic system. Given the exact particle–hole symmetry at neutrality, this system is "compensated" and hence there is no classical Hall effect, such that the bulk Hall conductivity vanishes, $\rho_{xy} = 0$, and the longitudinal conductivity is unaffected by the magnetic field. In contrast, the same approach yields the nonlocal response that is strongly field dependent. Indeed, the presence of two types of carriers (electrons and holes) leads to the existence of two macroscopic currents: the electric current $\boldsymbol{J}$ and the total quasiparticle (or "imbalance" [89]) current $\boldsymbol{j}_I$,

$$\boldsymbol{j} = \boldsymbol{j}_e - \boldsymbol{j}_h, \qquad \boldsymbol{j}_I = \boldsymbol{j}_e + \boldsymbol{j}_h, \qquad \boldsymbol{J} = e\boldsymbol{j}, \tag{1}$$

where $\boldsymbol{j}_{e(h)}$ is the electron (hole) current and e is the electron charge. In the absence of the magnetic field, the neutral current $\boldsymbol{j}_I$ is decoupled from $\boldsymbol{J}$ and is practically undetectable (it does not couple to the electric field). The electrons and holes are drifting in parallel, but opposite directions. However, the magnetic field bends the quasiclassical trajectories of charge carriers coupling the two currents and turning $\boldsymbol{j}_I$ in the direction that is orthogonal to $\boldsymbol{J}$. Now the neutral current can transport charge carriers to distant parts of the sample, where a nonlocal response is induced, again, by the magnetic field, see Sect. 4 for more details.

The arguments of Ref. [85] yield the nonlocal response capturing the main qualitative features of the effect observed in Ref. [70]. Quantitatively, these results are consistent with the rapid decay of the nonlocal signal away from the neutrality point, but overestimate the magnitude of the effect. The latter discrepancy was attributed to the simplicity of the model that did not take into account the effects of electron–electron interaction contributing to resistivity of neutral graphene, the residual carrier population at neutrality due to fluctuations of the electrostatic potential [84], and viscous phenomena, all of which are expected to suppress R_{NL}.

Viscous effects are of particular interest in the context of electronic hydrodynamics and may also lead to nonlocality. However, these effects are expected to occur in the absence of magnetic field as well and in graphene are most pronounced away from charge neutrality.

2.2.2 Negative vicinity resistance

Away from charge neutrality, i.e., when the chemical potential exceeds the temperature, $\mu \gg T$, electrons in graphene are typically expected to behave similarly to 2DEG in semiconductor heterostructures. The contribution of the valence band is exponentially suppressed and the electronic system comprises only the single component. In that case, a Fermi liquid is expected to behave hydrodynamically [26], the issue with the electronic systems being whether the material is pure enough.

Assuming the hydrodynamic regime is possible, the single-component electronic system should obey the Navier–Stokes-like equation [13, 90–92] with an additional damping due to disorder scattering [21], as well as the continuity equation. Within linear response and in the static limit, these equations can be written as (see, e.g., Sect. 3)

$$e\boldsymbol{E} = -m\nu\Delta\boldsymbol{u} + m\boldsymbol{u}/\tau_{\rm dis}, \qquad \nabla\boldsymbol{u} = 0, \tag{2}$$

where $\boldsymbol{u}$ is the hydrodynamic velocity, ν is the kinematic viscosity, and m is the effective mass (in graphene this should be replaced by μ/v_g^2, with μ being the chemical potential and v_g the velocity of the Dirac spectrum). The electric current is expressed in terms of the hydrodynamic velocity as

$$\boldsymbol{j} = n\boldsymbol{u}, \tag{3}$$

where n is the carrier density, see also Eq. (1).

The resulting behavior of the current density is determined by the relative strength of the viscosity and disorder scattering, which can be expressed in terms of the dimensionless "Gurzhi number" (note that this definition is written in analogy to the Reynolds number [13] and is the inverse of the number defined in Ref. [93])

$$\mathrm{Gu} = \frac{l^2}{\nu\tau_{\mathrm{dis}}}, \tag{4}$$

where l is the typical length scale of the problem. Large values of Gu indicate that the disorder scattering dominates (such that the current density exhibits patterns typical to the traditional diffusive behavior), whereas small values of Gu correspond to the hydrodynamic viscous flow [93–98].

In confined geometries, viscous flows may be accompanied by vortices (or whirlpools) [93–96], which may be detected by observing *negative* nonlocal resistance by placing the leads on the opposite sides of a vortex. This idea was realized in the pioneering experiment of Ref. [27]. Here (unlike the measurement in Ref. [70]) the leads were placed close to each other (based on the expected vortex size), see Fig. 4, hence the measured quantity was referred to as "vicinity resistance".

In agreement with the expectation that the hydrodynamic behavior should occur at intermediate temperatures, the measured vicinity resistance is negative roughly between 70 K and 250 K (with the actual range being density dependent), see Fig. 4. This observation was supported in Ref. [27] by a solution to the above equations (2) showing formation of a vortex close to the leads. Similar theoretical results were reported in Refs. [93–96], see also Ref. [99].

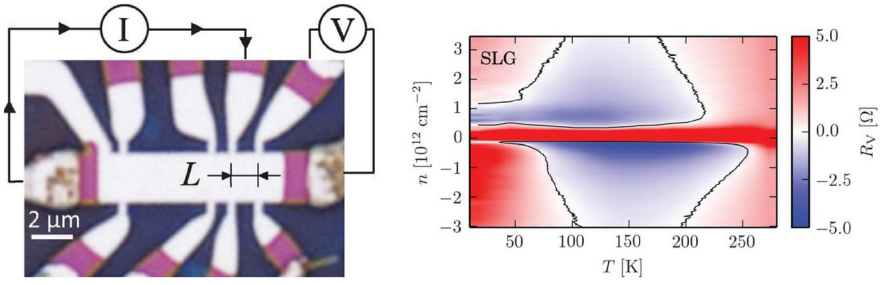

Fig. 4 Negative vicinity resistance in graphene. Left panel: multi-lead device with the measurement schematic. Right panel: color map showing a wide, intermediate temperature range where the vicinity resistance is negative (From Ref. [27]. Reprinted with permission from AAAS)

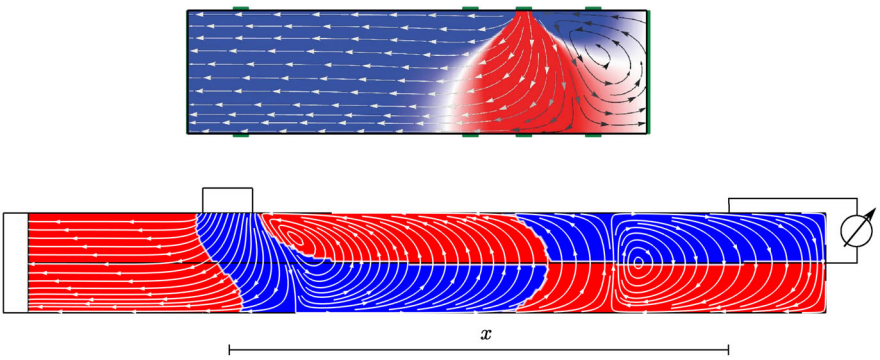

Fig. 5 Vorticity in electronic flows in graphene. Top panel: simulated flow in the experimental device shown in Fig. 4 (from Ref. [27]. Reprinted with permission from AAAS). Bottom panel: double vortex in a long device suggested in Ref. [93]. The red and blue colors indicate the alternating sign of the deviation of the electrochemical potential from its median value. (Reprinted with permission from IOP Publishing)

Despite the apparent agreement between theory and experiment, observation of the negative vicinity resistance does not represent the proverbial "smoking gun" proving that the system is in fact in the hydrodynamic regime. The reason is that ballistic systems may also exhibit negative nonlocal resistance [51] as has been shown both experimentally [77] and theoretically [100]. This issue has been specifically studied in Ref. [41], where it was shown that in addition to being negative, the vicinity resistance has to grow with temperature (the crossover from the ballistic to hydrodynamic behavior was identified with the minimum in the vicinity resistance as a function of temperature). More recently, Ref. [93] reported a numerical solution to the hydrodynamic equations (2) showing the existence of multiple vortices in long samples, see Fig. 5. Since the vorticity of the adjacent vortices has the opposite sign, placing multiple leads along the sample and measuring the voltage as a function of distance from the source electrode should yield a *sign-alternating nonlocal resistance* which should in principle distinguish the ballistic and hydrodynamic behavior. Alternatively, one could try to use one of the novel imaging techniques [50–53] to observe vortices "directly".

2.3 Hydrodynamic flow around macroscopic obstacles

The collective hydrodynamic flow is expected to differ strongly from the single-particle ballistic motion in systems with macroscopic obstacles. Whereas particles tend to scatter off anything they may encounter—sample boundaries, other geometrical features, or long-range potentials, a viscous fluid tends to avoid obstacles by flowing around them. As a result, the collective flow maybe more efficient in carrying the constituent particles through the system in question. In the context of the traditional hydrodynamics of rarefied gases, this fact has been established already by Knudsen [68]. In the context of electronic hydrodynamics, this issue was first addressed theoretically in Ref. [101] and experimentally in Ref. [39].

2.3.1 Superballistic transport

One of the most common types of "obstacles" studied in the context of electronic transport is a constriction (or a point contact). This object was extensively studied in mesoscopic physics [11], with the conductance quantization [102, 103] being the hallmark effect. In particular, it was established that ballistic propagation of charge carriers through a point contact yields the conductance that is constrained by a fundamental upper bound [104].

Quantization of the point contact conductance can be understood by considering one-dimensional (1D) subbands in the constriction of the width W (corresponding to the quantized values of the transverse momentum, $k_y = \pm\pi n/W$). Each subband contributes equally to the conductance due to the cancellation of the group velocity and the 1D density of states (DoS) [11]. Observing that the number of the occupied subbands is naturally an integer, one finds that the total conductance is quantized, $G_b = 2Ne^2/h$. In the classical limit, the number of propagating (Landauer) channels in 2D can be estimated as $N = [k_F W/\pi]$ (square brackets indicate the integer value), yielding the upper bound known as the Sharvin limit [11, 104].

The above argument neglects electron–electron interaction and is justified when the corresponding scattering length is large compared to the width of the constriction, $\ell_{ee} \gg W$. In the hydrodynamic regime, $\ell_{ee} \ll W$, electrons move collectively avoiding the boundaries and thus may carry the charge through the point contact more effectively than free fermions (i.e., achieving conductance higher than G_b, see Fig. 6). Indeed, the solution to the hydrodynamic equations describing the electron flow through a simplest 2D constriction reported in Ref. [101] yields the conductance

$$G_h = \frac{\pi e^2 n^2 W^2}{32\eta}, \tag{5}$$

where η is the shear viscosity. Since G_h grows with width faster than G_b, there is a possibility for the "superballistic" conduction for wide enough channels.

The theoretical expectation ($G_h > G_b$) was first confirmed in the experiment of Ref. [39], see Fig. 6, and more recently corroborated in Ref. [44], where a novel imaging technique was applied to the point contact problem (see Sect. 2.4), see also Ref. [45]. The theory of Ref. [101] was revisited and expanded upon in Ref. [37], where the same hydrodynamic equation was solved for the current density profile. The authors of Ref. [37] also analyzed the intermediate parameter regime where hydrodynamic flows could be realistically observed. Heating effects in similar inhomogeneous flows were analyzed in Ref. [105].

2.3.2 Flows around macroscopic obstacles

The transition from the Ohmic to hydrodynamic flow observed in the point contact geometry in Refs. [39, 44] is similar to the transition between the Knudsen and Poiseuille flows [17, 58, 68]. The tendency of the viscous flow to avoid obstacles is well known in hydrodynamics and is illustrated in Fig. 7. However, a naive solution of

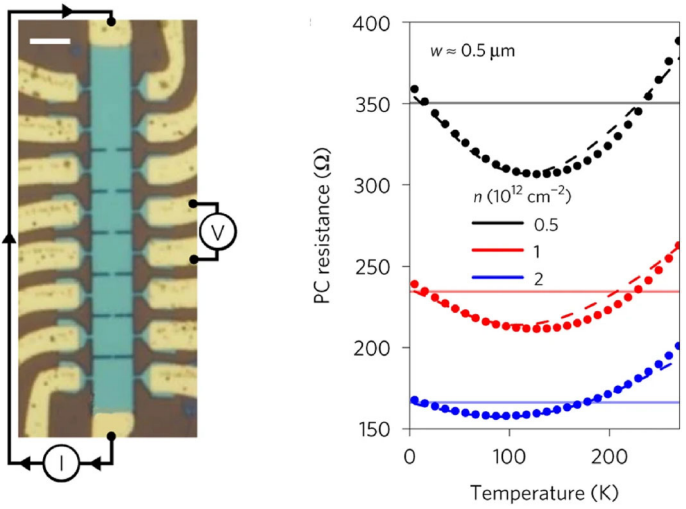

Fig. 6 Superballistic transport in graphene. Left panel: a typical measuring device showing multiple point contacts varying in width from $W = 0.1$ to $W = 1.2\,\mu$m. Right panel: point contact resistance for a $W = 0.5\,\mu$m constriction at representative carrier densities. The experimental data are represented by dots, while the horizontal lines indicate the Sharvin limit of the maximum classical ballistic conductance. Lower-than-the-limit resistance at intermediate temperatures is indicative of the collective, viscous flow of electrons. (From Ref. [39]. Reprinted with permission from Springer Nature)

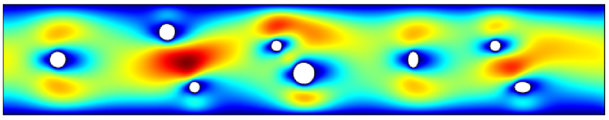

Fig. 7 Numerical simulation of the Poiseuille flow in a 2D channel with randomly placed macroscopic obstacles (represented by white shapes). The color map indicates the magnitude of the flow velocity (ranging from zero shown in blue to the maximum shown in dark red)

the hydrodynamic equations in a 2D system with macroscopic obstacles within linear response leads to the so-called "Stokes paradox" [13, 14, 32, 106, 107].

The problem of a motion of a spherical object through an otherwise stationary viscous fluid (or equivalently, viscous flow around a stationary sphere subject to the condition of constant flow velocity at infinity) is a classic problem in hydrodynamics [13, 14, 92]. For flows characterized by small Reynolds numbers, one may neglect the nonlinear term in the Navier–Stokes equation [13, 90, 91] and solve the resulting system of linear equations. In 3D, the problem can be solved analytically not only for the sphere but also for several other simple shapes [14], where one typically calculates the "drag force" acting on the obstacle.

The above simple solution of the linearized hydrodynamic equations appears to fail if the obstacle has the form of an infinitely long cylinder (or equivalently, in 2D), the issue known as the "Stokes paradox". The reason for the apparent paradox lies in the approximation used to linearize the Navier–Stokes equation: the Reynolds number (i.e., the quantitative expression for the relative strength of the nonlinear and viscous

terms) is scale dependent and cannot be assumed small at arbitrary large distances [13, 14]. Instead of simply neglecting the nonlinear term, one should linearize it following Oseen [108], whose modified equation yields a consistent solution (as well as the corrected expression for the drag force).

In contrast to traditional hydrodynamics, in solid-state physics one is typically interested in linear response properties and has to take into account momentum relaxation due to weak impurity scattering. The latter allows one to stabilize the solution, while keeping it within linear response [106, 107]. Indeed, in ultra-pure electronic systems the Gurzhi number (4) may be much larger than the Reynolds number

$$\frac{\mathrm{Gu}}{\mathrm{Re}} = \frac{l^2/(v\tau_{\mathrm{dis}})}{ul/v} = \frac{l}{u\tau_{\mathrm{dis}}}, \tag{6}$$

justifying the Stokes approximation in the presence of the impurity scattering.

Stokes flow in the 2D electron system with a circular obstacle was observed in Ref. [32]. The experiment was performed in a GaAs heterostructure with the role of the obstacle played by an anti-dot (or a micro-hole) in the middle of the Hall bar, see Fig. 8. The measured resistivity was interpreted using the macroscopic approach of Refs. [109, 110]. The two scattering mechanisms (one due to impurity scattering and another due to viscosity) were treated as two parallel channels of momentum relaxation (based on the fact that the corresponding relaxation rates can be attributed to the first and second moments of the semiclassical distribution function). The two contributions can be separated since they have a different temperature dependence, in particular, the viscous contribution should exhibit the Gurzhi-like $\rho \sim T^{-2}$ behavior. Now, the obstacle does not seem to affect the latter, while the disorder contribution at low temperatures is significantly enhanced, see Fig. 8, which is consistent with

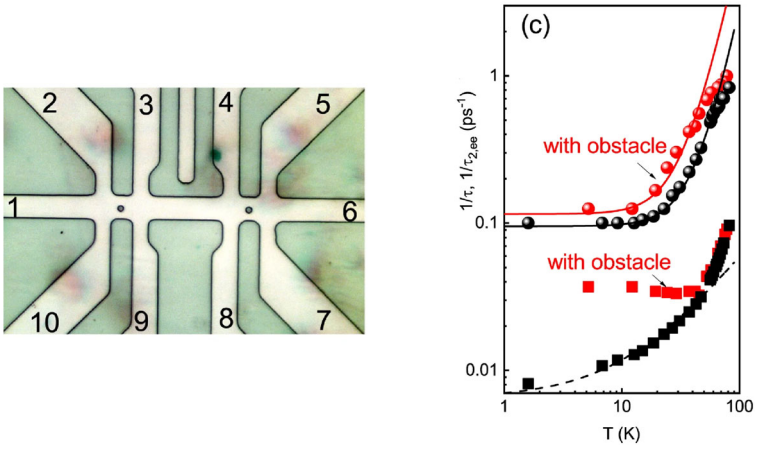

Fig. 8 Stokes flow around an obstacle in GaAs. Left panel: image of the Hall bar with two anti-dots used in the experiment [32]. Right panel: the disorder (squares) and electron–electron interaction (circles) scattering rates obtained from the experimental data measured in sample with (red) and without (black) the obstacle (From Ref. [32])

the expectation of the viscous fluid avoiding the obstacle (as opposed to individual electrons scattering off it).

2.4 Imaging of electronic flows

Although traditional linear response measurements may be strongly affected by the collective, hydrodynamic behavior, interpretation of such experiments is not straightforward [41]. It would be much easier if one could simply "watch" the flow (in a close analogy to the usual hydrodynamics). Fortunately, in recent years, several "scanning" or "imaging" techniques were suggested allowing one to do just that even if indirectly.

The basic requirement for any imaging technique is that it should be non-invasive, i.e., it should not disrupt the flow itself. When trying to image the flow of electrons, one can rely either on detecting spatial variation of electric potential [51, 52] or on detecting the local magnetic field induced by the charge motion [50].

2.4.1 Scanning carbon nanotube single-electron transistor

Electric current flowing through a conductor is known to generate a local change in electrostatic potential (or "voltage drop"). This potential can be detected using the capacitive coupling to a local probe such as the scanning single-electron transistor (SET), see Fig. 9. In particular, a nanotube SET may exhibit extreme voltage sensitivity, while the planar probe design could help minimizing the back action on (or gating) the sample [52]. Moreover, by applying weak perpendicular magnetic field, the same probe is able to resolve the Hall voltage associated with the flow, yielding a direct measure of the local current density.

Applying the nanotube SET technique to doped graphene in the hydrodynamic regime allowed to image the Poiseuille flow of charge carriers [51]. Similarly to the case of the Gurzhi effect, see Sect. 2.1, the main goal of the experiment was to distinguish the collective (hydrodynamic) motion from the single-particle (ballistic) behavior (assuming $\ell_{\rm dis}$ is the largest length scale in the problem). However, instead of contrasting the temperature dependence of the sample's resistance [41], here one has to compare the spatial profile of the current density. In the channel geometry, see Fig. 9, one studies its dependence on the lateral coordinate, $\boldsymbol{j} = j(y)\boldsymbol{e}_x$ (where $\boldsymbol{e}_x$ is the unit vector directed along the channel and y is the coordinate across the channel). The difficulty is that in contrast to the textbook diffusive behavior, where the current density is uniform (except in the narrow regions close to the sample boundaries), both in the ballistic and hydrodynamic cases $j(y)$ is characterized by a non-uniform profile with the maximum at the center of the channel [11, 112], making it difficult to distinguish the two regimes experimentally.

The hydrodynamic Poiseuille flow in a narrow channel is a textbook problem [13]. Taking into account weak impurity scattering and making the common assumption of the no-slip boundary conditions, one finds for the electric current density in doped graphene in the channel geometry

$$J_x = \sigma E_x \left[1 - \frac{\cosh(y/\ell_G)}{\cosh[W/(2\ell_G)]}\right], \tag{7}$$

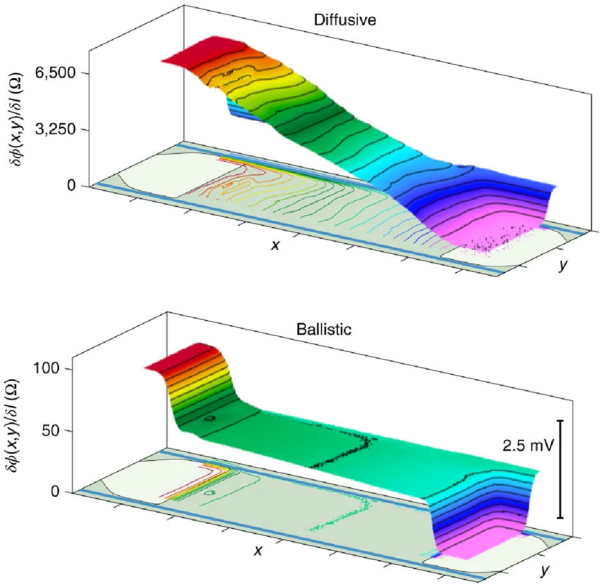

Fig. 9 Spatial imaging of the voltage drop of flowing electrons in the diffusive (left) and ballistic (right) regimes [52]. Both plots show the imaged electrostatic potential normalized by the total current (yielding a quantity with the units of resistance). The data were measured at $T = 4$ K. The diffusive flow was observed at charge neutrality (determined by the sharp maximum in the two-terminal resistance of the sample), while the ballistic behavior was imaged at the hole density of 1×10^{12} cm^{-2}. In the latter case, most of the voltage drop occurs at the contacts, with the contact resistance approaching the ideal Sharvin value [104, 111]. The bottom plane shows the equipotential contours superimposed on the schematic of the graphene channel and contacts, indicating the gradual voltage drop in the diffusive case contrasted to the flat potential typical of the ballistic motion [112]. (From Ref. [52]. Reprinted with permission from Springer Nature)

where σ in the bulk longitudinal conductivity and ℓ_G is the Gurzhi length [93, 110, 113–115]

$$\ell_G = \sqrt{\nu \tau_{\rm dis}}. \tag{8}$$

Here ν is the kinematic viscosity, see Eq. (2). The parabolic current density profile typical of the standard Poiseuille flow [13, 116] can be recovered by assuming a large Gurzhi length, $\ell_G \gg W$. In this limit, the sample resistance is proportional to the shear viscosity [114], a manifestation of the Gurzhi effect [17].

Introducing more realistic (Maxwell's) boundary conditions with nonzero slip length [117] effectively sets the coordinates where the catenary curve (7) reaches zero outside of the channel, but does not significantly affect the current density in the bulk of the sample. From the experimental viewpoint, however, the resulting curve is difficult to distinguish from the non-uniform current density in the ballistic regime, see the bottom panel in Fig. 10 and Sect. 3.2. As a result, one has to perform other measurements (e.g., the Hall field, see Fig. 10) to distinguish the two regimes [51].

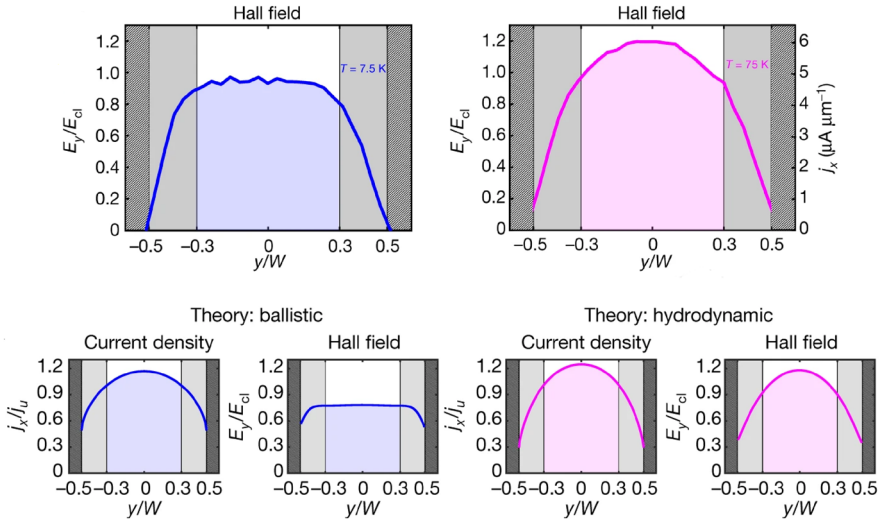

Fig. 10 Spatial imaging of the hydrodynamic flow of electrons in doped graphene [51]. Top: the Hall field E_y as obtained by numerical differentiation of the measured Hall voltage with respect to y, normalized by the classical value, $E_{\rm cl} = BJ/(neW)$. The top left panel shows data taken at $T = 7.5\,\mathrm{K}$, $B = \pm 12.5\,\mathrm{mT}$, and $E_{\rm cl} = 91\,\mathrm{Vm}^{-1}$. The right top panel shows data in the presumed hydrodynamic regime at $T = 75\,\mathrm{K}$, $B = \pm 18\,\mathrm{mT}$, and $E_{\rm cl} = 162\,\mathrm{Vm}^{-1}$. The right vertical axis converts the field into the units of the current density by scaling with ne/B. Bottom: calculated current density J_x/J_u (with $J_u = J/W$) and Hall field $E_y/E_{\rm cl}$. The numerical values were obtained using the parameters corresponding to the experimental data in the top panels. (From Ref. [51]. Reprinted with permission from Springer Nature)

2.4.2 Quantum spin magnetometry

An alternative technique for imaging the electric current density is based on the idea of measuring the associated stray magnetic field [50]. A sensitive quantum spin magnetometer was realized using nitrogen-vacancy (NV) centers in diamonds [118]. In contrast to Ref. [51], the experiment of Ref. [50] targeted the so-called Dirac fluid in neutral graphene and contrasted the presumed hydrodynamic regime with the diffusive behavior in low-mobility devices. The latter measurements served as a benchmark and yielded the standard picture of nearly uniform current (exhibiting a sharp decay near the channel boundaries, see also Sect. 3.2) shown in Fig. 11.

The main result of Ref. [50] is the observation (by means of the scanning NV magnetometry) of a Poiseuille-like flow of the electric current in neutral graphene described by a catenary curve (7). Comparing the data to Eq. (7), the authors have extracted the kinematic viscosity of the Dirac fluid in graphene (see the right panel in Fig. 11) showing a good quantitative agreement with the theoretical calculations of Ref. [119] (without any fitting procedure). Nevertheless, the results of Ref. [50] remain controversial. Within the existing theory of electronic hydrodynamics, the electric current is related to the hydrodynamic velocity by Eq. (3) up to an Ohmic correction. Precisely at charge neutrality, $n = 0$, and Eq. (3) yields zero, implying that any electric current at charge neutrality is not hydrodynamic, but is rather given by the Ohmic correction [120, 121] with the corresponding bulk conductivity determined

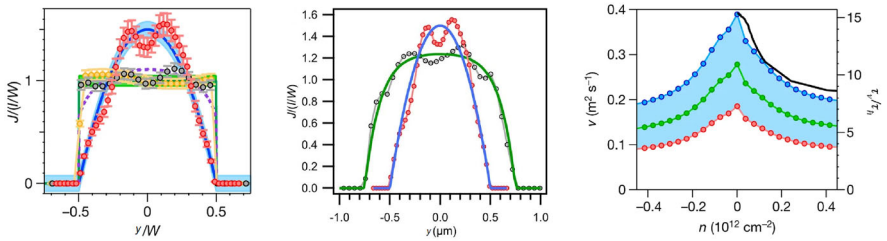

Fig. 11 Spatial imaging of the electric current in neutral graphene [50]. Left: reconstructed current density as a function of the lateral coordinate. The current is normalized by the average charge carrier flux I/W, where I is the total flux and $W = 1\,\mu$m is the width of the channel. The spatial coordinate y is normalized by W and centered on the channel. Red points show data measured in neutral graphene, gray points—in palladium channel, orange points—low-mobility graphene. The curves correspond to idealized theoretical expectations: blue—ideal viscous flow, green—uniform current, purple dashed—the current profile of non-interacting electrons with diffusive boundary condition. Center: similar measurement for $W = 1.5\,\mu$m compared to the data on the left. Solid lines are fit to Eq. (7). Right: bounds on kinematic viscosity obtained from fitting the data to Eq. (7). The black curve is the result of a theoretical calculation of Ref. [119] at $T = 300$ K and no adjustable parameters (From Ref. [50]. Reprinted with permission from Springer Nature)

by electron–electron interaction [122]. The situation is more involved if the system is subjected to the external magnetic field. In that case, the Ohmic correction acquires an additional dependence on the hydrodynamic velocity [120], which in particular leads to positive magnetoresistance [123, 124]. However, a recent theoretical calculation of the electronic flow in a channel geometry in neutral graphene based on the direct solution of hydrodynamic equations (see Sect. 4) yields the so-called "anti-Poiseuille" flow [125], with the current density exhibiting a minimum in the center of the channel—in contrast to the maximum in Eq. (7), see Sect. 5.

Another feature of the data shown in Fig. 11 not accounted for by the existing theory is that the electric current vanishes at the channel boundaries. Indeed, the boundary conditions for the Ohmic correction to Eq. (3) should be derived from the kinetic theory similarly to those describing ballistic propagation of electrons [11]. In that case, one has to solve the kinetic equation imposing boundary conditions on the electronic distribution function. Both extreme limits typically considered in literature, namely the diffusive and specular boundary conditions, do not lead to the current vanishing at the boundary. Moreover, the kinetic theory derivation of the hydrodynamic equations yields the Maxwell's boundary conditions for the hydrodynamic velocity [117]. Finally, there is strong experimental evidence [53] for the existence of classical edge currents in graphene that are not taken into account in existing theories but casting further doubts on the results shown in Fig. 11.

The importance of edge physics is further highlighted by the experiment of Ref. [44], where the NV magnetometry was used to image the flow of charge through a constriction (or a slit) in neutral graphene. The authors performed measurements in a channel geometry as well with somewhat contradicting results, see Fig. 12. While the channel measurement at nearly room temperature ($T = 298$ K) yielded the current density profile similar to that reported in Ref. [50], see Fig. 11, the same profile was observed at $T = 100$ K implying that the charge flow in the channel is not very sensi-

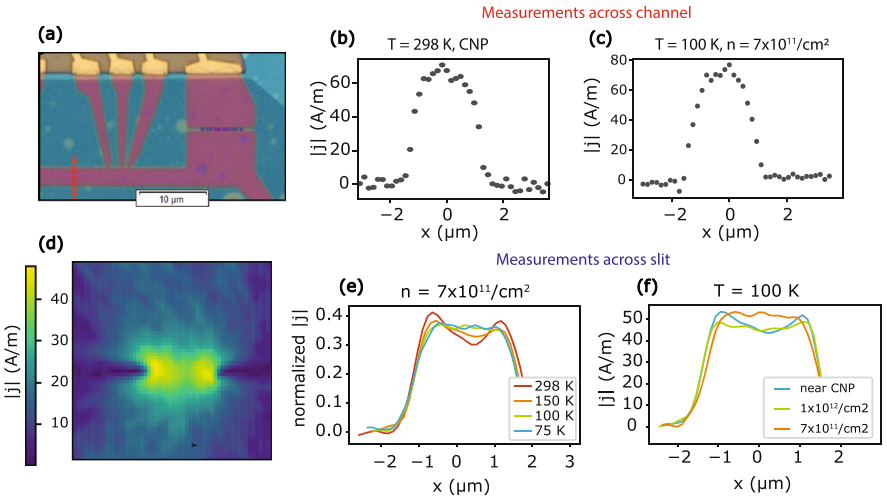

Fig. 12 Spatial imaging of the electric current in neutral graphene [44]. **a** Optical image of the graphene device showing the locations used in obtaining the current density measurements for the channel geometry **b**, **c**, $W = 2.7\,\mu$m, and the slit geometry (**d**–**f**). **b** Current density profile in the channel near the charge neutrality point (CNP) at $T = 298$ K. The black dots are the reconstructed current density. **c** Measurement of the current density profile of the channel at the same position as in **b**, but at $T = 100$ K and $n = 7 \times 10^{11}$ cm^{-2}. **d** Reconstructed current density magnitude at $T = 298$ K, near the CNP, showing the characteristic double peaks of Ohmic flow. **d** Temperature dependence of the reconstructed j_y at fixed carrier density $n = 7 \times 10^{11}$ cm^{-2} in a line cut through the constriction. **e** Carrier density dependence of j_y at fixed temperature $T = 100$ K. (From Ref. [44]. Reprinted with permission from the authors)

tive to the variation of the scattering length. In contrast, the current density measured in the slit geometry exhibited Ohmic behavior at room temperature, while at lower temperatures and finite charge densities the Ohmic double peaks disappeared indicating the crossover into the hydrodynamic regime. The authors of Ref. [44] explained the contradiction between the results in the channel and slit geometries by fact that the latter is not affected by the boundary conditions as much as the former. They conclude that while the edge physics is poorly understood the slit geometry is better suited to observe the Ohmic-viscous crossover.

2.4.3 Non-topological edge currents

Sample edges play a crucial role in all of the experiments discussed so far. Yet, understanding of the physics of the edges themselves has proven somewhat challenging. In traditional condensed matter physics [10], the focus is typically on bulk behavior and hence a system is modeled to be infinite. Sample geometry and edge scattering becomes important in mesoscopic physics [11, 112], but most details are encoded in the boundary conditions. Finally, edge states are being actively researched in the context of the Quantum Hall Effect (QHE) [126, 127] and more generally in the field of topological insulators [128]. But even in the latter case, the edge behavior is dictated by the topological properties of the bulk. At the same time, experiments show that sample

edges (in particular, in graphene, see Fig. 13) may exhibit charge accumulation [48, 129–131] and carry non-topological currents [53, 132].

Charge accumulation at the surface is a known phenomenon in semiconductors [133] and is a key feature in the traditional theory of the Schottky barrier [134]. Typically, these effects are associated with "band bending" or local, position-dependent changes in quasiparticle energy levels in the vicinity of the sample surface (or an interface). The band bending can also occur in 2D systems. In particular, it has been suggested that in graphene, band bending leads to p-doping of the edges, due to either intrinsic mechanisms or charged impurities (or defects) [48, 132, 135]. The resulting hole accumulation at the sample edges has been used in Ref. [53] to interpret the highly unusual nonlocal transport observed by means of SQUID-on-tip (SOT) thermal imaging and scanning gate microscopy [47, 48, 136] (for applications of scanning gate microscopy to 2D electron systems in semiconductor heterostructures, see Ref. [137]).

The experiment of Ref. [53] provided a deeper insight into the giant nonlocality observed in neutral graphene subjected to magnetic field in Ref. [70], see Sect. 2.2.1. While confirming the giant enhancement of the nonlocal resistance at charge neutrality and in magnetic field, the new data show a number of novel features: (i) the nonlocality exists even in the absence of magnetic field; although the observed R_{NL} is much smaller than in the presence of the field, it is still an order of magnitude stronger that the Ohmic expectation; (ii) the observed nonlocality is asymmetric with respect to electron and hole doping; (iii) in magnetic field, the system exhibits the Hall voltage of the opposite sign (as compared to the naive expectation); and most importantly, (iv) the observed nonlocality can be suppressed by applying a potential at the sample edges. The latter observation represents the key evidence in support of the interpretation of the data offered in Ref. [53]. The authors argue that the sample edges may carry electric current which in turn leads to nonlocal resistance. The fact that this current can be suppressed by a local potential points towards its non-topological origin (a topological

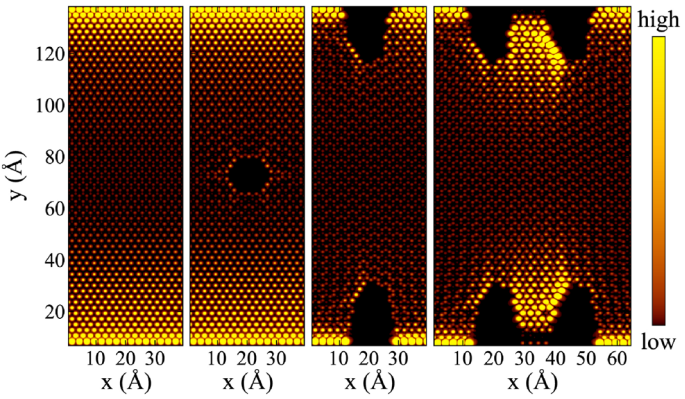

Fig. 13 DFT calculation of the local density of states (LDoS) in a graphene flake [131]. The enhanced LDoS at the edges appears regardless of the shape of the edge and the presence of macroscopic defects in the bulk (From Ref. [131])

current tends to flow around obstacles [48] such that applying a potential would just "redefine" the edge). The existence of the edge current is further corroborated by the thermal imaging, see Fig. 14.

The authors of Ref. [53] offer a simple theoretical model to account for the experimental data. Consider a sample that is infinite in x direction, while having a width W in the y direction. Without charge accumulation at the edges, the sample can be assumed to host a uniform charge density, while the current density can be found using the Ohm's law and the continuity equation. Consider now a different situation, where the charge density in narrow regions close the sample edge exceeds the bulk density. Now, the same equations have to be solved separately in the edge and bulk regions leading to the complicated behavior shown in Fig. 15.

The classical model accounts for the unexpected inversion of the Hall voltage and edge currents observed in the experiment, but does not explain the physical origin of these effects at a microscopic level. Some of these features appear to be rather general for the usual transport equations in the strip geometry. For example, current

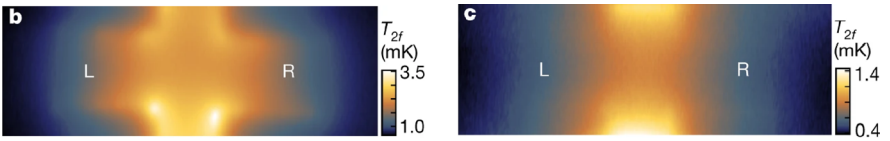

Fig. 14 Thermal imaging of a graphene sample [53]. Both images show the local temperature distribution obtained using the scanning SOT at the background temperature $T = 4.2\,\mathrm{K}$ and $B = 0$. Left: enhanced nonlocality in neutral graphene—heat dissipation is extended into the left and right arms of the Hall bar. Right: Ohmic behavior—heat dissipation is confined to the central region of the sample between the source and drain electrodes. (From Ref. [53]. Reprinted with permission from Springer Nature)

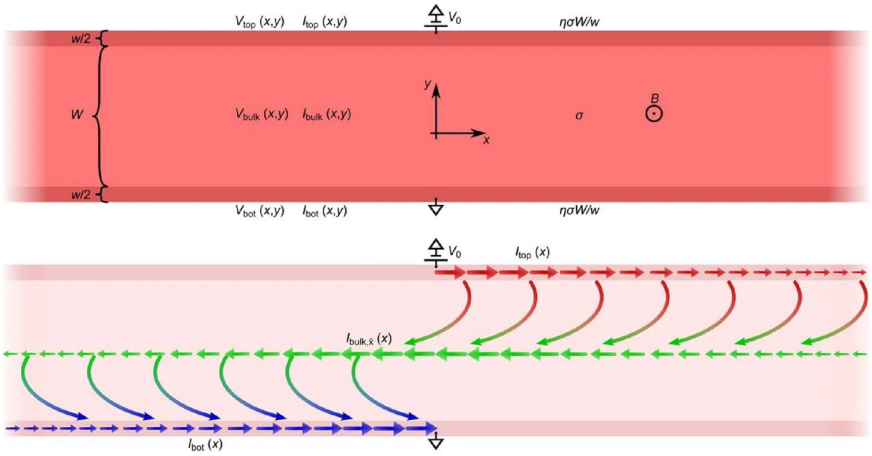

Fig. 15 Classical model mimicking the effects of charge accumulation at the sample edges [53]. Top: the setup—a strip-like sample of width W with bulk conductivity σ and narrow edge regions (width $w/2$) with the conductivity $\eta\sigma W/w$ with η being the phenomenological measure of charge accumulation. Bottom: non-uniform current density in the presence of the magnetic field B featuring the bulk flow in the direction opposite to the applied electric field. (From Ref. [53]. Reprinted with permission from Springer Nature)

flows against the direction of the applied electric fields have also been reported in Ref. [115], where the hydrodynamics-like phenomenology was used to define distinct edge regions where charge carriers react to the applied magnetic field differently than carriers in the bulk of the sample, see also Ref. [87].

Although implications of the results of Ref. [53] are not fully understood at the time of writing, it is clear that the boundary effects play a very important role in the observed behavior of small graphene samples. This presents a clear challenge for the theory which so far was focusing on bulk systems, see Sect. 3. In particular, the existing solutions of the hydrodynamic equations in the strip geometry (similar to Fig. 15) were found under the simplest model assumptions of either the no-slip or Maxwell's boundary conditions, see Sect. 3.

One could try to avoid the issue of the boundary conditions (except for the boundaries with the source and drain electrodes [138]) by utilizing the Corbino disk geometry [139]. Due to inherently inhomogeneous current flow (even in the Ohmic regime), the Corbino disk was suggested as a potential device to measure electronic viscosity [140]. More recently, hydrodynamic behavior in this setting was reported in the imaging experiment of Ref. [54].

2.5 Wiedemann–Franz law violation

Unconventional charge transport properties exhibited by electronic systems presumed to be in the hydrodynamic regime may be accompanied by unusual heat transport leading to strong violations of the Wiedemann–Franz law [141, 142]. Initially an empirical observation, the Wiedemann–Franz law can be readily understood within the standard, single-particle transport theory [10]. Qualitatively, if both charge and heat are carried by the same excitations and affected by the same scattering mechanisms (as is the case for non-interacting electron models), then the only difference between the electric and thermal conductivities is the dimensionality, leading to the famous expression

$$\frac{\kappa}{\sigma} = \mathcal{L}T, \qquad \mathcal{L} = \mathcal{L}_0 = \frac{\pi^2}{3e^2}. \tag{9}$$

Here σ and κ are the electric and thermal conductivities and the coefficient $\mathcal{L}$ is known as the Lorenz number, while the "universal" value $\mathcal{L}_0$ corresponds to free electrons. Now, electrons in solids are typically not free and hence there is no reason for Eq. (9) to be universally valid. In conventional metals, the Wiedemann–Franz law is approximately obeyed, for example the Lorenz number in copper exhibits deviations from $\mathcal{L}_0$ up to a factor of 2 at intermediate temperatures (depending on sample purity) [143]. Consequently, a strong violation of the Wiedemann–Franz law almost certainly an indication of unconventional physics, that in the context of electronic systems may include hydrodynamic behavior.

2.5.1 Large Lorenz number in neutral graphene

Unconventional thermal transport in neutral graphene was reported already in early experiments of Refs. [144, 145]. The Wiedemann–Franz law was then studied in detail

in Ref. [28] where it was interpreted as evidence for the hydrodynamic "Dirac fluid". An observation of the related phenomenon of giant thermal diffusivity in a Dirac fluid was reported in Ref. [146].

In hindsight, strong violation of the Wiedemann–Franz law in neutral graphene should have been expected (see also Ref. [147]) on the basis of the two celebrated features—the linear spectrum [148–150] and "quantum" conductivity [122, 151–155]. The latter indicates that the unusual feature of the electrical conductivity at charge neutrality is not its value, but rather the scattering mechanism behind it—electron–electron interaction. In contrast, the former ensures that the electron–electron interaction does not relax the energy current (since it is equivalent to the momentum flux, see Sect. 3), which implies that the thermal conductivity is determined by disorder scattering. As a result, the Lorenz number is expected to be proportional to the ratio of the disorder mean free time to the electron–electron scattering time, which in the hydrodynamic regime (or otherwise in ultra-clean graphene in the appropriate temperature interval) is assumed to be large, $\mathcal{L} \propto \tau_{\rm dis}/\tau_{ee} \gg 1$, see Fig. 16.

The intermediate nature of the hydrodynamic regime suggested by the data in Fig. 16 is corroborated by the results of the experiments on the thermoelectric power [40]. Here it manifested itself in the failure to uncover the ideal hydrodynamic limit where (in the absence of disorder) the thermopower equals the thermodynamic entropy per carrier charge [89, 158]. Still, the observed thermopower at relatively high temperatures significantly exceeded the standard Mott relation indicating the hydrodynamic behavior [40].

Interestingly, the hydrodynamic theory predicts the Wiedemann–Franz law violation even in doped graphene (in the Fermi-liquid regime) [24, 159] (for a detailed discussion of the Wiedemann–Franz law violation in Fermi liquids in general see Ref. [160]), but now the Lorenz number is predicted to be small (and in fact vanish in the limit of large densities, see Sect. 3). The effect can not be clearly seen in Fig. 16, presumably due to relatively low densities explored in the data shown. This prediction suggests a possible relation with the small Lorenz number observed in topological materials, which has not been fully addressed so far.

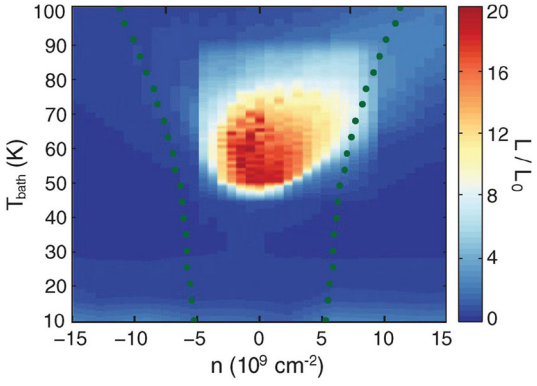

Fig. 16 Wiedemann–Franz law violation in neutral graphene [28]. The color scheme shows the Lorenz number as a function of the charge density and bath temperature. The unusually large Lorenz number is observed in the vicinity of charge neutrality and in a temperature window above the disorder-dominated regime, but below the onset of electron–phonon coupling (From Ref. [28]. Reprinted with permission from AAAS)

2.5.2 Small Lorenz number in topological materials

Recently, hints of electronic hydrodynamics have been observed in the topological material WP_2 [31, 156], where the Wiedemann–Franz law is also strongly violated, see Fig. 17. The measured thermal and electrical conductivities in WP_2 exhibit features that are significantly different from those observed in graphene. The presumed hydrodynamic regime is limited to temperatures below 20 K (as determined by the electron–phonon scattering dominating transport properties at higher temperatures). Here, the measured Lorenz number turns out to be small, $\mathcal{L} \ll \mathcal{L}_0$, the result that was attributed to the existence of the hydrodynamic regime (confirmed by the extremely large measured values of the typical length scale describing momentum-relaxing scattering properties). Interestingly enough, similar effects have been observed in a different topological material, MoP [157].

The precise microscopic nature of the proposed hydrodynamic state and especially its relation to the hydrodynamic regime in graphene remains unclear. An interesting proposal on the experimental measurement of one of the relevant length scales, the "momentum-relaxing" length (e.g., ℓ_{dis}), which together with the "momentum-conserving" length ℓ_{ee} determines whether the sample is in the hydrodynamic, ballistic, or Ohmic regime, was suggested in Ref. [161]. The authors used Sondheimer oscillations [162] to extract ℓ_{dis} even in the ballistic case $\ell_{\text{dis}} \gg L$ (where L is the typical system size) and suggested that this effect can be used as an effective quantitative probe for identifying scattering processes in ultra-clean materials.

3 Electronic hydrodynamics

Hydrodynamic description of interacting particles (or excitations) has long been part of the theoretical toolbox used (in addition to traditional fluid mechanics [13]) in a wide range of fields including many-body theory [3], superfluids [15, 26], quark–gluon plasma [163], or interstellar matter [164]. The underlying general idea allowing to develop the hydrodynamic theory suitable to such different circumstances is the

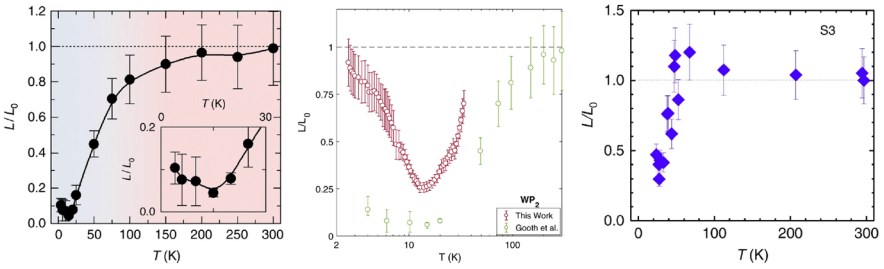

Fig. 17 Wiedemann–Franz law violation in topological materials. Left: the Lorenz number extracted from measurements of the electrical and thermal conductivities in a WP_2 micro-ribbon (width 2.5 μm) (Reprinted from Ref. [156]). The inset shows the zoomed-in low-temperature region of the same data. Central: the Lorenz number in bulk (mm-sized) single crystals of WP_2 (Reprinted from Ref. [31]). Green dots show the data from the left plot. Right: the Lorenz number in MoP (Reprinted from Ref. [157])

universality of the long-time, long-wavelength behavior, i.e., the assumption that macroscopic (long-distance) physics is independent of microscopic details and is governed by symmetries, which can be expressed in terms of continuity equations.

The most common symmetry assumed in physics is time translation invariance leading to energy conservation. The corresponding continuity equation reads

$$\partial_t n_E + \boldsymbol{\nabla}\cdot \boldsymbol{j}_E = 0, \tag{10a}$$

where n_E is the energy density and $\boldsymbol{j}_E$ is the energy current.

The second conservation law typically assumed in the context of electronic systems is the particle number (or charge) conservation (manifesting gauge invariance) described by the continuity equation

$$\partial_t n + \boldsymbol{\nabla}\cdot \boldsymbol{j} = 0. \tag{10b}$$

Here n and $\boldsymbol{j}$ are the particle number and current densities while the charge and electric current densities differ by a factor of the electric charge, see also Eq. (1).

Supplementing equations (10a) and (10b) by the thermodynamic equation of state and the entropy balance equation [1] one may arrive at the macroscopic theory describing the long-distance properties of the system and find the spectrum of the collective modes. The resulting behavior is diffusive (i.e., equivalent to the standard Drude-like approach to electronic transport [10]).

In contrast, conventional fluids are additionally assumed to be translationally invariant which implies momentum conservation described by the continuity-like equation for the momentum density, $\boldsymbol{n_k}$,

$$\partial_t n^\alpha_{\boldsymbol{k}} + \nabla^\beta \Pi^{\alpha\beta}_E = 0. \tag{10c}$$

Here $\Pi^{\alpha\beta}_E$ is the momentum flux (or stress-energy) tensor. Introducing momentum conservation has a drastic effect on the collective modes of the system leading to the appearance of a mode with the linear dispersion, i.e., the sound mode [1]. The existence of the latter is the crucial distinction between hydrodynamics and other macroscopic, long-wavelength theories (although a more general interpretation of the term "hydrodynamics" is also used in literature, see, e.g., Ref. [1]).

The explicit form of the hydrodynamic equations can be obtained by supplementing the continuity equations (10) by the so-called "constitutive relations" reducing the amount of independent variables and turning Eqs. (10) into a closed set. This is typically done under the assumption of local equilibrium [13]. Moreover, the form of the stress-energy tensor in the moving fluid is often obtained by relating to the properties of the stationary fluid (that are assumed to be known). To do that, one needs to change the reference frame to the rest frame of the fluid. Consequently, traditional hydrodynamics [13] distinguishes the two cases of Galilean- and Lorentz-invariant fluids, i.e., the classical and relativistic hydrodynamics. While early applications of the hydrodynamic approach to electronic transport were based on the classical theory [17, 22, 165], it is the possibility of realization of relativistic hydrodynamics in graphene that ignited the current interest in the field.

3.1 Relativistic hydrodynamics in a solid-state laboratory

The discovery of graphene and Dirac fermions in it [151] has provided a unique opportunity to study relativistic effects in a solid-state laboratory [166]. In particular, early work on collective electronic flows attempted to adapt relativistic hydrodynamics in $(2+1)$ dimensions to Dirac fermions in graphene [147, 167].

3.1.1 Ideal relativistic fluid

Standard equations of relativistic hydrodynamics [13] are encoded in the relation

$$\frac{\partial T_i^k}{\partial x^k} = 0, \tag{11}$$

where T^{ik} is the relativistic stress-energy tensor (in graphene, this is a 3×3 tensor in the $(2+1)$-dimensional space-time)

$$T^{ik} = w u^i u^k - p g^{ik}, \tag{12a}$$

with w and p being the enthalpy and pressure, respectively, in the local rest frame.

For the purposes of this review, it will be instructive to write down the explicit form of the individual components of T^{ik}: the energy density

$$T^{00} = \frac{w}{1 - u^2/v_g^2} - p, \tag{12b}$$

the momentum density (here we adopt the usual practice of denoting the space components by Greek indices, while the Roman indices refer to the space-time)

$$T^{0\alpha} = \frac{w u_\alpha}{v_g \left(1 - u^2/v_g^2\right)}, \tag{12c}$$

and finally the momentum flux density

$$T^{\alpha\beta} = \frac{w u_\alpha u_\beta}{v_g^2 \left(1 - u^2/v_g^2\right)} + p\delta_{\alpha\beta}. \tag{12d}$$

The energy flux density is proportional to the momentum density and is given by $v_g T^{0\alpha}$. This fact will be explored in more detail below.

The relativistic generalization of the Euler equation [168] can be obtained by projecting Eq. (11) onto the direction perpendicular to the 3-velocity u^i [13]. This yields

$$\frac{w}{1 - u^2/v_g^2}\left[\frac{\partial}{\partial t} + \boldsymbol{u}\cdot\nabla\right]\boldsymbol{u} + v_g^2 \nabla p + \boldsymbol{u}\frac{\partial p}{\partial t} = 0. \tag{13a}$$

Supplementing the Euler equation (13a) by the relativistic continuity equation

$$\frac{\partial\left(nu^k\right)}{\partial x^k}=0, \tag{13b}$$

and the thermodynamic equation of state

$$w=3p, \tag{13c}$$

one can quickly convince oneself that the ideal flow described by Eq. (13a) is isentropic

$$\frac{\partial\left(su^k\right)}{\partial x^k}=0. \tag{13d}$$

Equations (13) represent the closed set of hydrodynamic equations describing an ideal (non-dissipative) flow of a single-component relativistic fluid in a $(2+1)$-dimensional space-time with the velocity v_g playing the role of the speed of light. This theory possesses a collective mode [24, 121, 122, 169–176] with the linear dispersion relation

$$\omega=\frac{v_g q}{\sqrt{2}}. \tag{14}$$

In the literature, this mode has been referred to as the "cosmic sound" [169] or the "second sound" [174].

3.1.2 Electronic fluid in graphene

The ideal hydrodynamic theory outlined in the previous Section can be considered a purely phenomenological since it is based on an implicit assumption of equilibrium in the local rest frame without discussing the physical processes responsible for the equilibration. In the case of graphene, that has to be electron–electron interaction, which is the *classical, three-dimensional* Coulomb interaction. The latter point refers to the fact that although graphene is atomically thin so that the electron motion is restricted to two dimensions, the electric field induced by the electron charges is not. The former point refers to the orders of magnitude difference between the electron velocity and the speed of light, $v_g \ll c$, preventing the above hydrodynamic theory and electromagnetic fields to be transformed by the same Lorentz transformation. This issue was addressed in detail in Ref. [147].

Coulomb interaction can be included in the hydrodynamic description by re-writing the relativistic Euler equation (11) in the form

$$\frac{\partial T_i^k}{\partial x^k}=\frac{e}{c}F_{ik}j^k. \tag{15}$$

Notice, that in the right-hand side of this equation one has to write the speed of light, which is inconsistent with the use of the velocity v_g in the stress-energy tensor (12).

A possibility to resolve this issue was suggested in Ref. [147]. Indeed, redefining the electromagnetic field tensor F_{ik} and the current j^k as

$$F_{ik} = \begin{pmatrix} 0 & (c/v_g)E_x & (c/v_g)E_y \\ -(c/v_g)E_x & 0 & -B \\ -(c/v_g)E_y & B & 0 \end{pmatrix}, \tag{16}$$

$$j^k = \left(v_g n,\ \boldsymbol{j}\right), \tag{17}$$

one may remove the inconsistency from Eq. (15) turning it into the standard form of the relativistic Euler equation. However, this is only a partial solution since the redefined field tensor (16) leaves only two Maxwell's equations intact,

$$\nabla \times \boldsymbol{B} = 0, \qquad \nabla \cdot \boldsymbol{E} = 4\pi e n, \tag{18}$$

while the other two are violated leaving the above approach questionable.

Even if the modified equation (15) can be accepted for those problems that do not involve the two violated Maxwell's equations (e.g., a description of stationary currents), there are other issues that prevent one from treating electronic flows in graphene as truly relativistic. As already mentioned above, there are other scattering processes in graphene (and in any other solid) affecting the behavior of charge carriers. These may include electron–phonon and disorder scattering, Auger processes, and three-particle collisions, none of which are Lorentz-invariant. Moreover, typical currents studied in present-day experiments are small enough, such that the hydrodynamic velocity is small as well, $u \ll v_g$. As a result, one would be interested in the non-relativistic limit of the hydrodynamic equation (15) anyways. Now, the non-relativistic form of hydrodynamics can also be derived within the kinetic theory approach (see the next section), where all of the above issues can be consistently taken into account. In the absence of dissipative processes, the generalized Euler equation for the hydrodynamic electronic flows in graphene obtained from the kinetic theory does indeed closely resemble Eq. (13a), while containing additional terms taking into account scattering processes that were not considered so far. In addition, introducing dissipative processes within the phenomenological approach involves defining new parameters, such as electrical conductivity and viscosity, that can only be determined in an experiment. While the kinetic theory provides a method to "calculate" these parameters, the accuracy of these calculations may be limited depending on the initial assumptions allowing one to formulate the kinetic equation in the first place. The form of the dissipative corrections remains the same in both approaches providing a useful checkpoint.

3.2 Kinetic theory approach

Kinetic approach has been used to describe electronic transport in solids for decades [10]. While applicability of the kinetic theory to quantum many-body systems remains an active area of research [177], it is often assumed that at least at high enough temperatures electrons behave semiclassically such that the kinetic theory is applicable. At the same time, this implies that quasiparticle excitations are long-lived, the assump-

tion that might not be valid in strongly correlated or hydrodynamic regimes. Strictly speaking, the kinetic equation can only be applicable in weakly interacting electronic systems. This might be a problem in graphene, where the effective coupling constant in an idealized model is $\alpha_g = e^2/v_g \approx 2.2$ (which may be reached in suspended graphene) and while an insulating substrate may reduce this value (by a factor of the dielectric constant), the resulting α_g is not small (typically, $\alpha_g \approx 0.2 \div 0.3$ [43, 178]). Consequently, derivation of the hydrodynamic equations has to rely on universality: one assumes that the form of the equations is independent of the interaction strength (similarly to how the Navier–Stokes equation derived from the kinetic theory of rarefied gases [16] can be used to describe properties of water, where the kinetic equation is not applicable). Calculation of kinetic coefficients then has to rely on the renormalization group procedure [119, 179] treating α_g as a running coupling constant [180–183]. One renormalizes the theory to the parameter regime, where the coupling constant is small, solves the kinetic equations, and then renormalizes back to realistic parameter values. For a more microscopic approach to deriving the hydrodynamic equations based on the nonequilibrium Keldysh technique, see Ref. [184]. This paper provides a proper microscopic treatment of inelastic electron–electron scattering that is responsible for establishing the local equilibrium that is the central assumption of the kinetic approach discussed below.

3.2.1 Quasiclassical Boltzmann equation

At high enough temperatures (where the hydrodynamic behavior is observed [27, 39, 41, 42]), the quasiparticle spectrum in monolayer graphene [185] comprises two bands of carriers (the "conductance" and "valence" bands) that touch in the corners of the hexagonal Brillouin zone, i.e., at the "Dirac points" (multilayer graphene was discussed in Ref. [186]). In the vicinity of the Dirac points the spectrum can be approximately considered to be linear (logarithmic renormalization due to electron–electron interaction [181], see also Ref. [187], is observed at much lower temperatures [188]). The linearity of the Dirac spectrum leads to two important kinematic effects: (i) the suppression of Auger processes [89, 189] and hence approximate conservation of the number of particles in each band independently [23, 24, 89, 190]; and (ii) the so-called "collinear scattering singularity" [122–124, 153, 180, 190–192]. The former represents an additional conservation law that is not taken into account in the above phenomenological hydrodynamics. The latter is justified by the smallness of the effective coupling constant and allows for a nonperturbative solution of the Boltzmann equation (recall that the Boltzmann approach itself is justified in the weak coupling limit, $\alpha_g \to 0$).

Consider now the two-band model of low-energy quasiparticles in graphene. Within the kinetic approach, the quasiparticles can be described by a distribution function, $f_{\lambda \boldsymbol{k}}$, where each quasiparticle state is characterized by the band index (or chirality), $\lambda = \pm 1$, and 2D momentum, $\boldsymbol{k}$. The spectrum is assumed to be linear,

$$\epsilon_{\lambda \boldsymbol{k}} = \lambda v_g k, \tag{19a}$$

with the straightforward relation between velocities and momenta,

$$\boldsymbol{v}_{\lambda\boldsymbol{k}} = \lambda v_g \frac{\boldsymbol{k}}{k}, \qquad \boldsymbol{k} = \frac{\lambda k}{v_g}\boldsymbol{v}_{\lambda\boldsymbol{k}} = \frac{\epsilon_{\lambda\boldsymbol{k}}\boldsymbol{v}_{\lambda\boldsymbol{k}}}{v_g^2}. \tag{19b}$$

The distribution function satisfies the kinetic (Boltzmann) equation

$$\mathcal{L} f_{\lambda\boldsymbol{k}} = \mathrm{St}_{ee}[f_{\lambda\boldsymbol{k}}] + \mathrm{St}_R[f_{\lambda\boldsymbol{k}}] + \mathrm{St}_{\mathrm{dis}}[f_{\lambda\boldsymbol{k}}], \tag{20a}$$

where the left-hand side (LHS) is defined by the Liouville's operator

$$\mathcal{L} = \partial_t + \boldsymbol{v}\cdot\boldsymbol{\nabla}_{\boldsymbol{r}} + \left(e\boldsymbol{E} + \frac{e}{c}\boldsymbol{v}\times\boldsymbol{B}\right)\cdot\boldsymbol{\nabla}_{\boldsymbol{k}}, \tag{20b}$$

and the right-hand side (RHS) represents the collision integral.

In the simplest Golden-Rule-like approximation, different scattering processes contribute to the collision integral in the additive fashion; hence, the form of the RHS in Eq. (20a). In the hydrodynamic regime, the electron–electron interaction (described by St_{ee}) is the dominant scattering process responsible for equilibration of the system. Consequently, *local equilibrium* is described by the distribution function that nullifies St_{ee} [16]

$$\mathrm{St}_{ee}\left[f^{(le)}_{\lambda\boldsymbol{k}}\right] = 0, \qquad f^{(le)}_{\lambda\boldsymbol{k}} = \left\{1+\exp\left[\frac{\epsilon_{\lambda\boldsymbol{k}} - \mu_\lambda(\boldsymbol{r}) - \boldsymbol{u}(\boldsymbol{r})\cdot\boldsymbol{k}}{T(\boldsymbol{r})}\right]\right\}^{-1}, \tag{21}$$

where $\mu_\lambda(\boldsymbol{r})$ is the local chemical potential and $\boldsymbol{u}(\boldsymbol{r})$ is the hydrodynamic (or "drift") velocity. The local equilibrium distribution function (21) allows for independent chemical potentials in the two bands, which can be expressed in terms of the "thermodynamic" and "imbalance" [89] chemical potentials

$$\mu_\lambda = \mu + \lambda\mu_I. \tag{22}$$

In global equilibrium (i.e., for stationary fluid)

$$f^{(0)} = f^{(le)}_{\lambda\boldsymbol{k}}(\mu_I = 0, \boldsymbol{u} = 0). \tag{23}$$

In addition, two more scattering processes need to be taken into account. Even ultra-pure graphene samples contain some degree of (weak) disorder. Scattering on impurities violates momentum conservation leading to a weak decay term in the generalized Euler equation [23, 24, 120, 121]. This process (as well as other momentum-relaxing processes) is described in Eq. (20a) by $\mathrm{St}_{\mathrm{dis}}$. At the same time, electron–phonon interaction may lead not only to the loss of electronic momentum (which is already taken into account in $\mathrm{St}_{\mathrm{dis}}$), but also to the loss of energy. Consequently, despite being subdominant in the hydrodynamic regime the electron–phonon interaction should be taken into account as one of the dissipative processes. However, due to the linearity of the Dirac spectrum, lowest order scattering on acoustic phonons

is kinematically suppressed. Instead, it is a higher order process, the so-called disorder-assisted electron–phonon scattering [193] or "supercollisions" [194–197], that plays the most important role in the hydrodynamic regime. Indeed, supercollisions violate not only energy conservation, but also conservation of the number of particles in each band. As a result, continuity equations for energy and single-band particle numbers also acquire weak decay terms. In the kinetic equation (20a), these effects are described by St_R (the subscript "R" here stands for "recombination", see Refs. [86–89, 114, 198–200]).

Within the kinetic theory, conservation laws are manifested in the sum rules for the collision integrals. There are four conservation laws to consider: energy, momentum, and particle number in the two bands. The latter can be expressed in terms of the "charge" and "total quasiparticle" (or imbalance) numbers similarly to Eq. (22)

$$n_\lambda = \frac{1}{2}\left(\lambda n + n_I\right). \tag{24}$$

The continuity equation (10b) representing global charge conservation can be obtained by summing the kinetic equation (20a) over all quasiparticle states. During this procedure, all three collision integrals in Eq. (20a) vanish [16]

$$\begin{aligned} N\sum_\lambda \int \frac{d^2k}{(2\pi)^2}\mathrm{St}_{ee}[f_{\lambda\boldsymbol{k}}] &= N\sum_\lambda \int \frac{d^2k}{(2\pi)^2}\mathrm{St}_R[f_{\lambda\boldsymbol{k}}] \\ &= N\sum_\lambda \int \frac{d^2k}{(2\pi)^2}\mathrm{St}_{\mathrm{dis}}[f_{\lambda\boldsymbol{k}}] = 0. \end{aligned} \tag{25a}$$

Moreover, electron–electron and disorder scattering also conserve the number of particles in each band, such that

$$N\sum_\lambda \int \frac{d^2k}{(2\pi)^2}\lambda\mathrm{St}_{ee}[f_{\lambda\boldsymbol{k}}] = N\sum_\lambda \int \frac{d^2k}{(2\pi)^2}\lambda\mathrm{St}_{\mathrm{dis}}[f_{\lambda\boldsymbol{k}}] = 0, \tag{25b}$$

whereas supercollisions lead to a decay term in the continuity equation for the imbalance density

$$N\sum_\lambda \int \frac{d^2k}{(2\pi)^2}\lambda\,\mathrm{St}_R[f_{\lambda\boldsymbol{k}}] \approx -\mu_I n_{I,0}\lambda_Q \approx -\frac{n_I - n_{I,0}}{\tau_R}. \tag{25c}$$

Here $n_{I,0}$ is the imbalance density at global equilibrium, see Eq. (23), i.e., for $\mu_I = 0$ and $\boldsymbol{u} = 0$. The first equality in Eq. (25c) was suggested in Ref. [89] and serves as the definition of the dimensionless coefficient λ_Q, while the second (valid to the leading order) was suggested in Refs. [87, 120] and offers the definition of the "recombination time" τ_R (see also Ref. [198]). The two expressions are equivalent since $n_I - n_{I,0} \propto \mu_I$.

Similarly, both electron–electron and disorder scattering conserve energy, hence the corresponding collision integrals vanish upon summation over all quasiparticle

states with an extra factor of energy

$$N\sum_{\lambda}\int\frac{d^2k}{(2\pi)^2}\epsilon_{\lambda\boldsymbol{k}}\mathrm{St}_{ee}[f_{\lambda\boldsymbol{k}}]=N\sum_{\lambda}\int\frac{d^2k}{(2\pi)^2}\epsilon_{\lambda\boldsymbol{k}}\mathrm{St}_{\mathrm{dis}}[f_{\lambda\boldsymbol{k}}]=0. \tag{25d}$$

Integrating the "recombination" collision integral one finds [201]

$$N\sum_{\boldsymbol{k}}\epsilon_{\lambda\boldsymbol{k}}\mathrm{St}_R[f_{\lambda\boldsymbol{k}}]=-\mu_I n_{E,0}\lambda_{QE}\approx-\frac{n_E-n_{E,0}}{\tau_{RE}}. \tag{25e}$$

The equivalence of the two forms of the decay term stems from $n_E-n_{E,0}\propto\mu_I$ assuming the electrons and holes are characterized by the same temperature.

Supercollisions contribute differently to recombination and energy relaxation. Recombination typically implies scattering between the quasiparticle states in different bands only. At the same time, supercollisions may also take place within a single band [193]. This process does not affect the number of particles in the band, but is accompanied by the energy loss as the electron scatters from a higher energy state into a lower energy state (losing its momentum to the impurity). Consequently, this process provides an additional contribution to energy relaxation. Thus, the time scales τ_R and τ_{RE} should be quantitatively different, although of the same order of magnitude (at least at charge neutrality and in the hydrodynamics regime).

Now, other processes may contribute to τ_R and τ_{RE}, including direct electron–phonon scattering [86, 89, 124, 192, 193, 202, 203], scattering on optical phonons [158, 204], three-particle collisions [24, 204], and Auger processes [23, 24, 89, 190]. Taking into account these effects does not change the functional form of the continuity equations leaving the integrated collision integrals (25c) and (25e) intact, but may affect the theoretical estimates of the values of τ_R and τ_{RE} (see Refs. [193, 201]). Given the approximate nature of such calculations, one may treat these parameters as phenomenological taking into account all relevant scattering processes.

Finally, electron–electron interaction conserves momentum and hence

$$N\sum_{\lambda}\int\frac{d^2k}{(2\pi)^2}\boldsymbol{k}\,\mathrm{St}_{ee}[f_{\lambda\boldsymbol{k}}]=0. \tag{25f}$$

On the other hand, weak disorder scattering leads to a weak decay term that should be included in Eq. (10c). Within the simplest τ-approximation [16, 120]

$$N\sum_{\lambda}\int\frac{d^2k}{(2\pi)^2}\boldsymbol{k}\,\mathrm{St}_{\mathrm{dis}}[f_{\lambda\boldsymbol{k}}]=\frac{\boldsymbol{n}_{\boldsymbol{k}}}{\tau_{\mathrm{dis}}}. \tag{25g}$$

The remaining collision integral St_R also does not conserve momentum, but given the phenomenological nature of τ_{dis} [43] (a better version of the disorder collision integral in graphene should involve the Dirac factors suppressing backscattering [205] which would lead to the similar approximation but with the transport scattering time, which

in graphene differs by a factor of 2), the contribution of the next-order supercollisions (involving both disorder and phonons) may be considered to be included in $\tau_{\rm dis}$ (similarly to the above discussion of τ_R and τ_{RE}).

3.2.2 Continuity equations in graphene

Using the above properties of the collision integrals, one can easily obtain the continuity equations in graphene [23, 24, 120] by integrating the kinetic equation (20a). In comparison to the "phenomenological" continuity equations (10), the resulting equation will contain extra terms due to the weak decay processes (discussed in the previous Section) and external electromagnetic fields. Hence the only true symmetry of the electronic fluid in a solid is gauge invariance that manifests itself by means of the continuity equation (10b)

$$\partial_t n + \boldsymbol{\nabla}\cdot\boldsymbol{j} = 0, \tag{26a}$$

where the kinetic definitions of the "charge" density and current are [cf. Eq. (24)]

$$n = n_+ - n_-, \qquad n_+ = N\int \frac{d^2k}{(2\pi)^2} f_{+,\boldsymbol{k}}, \qquad n_- = N\int \frac{d^2k}{(2\pi)^2}\left(1 - f_{-,\boldsymbol{k}}\right), \tag{26b}$$

and [cf. Eq. (1)]

$$\boldsymbol{j} = \boldsymbol{j}_+ - \boldsymbol{j}_- = N\int \frac{d^2k}{(2\pi)^2}\left[\boldsymbol{v}_{+,\boldsymbol{k}} f_{+,\boldsymbol{k}} - \boldsymbol{v}_{-,\boldsymbol{k}}\left(1 - f_{-,\boldsymbol{k}}\right)\right]. \tag{26c}$$

In the two-band model of graphene, the number of particles in each band is approximately conserved (see above). Hence, in addition to Eq. (26a), one finds a continuity equation for the "imbalance density", see Eq. (24),

$$\partial_t n_I + \boldsymbol{\nabla}\cdot\boldsymbol{j}_I = -\frac{n_I - n_{I,0}}{\tau_R}, \tag{26d}$$

where

$$n_I = n_+ - n_-, \qquad \boldsymbol{j} = \boldsymbol{j}_+ + \boldsymbol{j}_-, \tag{26e}$$

and the RHS in Eq. (26d) comes from integrating the collision integral, see Eq. (25c).

The continuity equation for the energy density is obtained by multiplying the kinetic equation (20a) by $\epsilon_{\lambda\boldsymbol{k}}$ and summing over all quasiparticle states,

$$\partial_t n_E + \boldsymbol{\nabla}\cdot\boldsymbol{j}_E = e\boldsymbol{E}\cdot\boldsymbol{j} - \frac{n_E - n_{E,0}}{\tau_{RE}}, \tag{26f}$$

where n_E and $\boldsymbol{j}_E$ are defined as

$$n_E = N \sum_{\lambda} \int \frac{d^2k}{(2\pi)^2} \epsilon_{\lambda \boldsymbol{k}} f_{\lambda \boldsymbol{k}} \tag{26g}$$

and

$$\boldsymbol{j}_E = N v_g^2 \sum_{\lambda} \int \frac{d^2k}{(2\pi)^2} \boldsymbol{k} f_{\lambda \boldsymbol{k}} = v_g^2 \boldsymbol{n}_{\boldsymbol{k}}. \tag{26h}$$

The last equality represents the fact that in graphene the momentum density is proportional to the energy density [due to the properties of the Dirac spectrum Eq. (19)]. The two terms in the RHS in Eq. (26f) come from the Lorentz term in the Liouville's operator (20b) and the integrated collision integral, see Eq. (25e). The former physically represents Joule's heat.

Finally, the continuity equation representing momentum conservation is obtained by multiplying the kinetic equation (20a) by $\boldsymbol{k}$ and summing over all states. In contrast to the "phenomenological" equation (10c), the resulting equations contains extra terms stemming from the effect of the electromagnetic field and weak disorder (25g)

$$\partial_t n_{\boldsymbol{k}}^{\alpha} + \nabla^{\beta} \Pi_E^{\alpha\beta} - enE^{\alpha} - \frac{e}{c} \left[\boldsymbol{j} \times \boldsymbol{B} \right]^{\alpha} = -\frac{n_{\boldsymbol{k}}^{\alpha}}{\tau_{\text{dis}}}. \tag{26i}$$

Here $\boldsymbol{n}_{\boldsymbol{k}}$ is given by Eq. (26h) and the momentum flux tensor is defined as

$$\Pi_E^{\alpha\beta} = N \sum_{\lambda} \int \frac{d^2k}{(2\pi)^2} k^{\alpha} v_{\lambda \boldsymbol{k}}^{\beta} f_{\lambda \boldsymbol{k}}. \tag{26j}$$

3.2.3 Constitutive relations

Continuity equations represent the global conservation laws and are valid without any further assumptions. Hydrodynamics, however, assumes that the set of continuity equations can be closed by expressing the vector and tensor quantities (i.e., the currents and stress-energy tensor) in terms of the "velocity field" $\boldsymbol{u}(\boldsymbol{r})$. Such expressions are known as "constitutive relations". Phenomenologically, they can be derived using the Galilean or (in the relativistic case) Lorentz invariance [13]. However, neither is valid for Dirac fermions in graphene (the former due to the linear spectrum and the latter due to the classical nature of the Coulomb interaction, see Sect. 3.1.2). Instead, one can derive the constitutive relations from the kinetic theory under the assumption of local equilibrium [23, 120]. Indeed, substituting the local equilibrium distribution function into the definitions of the three currents (26c), (26e), and (26h) yields the expected relations

$$\boldsymbol{j} = n\boldsymbol{u}, \qquad \boldsymbol{j}_I = n_I \boldsymbol{u}, \qquad \boldsymbol{j}_E = \mathcal{W}\boldsymbol{u}, \tag{27a}$$

where $\mathcal{W}$ is the enthalpy density. This thermodynamic quantity can also be evaluated using the local equilibrium distribution function, which yields the "equation of state"

$$\mathcal{W} = n_E + P = \frac{3n_E}{2+u^2/v_g^2}, \tag{27b}$$

where P is the thermodynamic pressure. Both of these quantities appear in the explicit expression of the momentum flux tensor

$$\Pi_E^{\alpha\beta} = P\delta^{\alpha\beta} + \frac{\mathcal{W}}{v_g^2}u^\alpha u^\beta. \tag{27c}$$

Combining Eqs. (27) with the continuity equation for momentum density (26i), one may generalize the Euler equation [168] to Dirac quasiparticles in graphene

$$\mathcal{W}(\partial_t + \boldsymbol{u}\cdot\boldsymbol{\nabla})\boldsymbol{u} + v_g^2\boldsymbol{\nabla}P + \boldsymbol{u}\partial_t P + e(\boldsymbol{E}\cdot\boldsymbol{j})\boldsymbol{u} = v_g^2\left[en\boldsymbol{E} + \frac{e}{c}\boldsymbol{j}\times\boldsymbol{B}\right] - \frac{\mathcal{W}\boldsymbol{u}}{\tau_{\rm dis}}. \tag{28}$$

It is instructive to compare Eq. (28) to the relativistic version of the Euler equation, Eq. (13a). Formally, the first three terms in the LHS of Eq. (28) coincide with the three terms of Eq. (13a). The rest of the terms—the Joule's heat, Lorentz force, and weak decay due to disorder—have not been considered in the relativistic theory and are explicitly not Lorentz-invariant. Even though the first three terms in Eq. (28) have the same form as Eq. (13a), there is a subtle difference: the pressure p in Eq. (13a) is the thermodynamic pressure in the local rest frame, while P in Eq. (28) is the pressure in the laboratory frame. The latter is evaluated with the distribution function (21) and hence is a function of the velocity $\boldsymbol{u}$, while $p = P(\boldsymbol{u} = 0)$. This point is the only difference between the relativistic equation of state (13c) and Eq. (27b) as well.

The generalized Euler equation (28) together with the continuity equations (26a), (26d), and (26f) describe the "ideal" flow of the electronic fluid. In conventional hydrodynamics "ideal" means "in the absence of dissipation", which is not quite the case here, since weak disorder scattering, quasiparticle recombination, and energy relaxation are already taken into account. However, none of these processes are due to electron–electron interaction and hence are absent in the conventional theory [13].

3.2.4 Dissipative corrections

In its simplest form, conventional hydrodynamics [13, 16] considers a system of particles (atoms, molecules, etc.) with the contact (short-range) interaction, such that individual scattering processes are almost literally "collisions". These collisions represent the physical process responsible for equilibration: if the system is driven out of equilibrium, they tend to restore it. In the process, the system is bound to lose energy, hence the collisions are responsible for dissipation.

In graphene (and other solids, see below), the situation is slightly more involved, but the main idea remain the same—physical processes responsible for equilibration

lead to dissipation that is described by "kinetic coefficients". This can be described as follows [13, 16]. Nonequilibrium states are characterized by nonzero macroscopic current. In the process of equilibration the currents relax (their values are being reduced towards zero). Hence, the quasiparticle currents (27a) acquire additional terms—the dissipative corrections [23, 24, 120, 176]

$$\boldsymbol{j} = n\boldsymbol{u} + \delta\boldsymbol{j}, \qquad \boldsymbol{j}_I = n_I\boldsymbol{u} + \delta\boldsymbol{j}_I. \tag{29a}$$

In the absence of magnetic field, the dissipative corrections are related to external bias by means of a "conductivity matrix" [89, 120, 204]

$$\begin{pmatrix} \delta\boldsymbol{j} \\ \delta\boldsymbol{j}_I \end{pmatrix} = \widehat{\Sigma} \begin{pmatrix} e\boldsymbol{E} - T\boldsymbol{\nabla}(\mu/T) \\ -T\boldsymbol{\nabla}(\mu_I/T) \end{pmatrix}. \tag{29b}$$

At charge neutrality $\mu = \mu_I = 0$ the matrix $\widehat{\Sigma}$ is diagonal. In the absence of disorder, the upper diagonal element defines the "quantum" or "intrinsic" conductivity [23, 24, 89, 120, 204]

$$\sigma_Q = e^2\Sigma_{11}(0). \tag{29c}$$

The third current $\boldsymbol{j}_E$ does not acquire a dissipative correction since it is proportional to the momentum density, see Eq. (26h), and electron–electron interaction conserves momentum. This point represents the key difference between electronic hydrodynamics in graphene (or any semimetal with linear spectrum) from conventional fluid mechanics of systems with parabolic (Galilean-invariant) spectrum. In the latter case, it is the particle number (or mass) current $\boldsymbol{j}$ that is proportional to the momentum density. As a result, the energy current gets a dissipative correction described by the thermal conductivity $\varkappa$ that is determined by interparticle collisions. In the hydrodynamic theory of graphene, the role that is equivalent to that of $\varkappa$ is played by the elements of the matrix $\widehat{\Sigma}$. The matrix nature of $\widehat{\Sigma}$ reflects the band structure of graphene. In the case of strong recombination, the imbalance mode becomes irrelevant and one is left with the single dissipative coefficient σ_Q, see Ref. [24]. Now, the thermal conductivity in graphene arises purely due to weak disorder scattering that is already taken into account in the Euler equation (28). This is the reason for the strong violation of the Wiedemann–Franz law in neutral graphene, see Sect. 2.5.1.

The kinetic coefficients $\widehat{\Sigma}$ can be found by solving the kinetic equation (20a) perturbatively using the standard procedure [16, 24, 121, 147]. In a bulk system and in the absence of magnetic field, this calculation was performed in detail in Ref. [120], where a 3×3 matrix was considered [i.e., adding the energy current and its relaxation due to weak disorder to Eq. (29b)]. The following 2×2 matrix was introduced in Ref. [176]. In both cases, one expresses the matrix $\widehat{\Sigma}$ as a linear combination of the interaction and disorder contributions

$$\widehat{\Sigma} = \widehat{\mathfrak{m}}\,\widehat{\mathfrak{S}}_{xx}^{-1}\widehat{\mathfrak{m}}, \qquad \widehat{\mathfrak{S}}_{xx} = \frac{\alpha_g^2 T^2}{2\mathcal{T}^2}\widehat{\mathfrak{T}} + \frac{\pi}{\mathcal{T}\tau_{\mathrm{dis}}}\widehat{\mathfrak{m}}, \tag{30a}$$

where (following the 2×2 notation)

$$\widehat{\mathfrak{m}}=\begin{pmatrix} 1-\frac{2\tilde{n}^2}{3\tilde{n}_E}\frac{T}{\mathcal{T}} & \frac{xT}{\mathcal{T}}-\frac{2\tilde{n}\tilde{n}_I}{3\tilde{n}_E}\frac{T}{\mathcal{T}} \\ \frac{xT}{\mathcal{T}}-\frac{2\tilde{n}\tilde{n}_I}{3\tilde{n}_E}\frac{T}{\mathcal{T}} & 1-\frac{2\tilde{n}_I^2}{3\tilde{n}_E}\frac{T}{\mathcal{T}} \end{pmatrix}, \tag{30b}$$

with dimensionless densities (in self-evident notation; $Li_n(z)$ is the polylogarithm)

$$\tilde{n}=\mathrm{Li}_2\left(-e^{-x}\right)-\mathrm{Li}_2\left(-e^{x}\right),\quad \tilde{n}_I=\frac{x^2}{2}+\frac{\pi^2}{6},\quad \tilde{n}_E=-\mathrm{Li}_3\left(-e^{x}\right)-\mathrm{Li}_3\left(-e^{-x}\right),$$

$$x=\mu/T,\quad \mathcal{T}=2T\ln\left[2\cosh(x/2)\right], \tag{30c}$$

and dimensionless scattering rates

$$\widehat{\mathfrak{T}}=\begin{pmatrix} t_{11}^{-1} & t_{12}^{-1} \\ t_{12}^{-1} & t_{22}^{-1} \end{pmatrix},\qquad t_{ij}^{-1}=\frac{8\pi\mathcal{T}}{\alpha_g^2 NT^2}\tau_{ij}^{-1}. \tag{30d}$$

Here τ_{ij}^{-1} represent the integrated collision integral appearing while solving the kinetic equation within the three-mode approximation [120, 121, 153, 174]. The fact that the collision integrals can be represented by the effective scattering rates τ_{ij}^{-1} is not equivalent to the simplest τ approximation that was employed above for the collision integrals $\mathrm{St}_{\mathrm{dis}}$ and St_R. Instead, this is simply a manifestation of the dimensionality of a collision integral (that is inverse time).

The numerical values of the scattering rates (30d) were discussed in Ref. [206]. In particular, at charge neutrality the off-diagonal elements vanish, $t_{12}^{-1}(0)=0$. The diagonal element $t_{11}^{-1}(0)$ determines the "intrinsic" or "quantum" conductivity matrix, σ_Q. For small $x\ll 1$ the dimensionless "scattering rates" t_{ij} have the form [206]

$$\frac{1}{t_{11}}=\frac{1}{t_{11}^{(0)}}+x^2\left(\frac{1}{t_{11}^{(2)}}-\frac{1}{8\ln 2}\frac{1}{t_{11}^{(0)}}\right)+\mathcal{O}(x^3), \tag{31a}$$

$$\frac{1}{t_{12}}=\frac{x}{t_{12}^{(1)}}+\mathcal{O}(x^3), \tag{31b}$$

$$\frac{1}{t_{22}}=\frac{1}{t_{22}^{(0)}}+x^2\left(\frac{1}{t_{22}^{(2)}}-\frac{1}{8\ln 2}\frac{1}{t_{22}^{(0)}}\right)+\mathcal{O}(x^3). \tag{31c}$$

For unscreened Coulomb interaction, the dimensionless quantities $t_{ij}^{(0,1,2)}$ are independent on any physical parameter. Numerically, one finds the values [176] (neglecting the small exchange contribution [191]):

$$\left(t_{11}^{(0)}\right)^{-1}\approx 34.63,\quad \left(t_{11}^{(2)}\right)^{-1}\approx 5.45,$$
$$\left(t_{12}^{(1)}\right)^{-1}\approx 5.72,\quad \left(t_{22}^{(0)}\right)^{-1}\approx 19.73,\quad \left(t_{22}^{(2)}\right)^{-1}\approx 5.65.$$

In the case of screened interaction, the quantities $t_{ij}^{(0,1,2)}$ depend on the screening length.

The above values for the effective scattering rates yield the following value for the intrinsic conductivity

$$\sigma_Q = \mathcal{A}e^2/\alpha_g^2, \qquad \mathcal{A} \approx 0.12. \tag{32}$$

The quantity σ_Q was studied by multiple authors [24, 120–123, 147, 152, 153, 191] and is a temperature-dependent constant. This temperature dependence appears due to the logarithmic renormalization of the coupling constant α_g [179].

The above theoretical values can be related to the experimental data of Ref. [43]. Using the value of the coupling constant $\alpha_g \approx 0.23$ that is consistent with measurements at charge neutrality, the dimensionfull scattering rates at a typical temperature $T = 267\,\mathrm{K}$ have the following values

$$\tau_{11}^{-1} \approx 7.35\,\mathrm{THz}, \qquad \tau_{22}^{-1} \approx 4.17\,\mathrm{THz}.$$

The disorder scattering rate at $T = 267\,\mathrm{K}$ can be estimated as

$$\tau_{\mathrm{dis}}^{-1} \approx 0.8\,\mathrm{THz}.$$

In the opposite limit of strongly doped graphene, $x \gg 1$, all elements of the matrix (30d) coincide approaching the value [120, 176, 206]

$$t_{ij}^{-1}(\mu \gg T) \to \frac{8\pi^2}{3}. \tag{33a}$$

The reason for this is the exponentially small contribution of the second band in which case the two currents $\boldsymbol{j}$ and $\boldsymbol{j}_I$ coincide. In this limit, the corresponding dimensionfull rate vanishes

$$\tau_{11}^{-1} \approx \frac{\pi N \alpha_g^2 T^2}{3\mu}, \tag{33b}$$

leading to the vanishing dissipative corrections to the quasiparticle currents

$$\delta \boldsymbol{j} = \delta \boldsymbol{j}_I \to 0. \tag{34}$$

As a result, electric current has the hydrodynamic form (3) leading to the use of the hydrodynamic approach to electronic transport in doped graphene, both theoretically [95, 96, 100, 101, 207] and experimentally [27, 41, 42, 51]

In the presence of magnetic field or in confined geometries the dissipative corrections to quasiparticle currents are more complicated. External magnetic field entangles all three modes and hence the corrections to quasiparticle currents acquire a dependence on the hydrodynamic velocity $\boldsymbol{u}$ [120]. In confined geometries, the coordinate

dependence of the distribution function becomes important and as a result the dissipative corrections (29) become non-uniform [125]. In that case, the usual local conductivity may become poorly defined [53, 125], but the issue remains insufficiently explored.

3.2.5 Electronic viscosity

Dissipative processes also contribute a correction to the momentum flux (stress-energy) tensor (26j). In the non-relativistic limit, one writes the dissipative correction to $\Pi_E^{\alpha\beta}$ [here $\Pi_{E,0}^{\alpha\beta}$ denotes the tensor given in Eq. (27c)]

$$\Pi_E^{\alpha\beta} = \Pi_{E,0}^{\alpha\beta} + \delta\Pi_E^{\alpha\beta}, \tag{35a}$$

to the leading order in gradient expansion as

$$\delta\Pi_E^{\alpha\beta} = \eta^{\alpha\beta\gamma\delta}\nabla^\gamma u^\delta, \tag{35b}$$

where $\eta^{\alpha\beta\gamma\delta}$ is the rank-four viscosity tensor [13]. In a fully rotationally invariant system the explicit form of the viscosity tensor is dictated by symmetry and in 2D is given by

$$\eta^{\alpha\beta\gamma\delta} = \eta\left(\delta^{\alpha\gamma}\delta^{\beta\delta} + \delta^{\alpha\delta}\delta^{\beta\gamma}\right) + (\zeta - \eta)\delta^{\alpha\beta}\delta^{\gamma\delta}, \tag{35c}$$

where η and ζ are the shear and bulk viscosity, respectively.

In graphene, the bulk viscosity vanishes, at least to the leading approximation [23, 24, 113, 121, 152], similarly to the situation in ultrarelativistic systems [16, 208] and Fermi liquids [26, 209] (although it may appear in disordered systems in magnetic field [210]). As a result, the leading term of the gradient expansion of the dissipative stress tensor has the form [13, 119, 120]

$$\delta\Pi_E^{\alpha\beta} = -\eta\mathfrak{D}^{\alpha\beta}, \tag{35d}$$

where

$$\mathfrak{D}^{\alpha\beta} = \nabla^\alpha u^\beta + \nabla^\beta u^\alpha - \delta^{\alpha\beta}\boldsymbol{\nabla}\cdot\boldsymbol{u}. \tag{35e}$$

In the presence of magnetic field, the shear viscosity acquires a field dependence [109, 110, 165] and the correction to the stress tensor gains an additional contribution

$$\delta\Pi_E^{\alpha\beta} = -\eta(B)\mathfrak{D}^{\alpha\beta} + \eta_H(B)\epsilon^{\alpha ij}\mathfrak{D}^{i\beta}e_B^j, \tag{35f}$$

where $\boldsymbol{e}_B = \boldsymbol{B}/B$ and $\eta_H(B)$ is the Hall [109, 110, 113, 120, 165, 211–214] viscosity. While the sign of η is fixed by thermodynamics [13, 16], the sign of η_H is not. Equation (35f) follows Ref. [42]: the Hall viscosity is positive for electrons [120] (and negative for holes).

Electronic viscosity can be calculated in two different ways. As a linear response function relating stress to strain [211, 215], the viscosity tensor can be found using a Kubo formula [211, 215, 216] (that can be related to the usual Kubo formula for conductivity [211]). Such calculations are mostly perturbative and were used to evaluate viscosity in strongly doped graphene [216] and in the high-frequency (collisionless) regime [215], as well as in disordered 2D electron systems beyond the hydrodynamic regime [217]. A further extension of this approach yields higher order corrections, such as "drag viscosity" [218] (by analogy to Coulomb drag [219]). Alternatively, one can proceed with the solution of the kinetic equation (20a) following the standard procedure [16, 120, 121]. For arbitrary carrier density this yields a somewhat cumbersome expression that can only be analyzed numerically [119], but simplifies in the limiting cases of neutral and strongly doped graphene.

At charge neutrality and in the absence of magnetic field, the only energy scale in the problem is the temperature T and hence the shear viscosity has the form [180]

$$\eta(\mu=0,\, B=0) = \mathcal{B}\frac{T^2}{\alpha_g^2 v_g^2}. \tag{36}$$

The coefficient $\mathcal{B}$ has been evaluated in Ref. [180] to have the value $\mathcal{B} \approx 0.45$. This result was later confirmed in Ref. [120]. In both cases, the numerical value was obtained with the simplest model of unscreened Coulomb interaction, which is valid for small α_g, i.e., in the regime of formal validity of the kinetic approach (as well as the three-mode approximation allowing for nonperturbative results). At realistic parameter values one has to supplement kinetic calculations by the renormalization group (RG) approach treating α_g as a running coupling constant [179–183]. However, the product $\alpha_g v_g$ remains constant along the RG flow [180, 191], such that Eq. (36) represents the correct form of shear viscosity in graphene at low temperatures and $B = 0$ [179].

Experimentally, a measurement of the shear viscosity is nontrivial [140]. However, nonlocal resistance measurements [27] yield an estimate of a related quantity, the kinematic viscosity, see Eq. (2). In graphene, the kinematic viscosity is defined as

$$\nu = \frac{v_g^2 \eta}{\mathcal{W}}. \tag{37}$$

The appearance of the enthalpy density in this definition is a manifestation of the fact that the hydrodynamic flow in graphene is the energy flow, see Eq. (26h). At charge neutrality, the kinematic viscosity is determined by the ratio of the velocity and coupling constant rather than their product [119]

$$\nu(\mu=0,\, B=0) \propto \frac{v_g^2}{\alpha_g^2 T}, \tag{38}$$

and hence is renormalized along the RG flow. In doped graphene, the dominant temperature dependence of the kinematic viscosity can be estimated as [119]

$$\nu(\mu \gg 1, B=0) \propto \frac{v_g^2 \mu}{\alpha_g^2 T^2} \frac{1}{1+T^2/\mu^2}. \tag{39}$$

This expression disregards additional temperature dependence arising from the RG and extra logarithmic factors [24, 119, 216].

Taking into account renormalization and screening effects, one can reach a quantitative estimate of the kinematic viscosity that is of the same order of magnitude as the experimental data reported in Ref. [27], see Fig. 18. Close to charge neutrality, the theoretical results show excellent agreement with the data reported in Ref. [50] as shown in Fig. 11 (see, however, Sect. 2.4.2 for the discussion of the controversial nature of that data).

The field dependence of the shear viscosity was discussed semiclassically in Refs. [42, 109, 110, 165] in the context of a single-component Fermi liquid or strongly doped graphene (where only one band contributes to low-energy physical properties). The resulting behavior is similar to the conventional magnetoconductivity [10]

$$\eta(B; \mu \gg T) = \frac{\eta(B=0; \mu \gg T)}{1+\Gamma_B^2}, \tag{40a}$$

$$\eta_H(B; \mu \gg T) = \eta(B=0; \mu \gg T) \frac{\Gamma_B}{1+\Gamma_B^2}, \tag{40b}$$

where

$$\Gamma_B = 2\omega_B \tilde{\tau}_{11}, \quad \omega_B = |e| v_g^2 B/(\mu c). \tag{40c}$$

The kinetic approach [119] allows one to identify the scattering rate $\tilde{\tau}_{11}$ appearing in Eqs. (40). Indeed, this rate should be distinguished [121, 216] from the transport

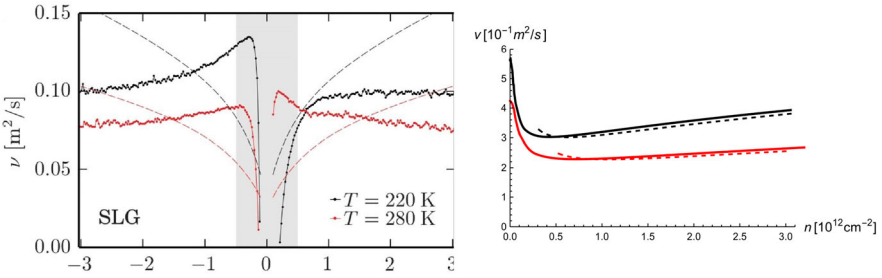

Fig. 18 Kinematic viscosity in monolayer graphene. Left: experimental data of Ref. [27] obtained by means of vicinity resistance measurements, see Sect. 2.2.2 (From Ref. [27]. Reprinted with permission from AAAS). Right: theoretical result of Ref. [119] obtained using the kinetic theory and renormalization group techniques (Reprinted with permission from Ref. [119]. Copyright (2019) by the American Physical Society)

scattering rate [122, 220] that determines the electrical conductivity and the "quantum" scattering rate [122] that determines the quasiparticle lifetime. At the same time, the kinetic theory yields the field dependence of the shear viscosity at charge neutrality as well [119]

$$\eta(B;\mu=0)=\frac{T^2}{\alpha_g^2 v_g^2}\frac{\mathcal{B}+\mathcal{B}_1\gamma_B^2}{1+\mathcal{B}_2\gamma_B^2}, \tag{41}$$

where

$$\gamma_B=\frac{|e|v_g^2 B}{\alpha_g^2 c T^2}, \tag{42}$$

where $\mathcal{B}_1\approx 0.0037$ and $\mathcal{B}_2\approx 0.0274$. In contrast to the Fermi liquid results, the shear viscosity at $\mu=0$ does not vanish in the limit of classically strong field.

Frequency-dependent viscosity was analyzed in Refs. [211, 216, 221]. In particular, Ref. [221] suggested an existence of a resonance in strong magnetic fields (as well as the corresponding plasmon damping). Momentum-dependent viscosity in Fermi liquids (due to head on collisions [222, 223]) was suggested in Ref. [224] (for an alternative approach to viscosity in Fermi liquids see Ref. [225]).

Beyond graphene, in anisotropic Dirac systems [183, 212] one has to consider the full viscosity tensor (these are the systems where two Dirac cones merge in momentum space [226]; this may be relevant to the organic conductor α-(BEDT-TTF)$_2$I$_3$ under pressure [227], the heterostructure of the 5/3 TiO_2/VO_2 supercell [228, 229], surface modes of topological crystalline insulators with unpinned surface Dirac cones [230], and quadratic double Weyl fermions [231]). In the absence of magnetic field, the viscosity matrix contains six independent components (in accordance with the Onsager reciprocity [13, 16]), which scale differently with temperature [183]. In particular, one of the six components vanishes at lowest temperatures violating the famous (conjectured) bound for the shear viscosity to entropy density ratio [232]. As a result, the authors of Ref. [183] proposed a generalization of the bound to anisotropic 2D systems, see Sect. 6. An alternative view on anisotropic Dirac semimetals taking into account spectrum topology (i.e., the Berry curvature) has been developed in Ref. [233]. Hall viscosity in the quantum Hall regime in such systems was discussed in Ref. [234]. More complicated spectra can be encountered in 3D Luttinger semimetals [235] where the long-screened nature of the Coulomb interaction leads to a scale-invariant, non-Fermi-liquid ground state [236]. The hydrodynamic behavior in such systems was considered in Ref. [237].

3.2.6 Hydrodynamic equations in graphene

Taking into account the dissipative corrections in the continuity equations (26), one finds the generalization of the Navier–Stokes equation [13, 90, 91] in graphene

$$\mathcal{W}(\partial_t+\boldsymbol{u}\cdot\nabla)\boldsymbol{u}+v_g^2\nabla P+\boldsymbol{u}\partial_t P+e(\boldsymbol{E}\cdot\boldsymbol{j})\boldsymbol{u}=$$

$$= v_g^2 \left[\eta \Delta \boldsymbol{u} - \eta_H \Delta \boldsymbol{u} \times \boldsymbol{e_B} + en\boldsymbol{E} + \frac{e}{c} \boldsymbol{j} \times \boldsymbol{B} \right] - \frac{\mathcal{W}\boldsymbol{u}}{\tau_{\rm dis}}. \tag{43a}$$

The full set of the hydrodynamic equations contains also the continuity equations

$$\partial_t n + \boldsymbol{\nabla} \cdot \boldsymbol{j} = 0, \tag{43b}$$

and

$$\partial_t n_I + \boldsymbol{\nabla} \cdot \boldsymbol{j}_I = -\frac{n_I - n_{I,0}}{\tau_R}, \tag{43c}$$

and the thermal transport equation [201]

$$\begin{aligned} T \left[\frac{\partial s}{\partial t} + \boldsymbol{\nabla} \cdot \left(s\boldsymbol{u} - \delta \boldsymbol{j} \frac{\mu}{T} - \delta \boldsymbol{j}_I \frac{\mu_I}{T} \right) \right] &= \delta \boldsymbol{j} \cdot \left[e\boldsymbol{E} + \frac{e}{c} \boldsymbol{u} \times \boldsymbol{B} - T \boldsymbol{\nabla} \frac{\mu}{T} \right] \\ - T \delta \boldsymbol{j}_I \cdot \boldsymbol{\nabla} \frac{\mu_I}{T} + \frac{\eta}{2} \left(\nabla^\alpha u^\beta + \nabla^\beta u^\alpha - \delta^{\alpha\beta} \boldsymbol{\nabla} \cdot \boldsymbol{u} \right)^2 \\ - \frac{n_E - n_{E,0}}{\tau_{RE}} + \mu_I \frac{n_I - n_{I,0}}{\tau_R} + \frac{\mathcal{W}\boldsymbol{u}^2}{v_g^2 \tau_{\rm dis}}, \end{aligned} \tag{43d}$$

where s denotes the entropy density. The equation (43d) replaces the continuity equation for the energy density (26f) as is common in hydrodynamics [13]. The hydrodynamic equations are supplemented by the constitutive equations for the quasiparticle currents (29) and the generalized conductivity matrix $\widehat{\Sigma}$, as well as Maxwell's equations for the electromagnetic field, in other words, Vlasov self-consistency [16, 23, 120, 121].

3.2.7 Boundary conditions

The state of a conventional fluid is described by the velocity vector and two thermodynamic quantities, such as density and pressure. The hydrodynamic equations are differential equations containing spatial and time derivatives of these variables. Hence, to find a solution to these equations one has to specify the boundary conditions.

The conventional Navier–Stokes equation [13, 90, 91] greatly simplifies for an incompressible fluid. In this case, the fluid density is a constant, while the pressure gradient can be excluded by applying the curl operation to the equation. The resulting equation is a differential equation for the velocity only.

If a viscous fluid is flowing near a solid, stationary boundary, a simple "no-slip" boundary condition is often assumed [13] (due to the molecular forces acting between the fluid and the boundary). On the other hand, a boundary between a fluid and a gas can be characterized by the "no-stress" boundary condition, where the tangential stress is continuous at the interface. The two conditions can be "unified" as limiting cases of a more general condition due to Maxwell [238]

$$u_t^\alpha \Big|_S = \ell_S \, e_n^\beta \, \frac{\partial u_t^\alpha}{\partial x^\beta} \Big|_S, \tag{44}$$

where $\boldsymbol{e}_n$ is the unit vector normal to the surface, $\boldsymbol{u}_t = \boldsymbol{u} - (\boldsymbol{u}\cdot\boldsymbol{n})\boldsymbol{n}$ is the tangential velocity, and ℓ_S is the so-called "slip length". The no-slip boundary condition, $\boldsymbol{u} = 0$ (the normal component of the velocity has to vanish at any solid boundary by obvious reasons) corresponds to $\ell_S = 0$, while the limit $\ell_S \to \infty$ describes the no-stress case.

In electronic systems, the boundary condition (44) was studied in detail in Ref. [117] based on the kinetic approach. Solving the kinetic equation in the presence of a boundary requires boundary conditions for the distribution function. The latter are well studied [239], especially in the context of mesoscopic physics [11]. Analytic calculations are possible in the two limiting cases of specular and diffusive scattering at the boundary. Boundary conditions in the presence of magnetic field were studied in Ref. [240]. Recently, the issue of the boundary conditions and the slip length in the magnetic field was discussed in Ref. [241].

Specular scattering refers to ideally smooth boundaries such that the incidence and reflection angles (of the quasiparticle velocity) coincide. In that case, the distribution function obeys the simple boundary condition

$$f(\varphi)\Big|_S = f(-\varphi)\Big|_S, \tag{45}$$

where φ is the angle between the quasiparticle (microscopic) velocity $\boldsymbol{v}$ and the boundary. Experimental feasibility of smooth boundaries was recently explored in Ref. [242].

In the diffusive case, the boundary is assumed to be sufficiently rough, such that the incoming quasiparticle can scatter off the boundary in any direction with equal probability (independent of the incidence angle). This can be expressed by a more complex condition. In a channel geometry (see Fig. 19) the corresponding condition has the form [11]

$$f(W/2, -\pi < \varphi < 0) = \frac{1}{2}\int_0^{\pi} d\varphi' \sin\varphi' f(W/2, \varphi'), \tag{46a}$$

$$f(-W/2, 0 < \varphi < \pi)|_S = \frac{1}{2}\int_{-\pi}^{0} d\varphi' \sin\varphi' f(-W/2, \varphi'). \tag{46b}$$

The resulting slip length is strongly influenced by the choice of the boundary conditions for the distribution function [117]. The authors of Ref. [117] express ℓ_S in

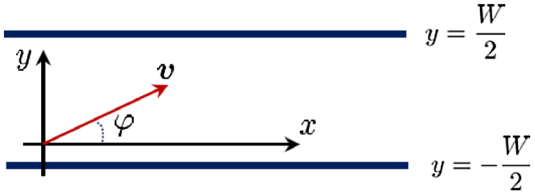

Fig. 19 Channel geometry: the electronic fluid is confined to a channel (along the x-direction) of the width W; $\boldsymbol{v}$ is the quasiparticle velocity directed at the angle φ to the channel boundary

terms of the electron–electron scattering length

$$\ell_S = g(\kappa)\ell_{ee}, \qquad \kappa = \frac{h_1^2 h_2^{d-1}}{\lambda^{d+1}}, \qquad g(\kappa) \to \begin{cases} g_0/\kappa, & \kappa \ll 1, \\ g_\infty, & \kappa \to \infty, \end{cases} \tag{47}$$

where h_1 and h_2 are the mean height and correlation length describing the boundary roughness [239], λ is the (temperature dependent) electron wavelength, and d is the spatial dimensionality. The precise value of $g(\kappa)$ varies dramatically, but at experimentally relevant temperatures one finds $\ell_S \approx 0.5\,\mu$m, the value that agrees with experimental observations, see Ref. [51].

Full solution to the hydrodynamic equations in electronic systems requires also boundary conditions for thermodynamic quantities. In electronic systems, these are most conveniently expressed in terms of electrochemical potentials.

Traditional transport theory is based on a single-electron approach, where the main mechanism of electrical resistance—and hence, dissipation—is the electron–impurity and electron–phonon scattering. In this case, the bulk system is characterized by a local conductivity, while contact interfaces—by the contact resistance. The latter appears due to equilibration of (originally mismatched) electrochemical potentials in the two interfacing materials [243]. The bulk and contact resistances could be seen as independent parts of the overall electrical circuit. If the bulk system is diffusive, the contribution of the contacts is typically negligible. On the contrary, in ballistic systems there is almost no dissipation in the bulk, such that most of the voltage drop occurring in the contacts, see Fig. 9.

In the context of ideal (inviscid) hydrodynamics in nearly neutral graphene, boundary conditions taking into account contact resistance were considered in Ref. [89]. Assuming the leads are represented by a disordered, particle–hole symmetric metal, the electron and hole currents are given by the difference of the electrochemical potentials across the interface divided by the contact resistance. If no electric current is allowed in the system (as is appropriate for measurements of thermal conductivity [24, 89]), this leads to a boundary condition relating the imbalance chemical potential μ_I and the total quasiparticle current $\boldsymbol{j}_I$.

An alternative situation was considered in Ref. [138]. In this paper the authors have considered an idealized situation where a clean (disorder-free), but viscous electron fluid is contacted by an ideal conductor with an ideal interface characterized by the vanishing reflection coefficient [244]. The absence of disorder implies the lack of Ohmic dissipation in the bulk, while the ideal contacts do not provide any contact resistance. In that case the bulk dissipation due to viscosity has to be compensated by the work done by current source. If both the bulk and the contacts are disorder-free, then the electric potential exhibits a sharp inhomogeneity (on the hydrodynamic scale—a jump) in a narrow region close to the interface, which translates into a viscosity-dependent contribution to the contact resistance that can be positive or negative depending on the contact curvature sign.

Real samples are likely to exhibit all of the above effects and moreover may host additional localized charges at the sample edges leading to classical (non-topological) edge currents [53], see Sect. 2.4.3. The appropriate boundary conditions then strongly

depend on sample geometry and the specific measurement scheme. For example, the authors of Ref. [140] suggest using the Corbino disk geometry to measure electronic viscosity. In their setup, the outer edge of the Corbino disk is isolated, implying the vanishing radial component of the electric current. In addition, they required the azimuthal momentum component to diffuse radially, such that the off-diagonal component of the viscous stress tensor vanishes at both edges of the disk. Interestingly enough, the authors of Ref. [140] considered the no-slip boundary conditions as well and found no qualitative difference with the above approach.

3.3 Hydrodynamic collective modes and plasmons

Hydrodynamic collective modes have been considered by many authors [24, 121, 122, 169–176, 245, 246]. The point of consensus is that the ideal (neglecting dissipative processes) electronic fluid in neutral graphene is characterized by a sound-like collective mode (sometimes referred to as the "cosmic sound" [169] or the "second sound" [174]) with the linear dispersion relation

$$\omega = v_g q/\sqrt{2}. \tag{48}$$

In a way, this result justifies the claim that the electronic fluid behave hydrodynamically, see Sect. 1.

Dissipative processes damp the sound mode (48). In contrast to traditional hydrodynamics this happens since dissipation due to "external" scattering (e.g., disorder and electron–phonon scattering) appears already in the description of an "ideal" (i.e., inviscid) electronic fluid, see Eqs. (26d), (26f), and (28). Another issue is the regime of applicability of the dispersion relation (48) or its damped counterparts. The point is that hydrodynamics is based on the gradient expansion valid at length scales that are much larger than ℓ_{ee} (representing the energy and momentum conserving interaction responsible for equilibration). At smaller length scales, other, more conventional collective excitations, such as plasmons [121, 170, 171, 173–175, 247–262], may be identified.

3.3.1 Electronic "sound" in neutral graphene

Collective excitations in the electronic system in graphene have been recently studied in detail in Ref. [176]. At charge neutrality and in the absence of magnetic field, the sound mode (48) damped by the dissipative processes has the dispersion relation

$$\omega = \sqrt{\frac{v_g^2 q^2}{2} - \frac{1}{4}\left(\frac{1+q^2\ell_G^2}{\tau_{\rm dis}} - \frac{1}{\tau_{RE}}\right)^2} - i\,\frac{1+q^2\ell_G^2}{2\tau_{\rm dis}} - \frac{i}{2\tau_{RE}}, \tag{49}$$

where ℓ_G is the Gurzhi length (8). Although Eq. (49) can be straightforwardly derived by linearizing the hydrodynamic equations (43), the damping in Eq. (49) can be seen as exceeding the accuracy of the hydrodynamic regime. Indeed, the gradient expansion

in neutral graphene is justified for momenta smaller than a certain scale defined by the electron–electron interaction

$$q\ell_{\rm hydro} \ll 1, \quad \ell_{\rm hydro} \sim \frac{v_g}{\alpha_g^2 \bar{T}}. \tag{50}$$

Assuming a clean system $\tau_{\rm dis} \to \infty$ (energy relaxation due to supercollisions [201] may be also neglected, $\tau_{RE} \gg \tau_{\rm dis}$), the expression under the square root in Eq. (49) can be expanded for small q as

$$\frac{v_g^2 q^2}{2} - \frac{\left(1+q^2\ell_G^2\right)^2}{4\tau_{\rm dis}^2} \to \frac{v_g^2 q^2}{2}\left[1 - Aq^2\ell_{\rm hydro}^2 - \mathcal{O}(\tau_{\rm dis}^{-1})\right],$$

where A is a numerical coefficient. Hence, within the hydrodynamic approach, the viscous contribution to damping should be neglected, leaving one with the simpler dispersion [121]

$$\omega = \sqrt{\frac{v_g^2 q^2}{2} - \frac{1}{4\tau_{\rm dis}^2}} - \frac{i}{2\tau_{\rm dis}}. \tag{51}$$

Now, the peculiar nature of the Dirac spectrum in graphene leads to the fact that the linearized version of the hydrodynamic equations is justified in a wider parameter region than Eqs. (43) themselves [121, 124, 192, 206] (due to the "collinear scattering singularity" [23, 24, 121, 153]). In the weak coupling limit, the linear response theory is valid at much larger momenta

$$q\ell_{\rm coll} \ll 1, \quad \ell_{\rm coll} \sim \frac{v_g}{\alpha_g^2 \bar{T} |\ln \alpha_g|} \ll \ell_{\rm hydro}, \tag{52}$$

formally providing one with a justification to extend Eq. (49) beyond the hydrodynamic regime. However, already at $q\ell_{\rm hydro} \sim 1$ the imaginary part of the sound dispersion becomes comparable to the real part, at which point the dispersion is no longer observable.

The nature of the sound mode (48) [or Eq. (49)] becomes clear if one takes into account the fact that in neutral graphene in the absence of magnetic field the electric charge is decoupled from the hydrodynamic energy flow. Indeed, at charge neutrality $n = 0$ so that the electric field does not enter the linearized Navier–Stokes equation (43a), while the "conductivity matrix" in Eqs. (29) is diagonal. Hence, the energy flow is described by the Navier–Stokes equation (43a), while charge transport is described by the Ohmic relation (29b), together with the Vlasov self-consistency. The latter can be expressed using the Poisson's equation

$$\boldsymbol{E}_V = -e\nabla \int d^2 r' \frac{\delta n(\boldsymbol{r}')}{|\boldsymbol{r} - \boldsymbol{r}'|}. \tag{53a}$$

In gated structures [87, 263], this can be simplified to

$$\boldsymbol{E}_V = -\frac{e}{C}\nabla\delta n(\boldsymbol{r}), \tag{53b}$$

where $C = \varepsilon/(4\pi d)$ is the gate-to-channel capacitance per unit area, d is the distance to the gate, and ε is the dielectric constant. This approximation neglects the long-ranged (dipole-type) part of the screened Coulomb interaction and is justified while the charge density $n(\boldsymbol{r})$ varies on length scales exceeding d.

The charge sector of the theory is characterized by an overdamped collective mode with the dispersion

$$\omega = -iD_0q^2\left[1+eV_s(q)\frac{\partial n}{\partial\mu}\right], \quad D_0 = \frac{1}{2}\frac{v_g^2\tau_{11}\tau_{\rm dis}}{\tau_{11}+\tau_{\rm dis}}. \tag{54}$$

In a gated structure, the mode is diffusive (with the Vlasov self-consistent potential $V_s = e/C$ providing a correction to the diffusion coefficient). For long-range Coulomb interaction (here $V_s = 2\pi e/q$), the dispersion remains purely imaginary with $\omega \sim iq$ at small q.

3.3.2 Electronic "sound" in doped graphene

In doped graphene, the charge and energy modes are coupled by the Vlasov self-consistency [176]. To the leading order in (weak) energy relaxation this leads to a sound mode similar to Eq. (49) and a diffusive mode that in a gated structure has the dispersion

$$\omega = -\frac{i}{\tau_{RE}}\frac{\varkappa v_g^2q^2}{(\varkappa+2\pi C)v_g^2q^2+4\pi C\tau_{RE}^{-1}\tau_{\rm dis}^{-1}}, \tag{55}$$

where the Thomas–Fermi screening length is given by

$$\varkappa = N\alpha_g k_F = Ne^2\mu/v_g^2. \tag{56}$$

For long-range Coulomb interaction, the factor $2\pi C$ should be replaced with q. Physically, the mode (55) describes energy diffusion appearing due coupling of the charge and energy fluctuations by Vlasov self-consistency.

For a gated structure, the sound mode coincides with the "cosmic sound" (48) at the lowest momenta, albeit with the sound velocity modified by screening. In the case of long-range Coulomb interaction the dispersion is no longer sound-like. In the limit $q \to 0$ (and $\mu \gg T$), one finds the spectrum similar to the usual 2D plasmon [12, 121]

$$\omega(q \ll \varkappa) = -\frac{i}{2\tau_{\rm dis}} + \sqrt{\frac{1}{2}v_g^2q\varkappa - \frac{1}{4\tau_{\rm dis}^2}}. \tag{57}$$

The expression (57) is valid when

$$q\ell_G \ll 1, \quad q \ll \varkappa, \quad v_g^2 \varkappa q \tau_{\rm dis}^2 \gg 1.$$

These conditions are consistent with the applicability condition of the hydrodynamic approach if

$$\begin{aligned} v_g \varkappa \tau_{\rm dis} \gg 1 \quad &\Rightarrow \quad N\alpha_g \mu \tau_{\rm dis} \gg 1, \\ \ell_G \ll v_g^2 \varkappa \tau_{\rm dis}^2 \quad &\Rightarrow \quad N^2 \alpha_g^4 \mu \tau_{\rm dis} (\bar{T}\tau_{\rm dis})^2 \gg 1. \end{aligned}$$

The above conditions provide a possibility to observe the dispersion (57) in a parametrically defined range of wavevectors.

3.3.3 Hydrodynamic modes and plasmons

The above sound-like modes have to be distinguished from plasmonic excitations in electronic systems. The latter are well studied, also in graphene [121, 170, 173–175, 247–262]. In a degenerate electron gas in 2D, the plasmon dispersion (neglecting impurity scattering, i.e., $\tau_{\rm dis} \to \infty$) has the form [247]

$$\omega = \sqrt{2e^2 \mu q}\left(1 + \gamma \frac{q}{\varkappa}\right), \tag{58}$$

where γ is a numerical coefficient, that can be evaluated either within the random phase approximation (i.e., by computing the Lindhard function; this leads to $\gamma = 3/4$ [247]), or using a macroscopic (hydrodynamic-like) theory. The latter approach yields a different value of γ which is typically attributed to the fact that hydrodynamics is applicable at small momenta ($q\ell_{\rm hydro} \ll 1$) and frequencies, while plasmons are nonequilibrium excitations that belong to higher momenta [247]. Based on this argument one might expect that the hydrodynamic collective modes and plasmons simply have nothing to do with each other [171]. Yet, given the same leading momentum dependence in Eqs. (57) and (58), the relation between the two is worth investigating.

In graphene, the possibility of discussing momenta exceeding $1/\ell_{\rm hydro}$ is afforded by the collinear scattering singularity [23, 24, 120–122, 124, 152, 153, 192] which leads to the existence of two parametrically different length scales, see Eq. (52), and hence of an intermediate momentum range, $\ell_{\rm hydro}^{-1} \ll q \ll \ell_{\rm coll}^{-1}$. Here a linear response theory of Ref. [124] can be used to find the collective modes. Remarkably, macroscopic equations of this theory coincide with the linearized hydrodynamic equations [176] such that the resulting dispersions should be valid in the hydrodynamic regime as well and can be compared with the above results.

In doped graphene, the electron system is degenerate and the linear response theory of Ref. [124] can be expressed in terms of a single equation

$$\frac{\partial \boldsymbol{J}}{\partial t} + \frac{v_g^2}{2}\nabla\rho - \nu\Delta\boldsymbol{J} - \frac{v_g^2}{2}\frac{\partial n}{\partial \mu} e^2 \boldsymbol{E} = -\frac{\boldsymbol{J}}{\tau_{\rm dis}}, \tag{59}$$

where $\boldsymbol{J}$ is the electric current, see Eq. (1), and ρ denotes the charge density. Taking into account the Vlasov field (53) and continuity equation, one finds the collective mode with the spectrum

$$\omega = \sqrt{2e^2\mu q\left(1+\frac{q}{\varkappa}\right) - \frac{(1+q^2\ell_G^2)^2}{4\tau_{\rm dis}^2}} - \frac{i(1+q^2\ell_G^2)}{2\tau_{\rm dis}}, \tag{60}$$

where $D = v_g^2\tau_{\rm dis}/2$ and $\sigma = v_g^2(\partial n/\partial\mu)\tau_{\rm dis}/2$ are the diffusion coefficient and the Drude conductivity.

The spectrum (60) is exactly the same as the screened sound mode leading to Eq. (57). In the limit $\tau_{\rm dis}\to\infty$, one may expand Eq. (60) in small $q\to 0$. This yields Eq. (58) with the "wrong" coefficient, $\gamma = 1/2$. At the same time, the leading term (at $q \ll \varkappa$) agrees with the Fermi liquid result in the presence of disorder [12] (in the absence of viscosity). The dispersion (60) is valid for $q\ell_{\rm coll} \ll 1$, however, becomes overdamped already at $q \sim \ell_{\rm hydro}^{-1}$. For $q \gg \ell_{\rm coll}^{-1}$, the quasi-equilibrium description leading to Eq. (59) breaks down and true plasmons with the dispersion (58) emerge. At these momenta the spectrum (60) is purely imaginary. Based on this argument, the authors of Ref. [176] argue that the two modes are not connected. Similar conclusions were reached in Ref. [173], where it was argued that Coulomb interaction precludes the appearance of hydrodynamic sound in Fermi liquids.

In graphene at charge neutrality, the "true" plasmon dispersion was established in Ref. [122] on the basis of microscopic theory. The leading behavior of the plasmon dispersion is given by

$$\omega = \sqrt{(4\ln 2)e^2Tq}. \tag{61}$$

This expression can be compared to the results of the linear response theory in graphene [124, 176]. The linear response theory of Ref. [124] is based on the same three-mode approximation as the hydrodynamics discussed in Sect. 3.2. Similarly to the discussion in Sect. 3.3.1, at charge neutrality the charge sector decouples from the rest of the theory and can be described by the equation

$$\frac{\partial \boldsymbol{j}}{\partial t} + \frac{v_g^2}{2}\nabla n - \frac{2\ln 2}{\pi}e^2T\boldsymbol{E} = -\frac{\boldsymbol{j}}{\tau_{\rm dis}} - \frac{\boldsymbol{j}}{\tau_{11}}, \tag{62}$$

where τ_{11} determines the quantum conductivity (32), see also Eqs. (29) and (30). Combining Eq. (62) with the continuity equation one finds

$$\omega^2 + i\omega\left(\frac{1}{\tau_{\rm dis}} + \frac{1}{\tau_{11}}\right) = \frac{v_g^2}{2}q^2 + (4\ln 2)e^2Tq, \tag{63a}$$

leading to the plasmon-like spectrum that can be expressed similarly to Eq. (54)

$$\omega = -i\frac{\sigma(\omega)q^2}{e^2\partial n/\partial\mu}\left[1 + eV_s(q)\frac{\partial n}{\partial\mu}\right], \tag{63b}$$

where $\sigma(\omega)$ is the optical conductivity [206] [in contrast to the static conductivity (32) in Eq. (54]

$$\sigma(\omega) = \frac{2e^2 T \ln 2}{\pi} \frac{1}{-i\omega + \tau_{11}^{-1} + \tau_{\rm dis}^{-1}}. \tag{63c}$$

In the hydrodynamic regime of small frequencies, $\sigma(\omega \to 0) \to \sigma_0$, the mode (63b) is purely diffusive recovering Eq. (54).

Resolving Eq. (63a) one finds the plasmon dispersion in the form

$$\omega = -i\frac{\tau_{\rm dis}+\tau_{11}}{2\tau_{\rm dis}\tau_{11}} + \sqrt{(4\ln 2)e^2 T q + \frac{v_g^2}{2}q^2 - \frac{(\tau_{\rm dis}+\tau_{11})^2}{4\tau_{\rm dis}^2\tau_{11}^2}}\,. \tag{63d}$$

For $\omega \gg \tau_{11}^{-1} \gg \tau_{\rm dis}^{-1}$ and $q \to 0$, the leading behavior in Eq. (63d) coincides with Eq. (61). At large momenta the first term in the RHS of Eq. (63a) dominates and the dispersion resembles the hydrodynamic sound, Eq. (48). This contradicts the results of Ref. [122]: although at large q the true dispersion also becomes linear, the coefficient (analogous to the speed of sound) is different (there is no factor of $\sqrt{2}$).

To summarize, the plasmon mode (63d) should be contrasted with the diffusive charge mode (54), and not the sound mode (49). The plasmon and the sound belong largely to different frequency regimes [171], but most importantly, stem from the two different, decoupled sectors of the theory (the sound mode can also be obtained from the linear response theory hence one can extend its region of applicability beyond the hydrodynamic regime). The latter fact is the reason why the plasmon dispersion is independent of viscosity, while the sound mode (49) is unaffected by screening effects (which are essentially responsible for plasmon excitations). Formally, the two modes coexist but are characterized by different frequencies that are much higher for the plasmon mode. Approximately at $q \sim \ell_{\rm coll}^{-1}$, i.e., at the applicability limit of the linear response theory, the sound mode becomes overdamped, which does not happen to the plasmon. At that point the plasmon dispersion is almost linear albeit with the coefficient that disagrees with the microscopic theory [122], as pointed out above.

An alternative approach to plasmons is to consider the electromagnetic response of the 2D electron fluid to the high-frequency field generated by a Hertzian dipole [264]. For small enough frequencies ($\omega\tau_{ee} \ll 1$) the electron system responds hydrodynamically. Coupling the hydrodynamic equations with the 3D Maxwell's equations one can define a boundary value problem yielding the full description of the spatial structure of the electromagnetic field. In particular, the numerical analysis of Ref. [264] suggests co-existence between the plasmon and diffusive modes in a way that is somewhat different from the above solution of the purely hydrodynamic problem (where the electromagnetic field was assumed to be static). For analytic analysis of edge magnetoplasmons (using the Wiener–Hopf technique) see Ref. [265].

4 Known solutions to hydrodynamic equations in electronic systems

Once equipped with the hydrodynamic equations and boundary conditions, one may embark on finding solutions in an attempt to either explain or predict experimental observations. Since most transport measurements in solids are performed within linear response, many authors consider solutions to linearized hydrodynamic equations.

Hydrodynamic charge flow in doped graphene (more generally, in hydrodynamic Fermi liquids) was considered analytically in Refs. [37, 94–96, 101, 109, 110, 207, 266] and numerically in Refs. [93, 97, 98]. Neutral graphene (more generally, compensated semimetals) was analyzed in Refs. [85, 87, 114, 115, 125, 199, 267].

Nonlocal transport properties observed in doped graphene [27, 41, 42] were studied in Refs. [94, 95] focusing on the appearance of vortices (or "whirlpools") in viscous flows in confined geometries, the effect that is responsible for the observed negative nonlocal resistance [27]. A purely analytic approach to that problem (albeit in an idealized geometry) was offered in Refs. [96, 207]. The authors of Ref. [96] hinted on the possibility to observe multiple vortices, the effect that was further explored numerically in Ref. [93] (see Fig. 5), where a *sign-alternating* nonlocal resistance was suggested as a consequence. The latter is especially important given that negative nonlocal resistance is not a unique characteristic of the viscous flow and can be observed in ballistic systems [41, 100]. Interestingly enough, complicated patterns of multiple vortices may arise also in nearly neutral graphene with long-ranged disorder [267]. Further complications with the hydrodynamic interpretation of the observed nonlocal resistance and the associated vorticity were discussed in Ref. [268], where it was argued that nonlocal (i.e., momentum-dependent) conductivity in disordered electron systems may mimic the hydrodynamic effects even in the absence of electron–electron interaction [the idea is to interpret Eq. (2) as the Ohm's law with nonlocal conductivity]. However, extracting the viscosity from the nonlocal conductivity obtained by means of the Kubo formula [211] might not be straightforward in disordered systems [217]. Moreover, it is unclear why should one use the hydrodynamic "no-slip" boundary conditions [which are needed to obtain Poiseuille-like solutions from Eq. (2)] in conventional disordered systems outside of the hydrodynamic regime.

An alternative measurement providing indirect evidence of hydrodynamic behavior, namely superballistic transport through a point contact [39] was discussed theoretically in Refs. [37, 101]. Reference [37] provided a detailed analysis of the hydrodynamic theory in the slit geometry comparing the results to those of the ballistic and diffusive (Ohmic) behavior. The authors of Ref. [37] concluded that the hydrodynamic regime represents a relatively narrow intermediate parameter region between the two more conventional regimes (namely, the diffusive and ballistic). Further analysis of a viscous flow through a constriction and the related enhancement of conductivity was reported in Ref. [269].

Now, one of the most popular geometries to consider hydrodynamic effects is the channel (or slab) geometry, see Figs. 9 and 19. The reason for this is the wide spread of the Hall bar geometry of the experimental samples, see Figs. 2 and 4, as well as simplicity of theoretical solution, since assuming a long channel all physical quantities depend only on the coordinate along the channel (the x-coordinate in the notations adopted in Fig. 19). Assuming the no-slip boundary conditions, one finds the solution

to the Navier–Stokes equation in the form of the catenary curve, which reduces to the standard Poiseuille flow [13, 116, 270] in the limit of the large Gurzhi length, $\ell_G \gg W$ (where W is the channel width).

In doped graphene, the electric current is hydrodynamic and is expected to exhibit this behavior [94], with

$$J_x = \sigma_0 E_x \left[1 - \frac{\cosh y/\ell_G}{\cosh W/[2\ell_G]} \right], \tag{64}$$

where J_x and E_x are the components of the current density and electric field along the channel and σ_0 is the Drude conductivity (due to, e.g., disorder). This effect was later observed in the imaging experiment of Ref. [51]. If the system is subjected to the magnetic field, then increasing the field decreases the viscosity, see Eqs. (40), and hence the Gurzhi length (8) leading to *negative* magnetoresistance (suggested theoretically in Refs. [109, 110] and observed experimentally in Ref. [42]). These effects were also considered within the two-fluid hydrodynamic model in Ref. [114]. For an alternative theory of the electronic flows in narrow channels in magnetic fields describing the interplay of electron–electron interactions, disorder, and boundary conditions that goes beyond the hydrodynamic description, see Ref. [240]. For a detailed discussion of the Hall voltage and more generally the role of Hall viscosity in 2D Fermi liquids see Ref. [271]. The case of long-range disorder (or general inhomogeneity of the medium) was considered in Refs. [266, 272, 273], where a positive bulk magnetoresistance was found due to the absence of the Hall voltage [273]. The latter point is reminiscent of the situation in graphene at charge neutrality (other than the boundary effects).

In neutral graphene, the picture is more complicated due to decoupling of the charge and energy flows in the absence of magnetic field. In that case, the hydrodynamic, Poiseuille-like flow is expected for the energy current [183], while the charge transport exhibits the usual diffusion with the quantum conductivity (32) due to electron–electron interaction instead of the standard Drude conductivity due to disorder. Applying external magnetic field naively leads to a positive, parabolic magnetoresistance. This is because the bulk electric current in neutral graphene is accompanied by the lateral quasiparticle (and energy) current (which in turn leads to the geometric magnetoresistance). However, due to the compensated Hall effect and quasiparticle recombination, see Sect. 3.2.1, there is a strong boundary effect changing that behavior and leading to nonsaturating, linear magnetoresistance (at charge neutrality) [87] that is somewhat similar to the edge effects considered in Ref. [86, 274]. The key point is that the above bulk effect is incompatible with finite size geometry: assuming that the bulk current is flowing along the channel, the lateral quasiparticle current must flow across the channel and hence must vanish at both boundaries. The resulting inhomogeneity of the individual electron and hole currents is inconsistent with the standard geometric magnetoresistance. Moreover, this inhomogeneity is only compatible with the continuity equation for the total quasiparticle density, Eq. (26d), if one takes into account recombination. The resulting quasiparticle density is practically uniform in the bulk (characterized by the parabolic geometrical magnetoresistance), but is strongly inhomogeneous in boundary regions of the width of the recombination length, $\ell_R(B) = \ell_R(B=0)/\sqrt{1+\mu^2 B^2}$ (here μ stands for carrier mobility). The edge

contribution to the overall resistance is linear in magnetic field [87] and can dominate in classically strong fields. This effect is not specific to Dirac fermions. Theoretically similar phenomena were considered in Refs. [114, 115, 199]. Experimentally, linear magnetoresistance due to recombination was studied in bilayer graphene in Ref. [88].

Electric current in a neutral graphene channel also becomes inhomogeneous in magnetic field (where all three modes in the "three mode approximation" discussed in Sect. 3 are coupled). However, unlike the situation in doped graphene, the current does not exhibit the Poiseuille-like flow (64) [125], see Fig. 20. One of the reasons for that is the boundary conditions: the Poiseuille flow is the solution of the hydrodynamic equations with the no-slip boundary conditions (which can be generalized to the Maxwell's boundary conditions with a relatively small slip length). The electric current in neutral graphene is not related to any solution of the Navier–Stokes equation and, moreover, there is no reason to assume that the current vanishes at the channel boundaries. In fact, for specular boundary conditions the opposite happens [125]: quasiparticle recombination leads to a minimum of the current density in the center of the channel, while the maximum value occurs at the boundaries. More general boundary conditions (see Sect. 3.2.7) require a numerical solution of the kinetic equation, which has not yet been carried out in this context.

An alternative geometry to study hydrodynamic flows is offered by the Corbino disk [139]. Here the electric current is inhomogeneous even in the simplest case of the Ohmic flow in the absence of magnetic field ($\boldsymbol{j} \propto (1/r)\boldsymbol{e}_r$, where $\boldsymbol{e}_r$ is the unit vector in the radial direction). Applying an external magnetic field that is orthogonal to the disk one can induce an azimuthal, non-dissipative Hall current (that is not compensated by the Hall voltage due to the absence of boundaries). The resulting inhomogeneous flows represent an excellent opportunity to study viscous effects [140]. The Corbino disk with specular boundaries was analyzed in Ref. [214]. Assuming small momentum relaxation, the authors of Ref. [214] concluded that the Hall angle (that can be determined by the ratio of the azimuthal and radial components of the current) is directly related to the ratio of the Hall and shear viscosities such that the resistive Hall angle approaches the viscous Hall angle. Anomalous thermoelectric response (i.e., violating the Matthiessen's rule, Wiedemann–Franz law, and Mott relation) exhibited by hydrodynamic flows in the absence of Galilean invariance was reported in Ref. [275].

Recently, the Corbino geometry was used to demonstrate the "superballistic conduction" both experimentally [54] and theoretically [276, 277]. Both theories focused on the boundary effects. Ref. [277] analyzed the radial electric current (in the absence of magnetic field). In the hydrodynamic regime, the interface between the lead (assumed to be a perfect conductor) and the Corbino disk is characterized by the finite Knudsen layer [138] with the boundary conductance that can exceed the Sharvin conductance [104]. Reference [276] came to similar conclusions arguing that if the number of conducting channels varies along the current flow (using either a wormhole or Corbino geometries as examples), the Landauer–Sharvin resistance is detached from the leads and is spread throughout the bulk of the system. If the length scale characterizing the spread is larger than ℓ_{ee} then the resistance is reduced leading to superballistic conductance.

More complicated flow patterns can be achieved by considering curved boundaries or adding artificial obstacles to engineer boundary conditions [97, 98]. In particular, on

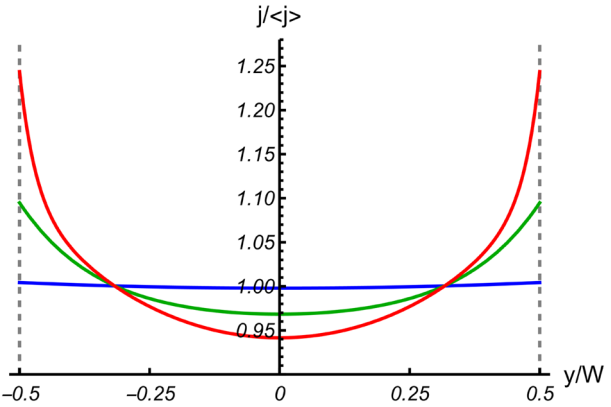

Fig. 20 Anti-Poiseuille flow in narrow channels in graphene in perpendicular magnetic field [125]. The curves represent the inhomogeneous current density in narrow channels of width $W = 0.1,\ 1,\ 5\,\mu$m (blue, green, and red curves, respectively). Calculations wee performed for typical parameter values $\tau_{\rm dis} \approx 0.8\,$THz [43], $\alpha_g \approx 0.2$ [43, 178], $\nu \approx 0.4\,{\rm m}^2/{\rm s}$ [50, 119], $B = 0.1\,$T, $T = 250\,$K (Reprinted with permission from Ref. [125]. Copyright (2021) by the American Physical Society)

the basis of numerical analysis it was shown [98] that additional barriers on the channel walls may lead to the effective "no-slip" boundary conditions that are commonly assumed in theoretical calculations.

5 Nonlinear phenomena in electronic hydrodynamics

Nonlinear hydrodynamic effects in electronic systems remain largely unexplored both theoretically and experimentally. Early numerical work [278] suggests that electron flows with the high enough Reynolds numbers (for samples of the size of $5\,\mu$m and macroscopic speeds $u \sim 10^5$ m/s [279], the authors of Ref. [278] estimate ${\rm Re} \sim 100$) may exhibit pre-turbulent phenomena such as vortex shedding.

A representative example of nonlinear hydrodynamic phenomena in graphene—hot spot relaxation—was considered in Ref. [121]. A hot spot is a particular non-equilibrium state of the system that is characterized by a locally elevated energy density. This state can be prepared with the help of a local probe or focused laser radiation [250, 251]. As expected [250, 251], the hot spot loses energy by emitting plasmon-like waves. At charge neutrality, these are in fact acoustic energy waves analogous to the long-wavelength oscillations in interacting systems of relativistic particles [sometimes called the "cosmic sound", see Eq. (48)]. However, a nonzero excess energy remains at the hot spot due to compensation between the thermodynamic pressure and the self-consistent (Vlasov) electric field. Dissipation tends to destroy the thus achieved quasi-equilibrium, but the resulting decay is characterized by a longer time scale as compared to the initial emission of plasmons. At the same time, the plasmons appear to be damped by viscous effects, see Sect. 3.3.3. The plasmon emission can also be expected in the in the high-frequency regime, where it has been linked to the Cherenkov effect [280–283].

The above quasi-equilibrium solution [121] may be viewed as an example of a soliton-like stationary nonlinear wave where charge and energy fluctuations (otherwise distinct at charge neutrality) are coupled by nonlinearity of the hydrodynamic theory. Away from charge neutrality, solitons were considered in the inviscid limit in Ref. [284] and more generally in Ref. [285]. In particular, the authors of Ref. [285] focused on hydrodynamic flows in graphene, where the decay of solitonic solutions was suggested as a possible experimental measure of electronic viscosity.

One of the most important consequences of nonlinearity of the hydrodynamic equations—turbulence [13]—is currently regarded as unlikely to occur in electronic systems, e.g., in graphene. In conventional fluids, turbulence can be reached when the Reynolds number characterizing the flow becomes large, $\mathrm{Re} \gtrsim 1000$ [13]. In contrast, typical Reynolds numbers characterizing existing experiments in graphene are rather small. Indeed, assuming one of the highest reported values of the drift velocity graphene, $u \sim 10^5$ m/s (based on the "saturation velocity measurements" [286]), the experimental estimate for the kinematic viscosity $\nu \sim 0.1\,\mathrm{m}^2/\mathrm{s}$ [27], and a typical sample size $L \sim 1\,\mu$m, one can estimate the Reynolds number as

$$\mathrm{Re} = \frac{uL}{\nu} \sim \frac{10^5 \frac{\mathrm{m}}{\mathrm{s}} \times 10^{-6}\mathrm{m}}{0.1 \frac{\mathrm{m}^2}{\mathrm{s}}} = 1.$$

At such values of the Reynolds number, one may hope to observe "pre-turbulent" phenomena, such as vortex shedding, as can be seen by solving the hydrodynamic equations numerically [278] (although at somewhat higher Re, see Fig. 21). For a possibility to achieve turbulence in electronic systems other than graphene, see Ref. [287].

Nonlinearity of the Navier–Stokes equation also leads to a number of known instabilities, arising in particular in systems with nontrivial boundary conditions [13]. One

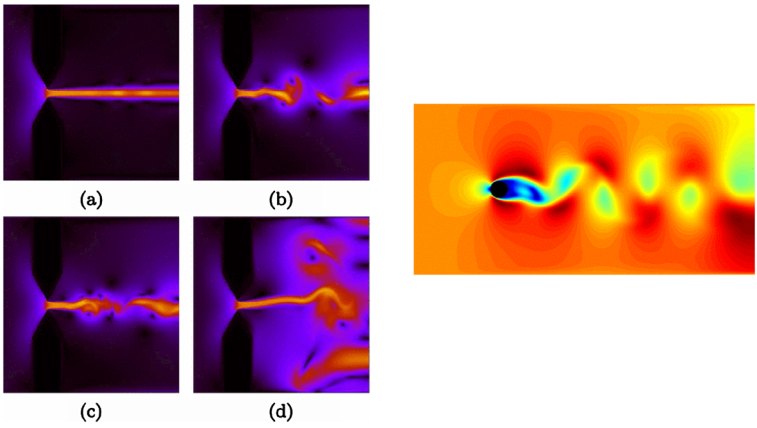

Fig. 21 Preturbulent hydrodynamic phenomena [278]. Left: microscale impurities in graphene can trigger coherent vorticity patterns that closely resemble classical 2D turbulence. The color represents the magnitude of the velocity. Calculations wee performed for $\mathrm{Re} = 25$. Right: Vortex shedding in graphene at $\mathrm{Re} = 100$ (Reprinted with permission from Ref. [278]. Copyright (2011) by the American Physical Society)

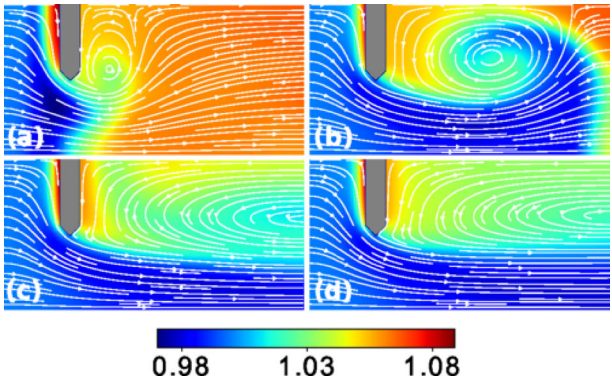

Fig. 22 Kelvin–Helmholtz instability in graphene [288]. The color represents density fluctuations relative to the initial density. The streamlines show the direction of the hydrodynamic velocity. The gray object is the stationary obstacle. The four images are respective snapshots of the fluid motion taken at different times. Calculations wee performed for Re = 53 (Reprinted with permission from Ref. [288]. Copyright (2017) by the American Physical Society)

of these instabilities, the Kelvin–Helmholz instability [290, 291], was studied numerically in Ref. [288], see Fig. 22. In conventional fluids this effect (actually visible in the atmosphere as a specific cloud pattern, the "fluctus") occurs in the case of velocity shear within a continuous fluid or at the interface between two fluids. In an electronic system this can be achieved by directing a charge flow through a macroscopic obstacle beyond which one observes vortex formation [288] that is reminiscent of the "whirlpools" that have been argued to be at the core of the nonlocal resistance experiments [27, 93–96]. Similarly, numerical simulations demonstrate the Rayleigh-Bénard instability [292, 293], see Ref. [289] and Fig. 23. Note that the simulations of Ref. [288] were performed using a lattice Boltzmann method for relativistic gases. For more recent work on that method see Ref. [294].

In addition to the "conventional" instabilities of the hydrodynamic equations, there is another instability that is predicted to occur in a ballistic field effect transistor [22] or, in other words, in a gated 2D electron systems. There are two key observations leading to the appearance of this instability. First, the carrier density in gated structures is determined by the same electric field (or voltage), see Eq. (53b), that represents the driving term in the Navier–Stokes equation (43a). In that case, the simplified Navier–Stokes equation (i.e., in the absence of magnetic field, neglecting Joule heating and weak disorder scattering) together with the continuity equation closely resemble the standard hydrodynamic equations for "shallow water" [13]. Second, one requires somewhat unusual (but experimentally feasible) boundary conditions: by connecting the source and drain of the device to a current source and the gate, while at the same time connecting the source to a voltage source, one arrives at the setup with a constant value of the voltage at the source together with the constant value of the current at the drain. In that case the wave velocities (shallow water waves in hydrodynamics or plasma waves in the heterostructure) describing propagation in the opposite directions are different leading to the instability with respect to plasmon generation. Known as the "Dyakonov–Shur" instability, this effect has attracted considerable attention in liter-

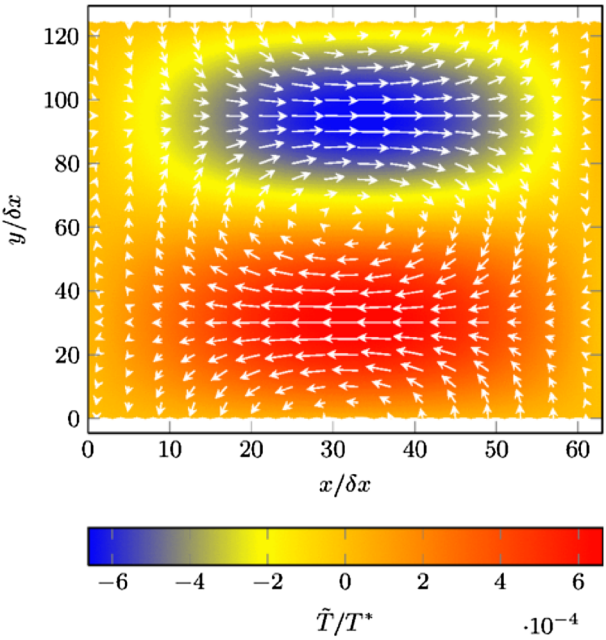

Fig. 23 Rayleigh–Bénard instability in graphene [289]. The color represents the temperature perturbation field with $T^* = 100$ K. The streamlines show the electron velocity. The image shows the formation of convection cells and the cosine-shaped temperature perturbation vanishing at the thermal contacts. (Reprinted with permission from Ref. [289]. Copyright (2015) by the American Physical Society)

ature, including that on hydrodynamic behavior in graphene [295, 296]; however, a definitive experimental observation of the effect is still lacking. For a detailed numerical analysis of a similar instability in GaAs MESFETs see Ref. [297]. An alternative suggestion for using viscous electrons as a source of terahertz radiation was proposed in Ref. [298]. Dyakonov–Shur instability in the Corbino geometry was discussed in Ref. [299].

Further nonlinear phenomena were discussed in Ref. [300] where three distinct hydrodynamic effects, namely the Bernoulli effect [301], Eckart streaming [302], and Rayleigh streaming [303], were suggested as possible experiments revealing nonlinear electron fluid dynamics, see Fig. 24. The suggested electronic analog of the Bernoulli effect yields a nonlinear term in the I–V characteristic ($V \propto I^2$) in the "Venturi geometry" (named after the Venturi tube, the standard device used for demonstrating the Bernoulli effect), which is essentially a finite-angle sector of the Corbino disk. The proposed effect is strongly dependent on sample geometry (e.g., it is expected to vanish in rectangular samples) and hence the boundary conditions. While the stationary Bernoulli effect is expected to occur in the ideal (inviscid) fluid, the dynamic nonlinear phenomena, such as the Eckart and Rayleigh streaming, are expected to occur in the presence of dissipation. Applying an oscillatory voltage to one of the sources while grounding the drain, the authors of Ref. [300] find a dc current (via the down-conversion). The two effects are distinguished by whether the dominant dissipation occurs in the bulk (Eckart streaming) or at the boundaries (Rayleigh streaming).

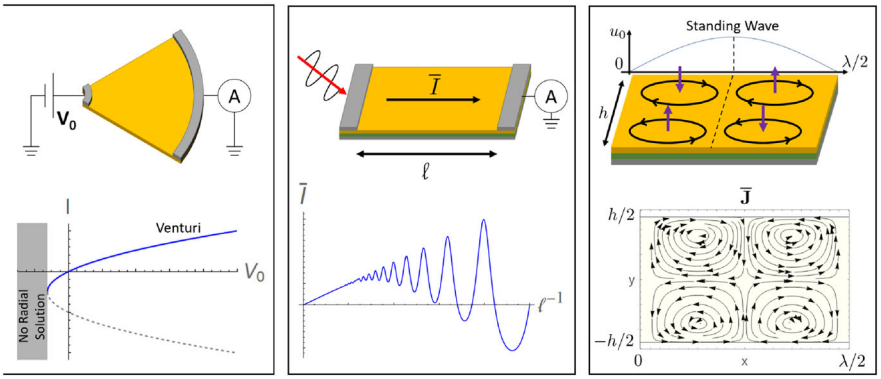

Fig. 24 Nonlinear hydrodynamic phenomena suggested in Ref. [300]. Left: the Venturi geometry and the expected nonlinear I–V characteristic with $I \sim \sqrt{V}$ (the gray dashed line represents and unstable solution, while the gray area corresponds to the parameter regime of a possible instability towards turbulence). Center: Eckart streaming and the rectification effect. Right: Rayleigh streaming. (Reprinted with permission from Ref. [300]. Copyright (2021) by the American Physical Society)

6 Theoretical conjectures of hydrodynamic behavior in strongly correlated systems

A (relatively) recent discovery of gauge-gravity duality (or AdS/CFT correspondence) [304–306] offers a new alternative theoretical tool to study strongly correlated systems by relating strongly coupled quantum field theories to gravity theories in one additional dimension. The best-known result of this approach is the conjectured lower bound for the shear viscosity to entropy density ratio [232] that has been found to be satisfied in quark-gluon plasma [307], cold atoms in the unitary limit [308], and intrinsic graphene [180]. The same physics can also be expressed in terms of the diffusivity bound [309]. Such bounds reflect not only the interaction strength, but also the symmetry properties of the system. In particular, in anisotropic systems the proposed bounds should be modified [183, 310].

In the condensed matter context, the duality has also been applied to the by now perennial issue of the linear resistivity [311] in "strange metals" [312, 313] (cuprates [314, 315], iron-based superconductors [316–319], twisted bilayer graphene at magic angles [320, 321], etc). The main premise of this approach is that excitations in strongly correlated systems are predominantly of the "collective" nature unlike the quasiparticles in conventional metals [306]. In that case, the system is described by "hydrodynamic-like" currents, with their relation to the external fields provided by the standard linear response theory. This way one can suggest universal bounds on the diffusion coefficient and conductivity (related by the Einstein relation) of a strange metal, as well as their scaling with temperature [309, 310]. The concept of diffusion appears through a particular collective mode (the so-called quasinormal mode [322]). Such modes essentially replace quasiparticles in the qualitative interpretation of the resulting theory [306]. Linear response transport properties can then be obtained by means of either solving the hydrodynamic equations or using the memory matrix formalism [323]. The latter has the advantage of being independent of the concept of quasiparticles and extending beyond the hydrodynamic regime.

The holographic duality can also be used in the opposite direction, where solutions of hydrodynamic theories can provide insight into physical properties of gravitational objects [324].

While they might appear too abstract, the holographic methods can be put to test by studying the typical condensed matter experiment: optical pump-probe spectroscopy [325]. The idea is to test one of the characteristic predictions of the bulk (gravity) side of the duality—instantaneous thermalization [326]. This feature (impossible in the usual semiclassical description of transport) is the natural consequence of causality and is related to the "eigenstate thermalization hypothesis" [327, 328]. As a result, measuring the optical conductivity in a strange metal excited by a short, intense laser pulse that does not contain a zero-frequency component one should obtain the exact same results as in the same system at equilibrium (characterized by the final temperature) at all times after the pulse.

The linear resistivity has also been interpreted as a signature of "Planckian dissipation" [329, 330] (which is also related to the above proposed bounds). The idea comes from the fact that the observed optical conductivity in strange metals often allows for a good fit with the standard Drude expression [311, 315, 331, 332] which is described by a timescale typically referred to as the "transport scattering time", $\tau_{\rm tr}$, [10]. The linear temperature dependence of the resistivity thus translates into the $\tau_{\rm tr}$ being inverse proportional to temperature or, in other words, proportional to the "Planckian" timescale

$$\tau_{\rm tr} \propto \tau_P = \frac{\hbar}{k_B T}, \tag{65}$$

where the Planck's and Boltzmann's constants ($\hbar$ and k_B) are restored for clarity. While completely natural in neutral graphene, see Eqs. (30), where the temperature dependence (65) follows already from dimensional analysis (in graphene at charge neutrality, T is the only energy scale), application of the concept of the scattering time to strongly correlated systems is more problematic. One possibility is that one can trace the decay of correlation functions (which can be characterized through a "transport" time scale) to the decay of local operators, as suggested in Ref. [330].

The hypothesis of the near-hydrodynamic behavior in strange metals (at least, at low temperatures where the measured optical conductivity has a Drude form) might sound attractive, but it certainly does not solve all the problems [329]. At higher temperatures, there appears the state of a "bad metal", where the optical conductivity is no longer of the Drude form [333], while the temperature dependence of the resistivity is still linear. Quantum Monte Carlo simulations [334] suggest that this state is accompanied by hints of spin-stripe correlations [335]. While there might be a way to include that physics into holographic modeling [336], the role of electron–phonon coupling, quantum criticality, and their relation to the seemingly "universal" linear resistivity across several distinct families of materials remains to be understood.

The above ideas on applying holographic methods to strange metals (in particular in cuprates) remain controversial. For a recent critique of this approach, see Ref. [337].

A detailed discussion of relativistic hydrodynamics on the basis of the AdS/CFT correspondence was offered in Ref. [338]. In the 2D wire (channel) geometry with

no-slip boundary conditions, this theory yields the Poiseuille behavior (see Sect. 2) for all velocities up to the ultrarelativistic limit $u \to v_g$. In the latter case, however, the differential resistance of the channel vanishes as a consequence of the kinematics of special relativity. The theory of Ref. [338] also offers further insights into the importance of the shear viscosity to entropy density ratio, η/s. First, the channel resistance strongly scales with η/s, such that "holographic strongly coupled fluids" (either at or near the proposed bound $\eta/s \simeq 1/(4\pi)$ [232]) are characterized by smaller resistance in comparison to conventional fluids. Second, the boundary relaxation time (i.e., the timescale describing the rate of the loss of momentum at the channel boundaries with no-slip boundary conditions) is inverse proportional to η/s.

7 Open questions and perspectives

The scope of this review was mostly limited to observable effects that can be interpreted as evidence of electronic hydrodynamics in graphene and other 2D materials as well as theoretical work exploring hydrodynamic phenomena in electronic systems. Several important topics were purposefully left out, most notably the hydrodynamic behavior of non-electronic excitations in solids, topological hydrodynamics, and generalized hydrodynamics in 1D systems.

The initial argument for electronic hydrodynamics requiring the electron–electron interaction to be the dominant scattering mechanism implies the existence of scale separation between electronic thermalization and energy relaxation due to, e.g., electron–phonon interaction. The latter typically assumes that the phonons are in thermal equilibrium. However, the current-carrying distribution of electrons is generally non-equilibrium and hence electron–phonon coupling can drive the phonons out of equilibrium as well [339]. The resulting phenomenon of phonon drag is well studied [340, 341] and in particular allows for a hydrodynamic description [342]. Recently, evidence of the coupled electron–phonon fluid was reported in the Dirac semimetal $PtSn_4$ [343] (for the theory see Ref. [344]), the material characterized by very low resistivity as well as showing a pronounced phonon drag peak [156] at low temperatures. Moreover, it was argued [345] that near-hydrodynamic behavior of electronic transport in the delafossite metals $PdCoO_2$ and $PtCoO_2$ [29, 346] should be understood in the context of phonon drag.

Another aspect of the strong coupling between the electronic system and the crystal lattice is the interplay between electronic viscosity and elasticity of the crystal [211, 212, 215, 347, 348]. Moreover, static deformations in graphene are known to lead to the appearance of giant pseudomagnetic fields [349]. From a general perspective, elasticity and hydrodynamics belong to a broader class of tensor-field theories that also includes gravitation theories and the theory of critical phenomena in spaces with nontrivial metrics [350].

Observations of viscous hydrodynamics in electronic transport raised the question of whether other excitations in solids might behave hydrodynamically as well. In particular, the classic proposal for the hydrodynamic behavior of spin waves [19] recently came under intense scrutiny both experimentally [351] and theoretically [352, 353]. Emergent hydrodynamics in a strongly interacting dipolar spin ensemble (consist-

ing of substitutional nitrogen defects—P1 centers—and nitrogen-vacancy centers in diamonds) was studied experimentally in Ref. [354].

Generally speaking, hydrodynamic flows represent a macroscopic, long wavelength motion governed by global conservation laws [1]. In conventional fluids, these include the particle number, energy, and momentum conservation allowing for a statistical description of the system based on traditional Gibbs approach [16]. In two-(and three-)dimensional electronic systems energy and momentum are conserved only approximately, which limits the applicability of the hydrodynamic approach to a relatively narrow temperature interval [23, 24, 176] as well as leads to unconventional behavior [85, 87, 114]. In one spatial dimension, in particular in the context of integrable (exactly solvable) models, the situation is different: here the system is characterized by a large number of integrals of motion leading to the concept of *generalized* Gibbs ensembles [355, 356]. Applying the hydrodynamic approach to the generalized Gibbs statistics yields generalized hydrodynamics offering new possibilities in describing quantum transport in systems with predominantly ballistic behavior (due to the large number of conservation laws). This approach was introduced in the context of integrable field theories [357] and quantum spin chains [358] and was successfully applied to a number of other integrable systems [359]. The resulting framework was used to describe one-dimensional cold atomic gases at large wavelengths [360] and has been observed experimentally [361]. Generalized hydrodynamics in nonintegrable systems was studied in Ref. [362].

Another topic outside of the scope of this review is topological hydrodynamics, see Ref. [363] and references therein. Recently, an optical topological invariant (measurable via the evanescent magneto-optic Kerr effect [364]) was proposed to describe properties of the viscous Hall fluid [365] suggesting that graphene with the "repulsive" Hall viscosity (i.e., $\omega_c \nu_H > 0$) may be used to create a topological electromagnetic phase of matter. Especially interesting in this context is the interplay of topological band structure and electron–electron interactions (responsible for establishing the local equilibrium underlying the usual hydrodynamic theory). A related issue is quantum hydrodynamics of vorticity [366] describing vortex–antivortex dynamics in 2D bosonic lattices pertaining to the superfluid–insulator transition.

While some experimental work on hydrodynamics in topological materials was addressed in Sect. 2.5.2, the theoretical discussion of Sect. 3 focused on the well-studied cases of the 2D Dirac and Fermi liquids. In contrast, a hydrodynamic theory of topological materials (including Weyl semimetals [59, 60] and conducting surface states of topological insulators) has not been hammered out yet. For recent literature on this subject see Refs. [66, 367–371]. The effects of band topology on the shear viscosity were considered in Ref. [372].

Despite the impressive amount of recent work on the subject, electronic hydrodynamics remains a young field with many unanswered questions. So far, the main focus of the community was on Fermi-liquid-type materials (including doped graphene), where the hydrodynamic equations are basically equivalent to the standard Navier–Stokes equation and the velocity field completely determines the electric current. Even in this simplest setting, the question of boundary conditions remains largely unresolved, especially in view of the experiment of Ref. [53]. Furthermore, practical applications of hydrodynamic equations require reliable tools for their numerical

solution. Although there exists a massive amount of literature devoted to solution of differential equations (as well as commercial and open source software packages dealing with their numerical solutions), equations of electronic hydrodynamics have to be solved together with the equations describing the electrostatic environment of the system, the electronic circuit into which the system is integrated, and in the case of spintronics applications—the magnetic environment. Combining all these aspects of the problem with the realistic boundary conditions and specific symmetries represents a formidable computational problem that is rather difficult to solve using the available "canned" solvers [373, 374].

Transport properties addressed with the hydrodynamic approach so far remain at the semiclassical "Drude" level (which is not surprising given that the hydrodynamic equations, see Sect. 3.2.6, were derived from the semiclassical Boltzmann equation, see Sect. 3. In contrast, the traditional transport theory considers also "higher order" processes leading to the so-called "quantum corrections" [9, 12, 375]. While typically discussed using field-theoretic methods, these results can also be obtained within the kinetic approach (for the corresponding "quantum kinetic equation" see Ref. [12]). It remains to be seen, whether this physics can be included in a macroscopic, hydrodynamic-type description. Moreover, it is unclear whether one can establish any relation between the well-known hydrodynamic fluctuations [13] and mesoscopic fluctuations in conventional diffusive conductors [376–378].

One of the most intriguing promises of the hydrodynamic approach is its supposed ability to describe properties of more complicated systems, including the "strange metals" [312]. This direction of research is still in its infancy. Many novel materials (including van der Waals heterostructures [320, 379], conducting surface states of topological insulators, and Weyl semimetals) are characterized by strong spin–orbit coupling. Up until now, a coherent kinetic theory for electrons with spin–orbit interaction has not been established, see Refs. [177, 380–382]. An advance in this direction could provide a substantial contribution to the application-oriented field of spintronics [383, 384], which has been under active development in the last 2 decades.

The conjecture of Planckian dissipation does not explain why does the observed resistivity remains linear (i.e., does not vanish faster) in different materials where different scattering mechanisms are presumed to be relevant in different temperature regimes [311]. This could indicate an existence of a universal principle limiting the decay rate of the longest lived modes in strongly correlated systems (similarly to the phase space limitations on the quasiparticle properties in Fermi liquids). Such a principle has not been established yet.

Finally, the issues raised in the course of the rapid development of electronic hydrodynamics are of fundamental importance for the physics of novel electronic systems necessary for the future development of functional materials. Future advances in this field will have far-reaching implications beyond the scope of particular systems considered in this review. They will substantially improve our understanding of interrelation of macroscopic transport properties (of charge, spin, and heat) and microscopic structure (symmetry properties, band structure, electronic correlations) of materials allowing for material engineering and functionalization.

Acknowledgements The author is grateful to I. Aleiner, P. Alekseev, U. Briskot, I. Burmistrov, A. Dmitriev, I. Gornyi, V. Kachorovskii, E. Kiselev, A. Mirlin, J. Schmalian, M. Schütt, A. Shnirman, and M. Titov for fruitful discussions.

Funding Open Access funding enabled and organized by Projekt DEAL. This work was supported by the German Research Foundation DFG Project NA 1114/5-1, by the German Research Foundation DFG within FLAG-ERA Joint Transnational Call (Project GRANSPORT), by the European Commission under the EU Horizon 2020 MSCA-RISE-2019 program (Project 873028 HYDROTRONICS).

Data Availability Statement There are no data associated with the paper

Declarations

Conflict of interest The author has no relevant financial or non-financial interests to disclose.

References

1. P.M. Chaikin, T.C. Lubensky, *Principles of condensed matter physics* (Cambridge University Press, Cambridge, 1995). https://doi.org/10.1017/CBO9780511813467
2. N. Bloembergen, Physica **15**, 386 (1949). https://doi.org/10.1016/0031-8914(49)90114-7
3. L.P. Kadanoff, P.C. Martin, Ann. Phys. (NY) **24**, 419 (1963). https://doi.org/10.1016/0003-4916(63)90078-2
4. A. Tucciarone, J.M. Hastings, L.M. Corliss, Phys. Rev. B **8**, 1103 (1973). https://doi.org/10.1103/PhysRevB.8.1103
5. B.N. Narozhny, Phys. Rev. B **54**, 3311 (1996). https://doi.org/10.1103/PhysRevB.54.3311
6. B.N. Narozhny, A.J. Millis, N. Andrei, Phys. Rev. B **58**, R2921 (1998). https://doi.org/10.1103/PhysRevB.58.R2921
7. A. Rosch, N. Andrei, Phys. Rev. Lett. **85**, 1092 (2000). https://doi.org/10.1103/PhysRevLett.85.1092
8. J. Sirker, R.G. Pereira, I. Affleck, Phys. Rev. Lett. **103**, 216602 (2009). https://doi.org/10.1103/PhysRevLett.103.216602
9. B.L. Altshuler, A.G. Aronov, in *Electron–electron interactions in disordered systems*, ed. by A.L. Efros, M. Pollak (North-Holland, Amsterdam, 1985). https://doi.org/10.1016/B978-0-444-86916-6.50007-7
10. J.M. Ziman, *Principles of the theory of solids* (Cambridge University Press, Cambridge, 1965). https://doi.org/10.1017/CBO9781139644075
11. C. Beenakker, H. van Houten, in *Semiconductor Heterostructures and Nanostructures*, *Solid State Physics*, vol. 44, ed. by H. Ehrenreich, D. Turnbull (Academic Press, 1991), pp. 1–228. https://doi.org/10.1016/S0081-1947(08)60091-0
12. G. Zala, B.N. Narozhny, I.L. Aleiner, Phys. Rev. B **64**, 214204 (2001). https://doi.org/10.1103/PhysRevB.64.214204
13. L.D. Landau, E.M. Lifshitz, *Fluid Mechanics* (Pergamon Press, London, 1987). https://doi.org/10.1016/C2013-0-03799-1
14. H. Lamb, *Hydrodynamics* (Dover, New York, 1945)
15. D. Vollhardt, P. Wölfle, The superfluid phases of helium 3 (Taylor and Francis. London (1990). https://doi.org/10.1201/b12808

16. E.M. Lifshitz, L.P. Pitaevskii, Physical Kinetics (Pergamon Press. London (1981). https://doi.org/10.1016/C2009-0-25523-1
17. R.N. Gurzhi, Soviet Physics Uspekhi **11**(2), 255 (1968). https://doi.org/10.1070/PU1968v011n02ABEH003815. [Usp. Fiz. Nauk 94, 689 (1968)]
18. Y. Machida, N. Matsumoto, T. Isono, K. Behnia, Science **367**(6475), 309 (2020). https://doi.org/10.1126/science.aaz8043
19. B.I. Halperin, P.C. Hohenberg, Phys. Rev. **188**, 898 (1969). https://doi.org/10.1103/PhysRev.188.898
20. R.N. Gurzhi, Zh. Eksp. Teor. Fiz. **44**, 771 (1963). [Sov. Phys. JETP **17**, 521 (1963)]
21. R.N. Gurzhi, Zh. Eksp. Teor. Fiz. **47**, 1415 (1965). [Sov. Phys. JETP **20**, 953 (1965)]
22. M. Dyakonov, M. Shur, Phys. Rev. Lett. **71**, 2465 (1993). https://doi.org/10.1103/PhysRevLett.71.2465
23. B.N. Narozhny, I.V. Gornyi, A.D. Mirlin, J. Schmalian, Annalen der Physik **529**(11), 1700043 (2017). https://doi.org/10.1002/andp.201700043
24. A. Lucas, K.C. Fong, J. Phys, Condens. Matter **30**(5), 053001 (2018). https://doi.org/10.1088/1361-648x/aaa274
25. M. Polini, A.K. Geim, Phys. Today **73**(6), 28 (2020). https://doi.org/10.1063/PT.3.4497
26. A.A. Abrikosov, I.M. Khalatnikov, Rep. Prog. Phys. **22**(1), 329 (1959). https://doi.org/10.1088/0034-4885/22/1/310
27. D.A. Bandurin, I. Torre, R. Krishna Kumar, M. Ben Shalom, A. Tomadin, A. Principi, G.H. Auton, E. Khestanova, K.S. Novoselov, I.V. Grigorieva, L.A. Ponomarenko, A.K. Geim, M. Polini, Science **351**, 1055 (2016). https://doi.org/10.1126/science.aad0201
28. J. Crossno, J.K. Shi, K. Wang, X. Liu, A. Harzheim, A. Lucas, S. Sachdev, P. Kim, T. Taniguchi, K. Watanabe, T.A. Ohki, K.C. Fong, Science **351**(6277), 1058 (2016). https://doi.org/10.1126/science.aad0343
29. P.J.W. Moll, P. Kushwaha, N. Nandi, B. Schmidt, A.P. Mackenzie, Science **351**(6277), 1061 (2016). https://doi.org/10.1126/science.aac8385
30. B.A. Braem, F.M.D. Pellegrino, A. Principi, M. Röösli, C. Gold, S. Hennel, J.V. Koski, M. Berl, W. Dietsche, W. Wegscheider, M. Polini, T. Ihn, K. Ensslin, Phys. Rev. B **98**, 241304(R) (2018). https://doi.org/10.1103/PhysRevB.98.241304
31. A. Jaoui, B. Fauqué, C.W. Rischau, A. Subedi, C. Fu, J. Gooth, N. Kumar, V. Süß, D.L. Maslov, C. Felser, K. Behnia, NPJ Quantum Mater. **3**, 64 (2018). https://doi.org/10.1038/s41535-018-0136-x
32. G.M. Gusev, A.S. Jaroshevich, A.D. Levin, Z.D. Kvon, A.K. Bakarov, Sci. Rep. **10**(1), 7860 (2020). https://doi.org/10.1038/s41598-020-64807-6
33. G. Varnavides, A.S. Jermyn, P. Anikeeva, C. Felser, P. Narang, Nat. Commun. **11**(1), 4710 (2020). https://doi.org/10.1038/s41467-020-18553-y
34. U. Vool, A. Hamo, G. Varnavides, Y. Wang, T.X. Zhou, N. Kumar, Y. Dovzhenko, Z. Qiu, C.A.C. Garcia, A.T. Pierce, J. Gooth, P. Anikeeva, C. Felser, P. Narang, A. Yacoby, Nat. Phys. (2021). https://doi.org/10.1038/s41567-021-01341-w
35. A. Jaoui, B. Fauqué, K. Behnia, Nat. Commun. **12**(1), 195 (2021). https://doi.org/10.1038/s41467-020-20420-9
36. A. Gupta, J.J. Heremans, G. Kataria, M. Chandra, S. Fallahi, G.C. Gardner, M.J. Manfra, Phys. Rev. Lett. **126**, 076803 (2021). https://doi.org/10.1103/PhysRevLett.126.076803
37. S.S. Pershoguba, A.F. Young, L.I. Glazman, Phys. Rev. B **102**, 125404 (2020). https://doi.org/10.1103/PhysRevB.102.125404
38. D.Y.H. Ho, I. Yudhistira, N. Chakraborty, S. Adam, Phys. Rev. B **97**, 121404(R) (2018). https://doi.org/10.1103/PhysRevB.97.121404
39. R. Krishna Kumar, D.A. Bandurin, F.M.D. Pellegrino, Y. Cao, A. Principi, H. Guo, G.H. Auton, M. Ben Shalom, L.A. Ponomarenko, G. Falkovich, K. Watanabe, T. Taniguchi, I.V. Grigorieva, L.S. Levitov, M. Polini, A.K. Geim, Nat. Phys. **13**(12), 1182 (2017). https://doi.org/10.1038/nphys4240
40. F. Ghahari, H.Y. Xie, T. Taniguchi, K. Watanabe, M.S. Foster, P. Kim, Phys. Rev. Lett. **116**, 136802 (2016). https://doi.org/10.1103/PhysRevLett.116.136802
41. D.A. Bandurin, A.V. Shytov, L.S. Levitov, R. Krishna Kumar, A.I. Berdyugin, M. Ben Shalom, I.V. Grigorieva, A.K. Geim, G. Falkovich, Nat. Commun. **9**(1), 4533 (2018). https://doi.org/10.1038/s41467-018-07004-4

42. A.I. Berdyugin, S.G. Xu, F.M.D. Pellegrino, R. Krishna Kumar, A. Principi, I. Torre, M.B. Shalom, T. Taniguchi, K. Watanabe, I.V. Grigorieva, M. Polini, A.K. Geim, D.A. Bandurin, Science **364**(6436), 162 (2019). https://doi.org/10.1126/science.aau0685
43. P. Gallagher, C.S. Yang, T. Lyu, F. Tian, R. Kou, H. Zhang, K. Watanabe, T. Taniguchi, F. Wang, Science **364**(6436), 158 (2019). https://doi.org/10.1126/science.aat8687
44. A. Jenkins, S. Baumann, H. Zhou, S.A. Meynell, D. Yang, T.T. K. Watanabe, A. Lucas, A.F. Young, A.C. Bleszynski Jayich (2020). https://doi.org/10.48550/arXiv.2002.05065
45. Z.J. Krebs, W.A. Behn, S. Li, K.J. Smith, K. Watanabe, T. Taniguchi, A. Levchenko, V.W. Brar (2021). https://doi.org/10.48550/arXiv.2106.07212
46. A. Finkler, Y. Segev, Y. Myasoedov, M.L. Rappaport, L. Ne'eman, D. Vasyukov, E. Zeldov, M.E. Huber, J. Martin, A. Yacoby, Nano Lett. **10**(3), 1046 (2010). https://doi.org/10.1021/nl100009r
47. D. Halbertal, J. Cuppens, M. Ben Shalom, L. Embon, N. Shadmi, Y. Anahory, H.R. Naren, J. Sarkar, A. Uri, Y. Ronen, Y. Myasoedov, L.S. Levitov, E. Joselevich, A.K. Geim, E. Zeldov, Nature **539**(7629), 407 (2016). https://doi.org/10.1038/nature19843
48. A. Marguerite, J. Birkbeck, A. Aharon-Steinberg, D. Halbertal, K. Bagani, I. Marcus, Y. Myasoedov, A.K. Geim, D.J. Perello, E. Zeldov, Nature **575**(7784), 628 (2019). https://doi.org/10.1038/s41586-019-1704-3
49. A. Uri, Y. Kim, K. Bagani, C.K. Lewandowski, S. Grover, N. Auerbach, E.O. Lachman, Y. Myasoedov, T. Taniguchi, K. Watanabe, J. Smet, E. Zeldov, Nat. Phys. **16**(2), 164 (2020). https://doi.org/10.1038/s41567-019-0713-3
50. M.J.H. Ku, T.X. Zhou, Q. Li, Y.J. Shin, J.K. Shi, C. Burch, L.E. Anderson, A.T. Pierce, Y. Xie, A. Hamo, U. Vool, H. Zhang, F. Casola, T. Taniguchi, K. Watanabe, M.M. Fogler, P. Kim, A. Yacoby, R.L. Walsworth, Nature **583**, 537 (2020). https://doi.org/10.1038/s41586-020-2507-2
51. J.A. Sulpizio, L. Ella, A. Rozen, J. Birkbeck, D.J. Perello, D. Dutta, M. Ben-Shalom, T. Taniguchi, K. Watanabe, T. Holder, R. Queiroz, A. Stern, T. Scaffidi, A.K. Geim, S. Ilani, Nature **576**, 75 (2019). https://doi.org/10.1038/s41586-019-1788-9
52. L. Ella, A. Rozen, J. Birkbeck, M. Ben-Shalom, D. Perello, J. Zultak, T. Taniguchi, K. Watanabe, A.K. Geim, S. Ilani, J.A. Sulpizio, Nat. Nanotechnol. **14**, 480 (2019). https://doi.org/10.1038/s41565-019-0398-x
53. A. Aharon-Steinberg, A. Marguerite, D.J. Perello, K. Bagani, T. Holder, Y. Myasoedov, L.S. Levitov, A.K. Geim, E. Zeldov, Nature **593**, 528 (2021). https://doi.org/10.1038/s41586-021-03501-7
54. C. Kumar, J. Birkbeck, J.A. Sulpizio, D.J. Perello, T. Taniguchi, K. Watanabe, O. Reuven, T. Scaffidi, A. Stern, A.K. Geim, S. Ilani (2021). https://doi.org/10.48550/arXiv.2111.06412
55. G.M. Gusev, A.D. Levin, E.V. Levinson, A.K. Bakarov, Phys. Rev. B **98**, 161303(R) (2018). https://doi.org/10.1103/PhysRevB.98.161303
56. O.E. Raichev, G.M. Gusev, A.D. Levin, A.K. Bakarov, Phys. Rev. B **101**, 235314 (2020). https://doi.org/10.1103/PhysRevB.101.235314
57. G.M. Gusev, A.S. Jaroshevich, A.D. Levin, Z.D. Kvon, A.K. Bakarov, Phys. Rev. B **103**, 075303 (2021). https://doi.org/10.1103/PhysRevB.103.075303
58. M.J.M. de Jong, L.W. Molenkamp, Phys. Rev. B **51**, 13389 (1995). https://doi.org/10.1103/PhysRevB.51.13389
59. A. Lucas, R.A. Davison, S. Sachdev, Proc. Natl. Acad. Sci. **113**(34), 9463 (2016). https://doi.org/10.1073/pnas.1608881113
60. E.V. Gorbar, V.A. Miransky, I.A. Shovkovy, P.O. Sukhachov, Phys. Rev. B **97**, 205119 (2018). https://doi.org/10.1103/PhysRevB.97.205119
61. J.S. Bell, R. Jackiw, Nuovo Cimento A **60**, 47 (1969). https://doi.org/10.1007/BF02823296
62. S.L. Adler, Phys. Rev. **177**, 2426 (1969). https://doi.org/10.1103/PhysRev.177.2426
63. R. Jackiw, Int. J. Mod. Phys. A **25**(04), 659 (2010). https://doi.org/10.1142/S0217751X10048391
64. C. Felser, B. Yan, Nat. Mater. **15**(11), 1149 (2016). https://doi.org/10.1038/nmat4741
65. M. Hirschberger, S. Kushwaha, Z. Wang, Q. Gibson, S. Liang, C.A. Belvin, B.A. Bernevig, R.J. Cava, N.P. Ong, Nat. Mater. **15**(11), 1161 (2016). https://doi.org/10.1038/nmat4684
66. D.T. Son, B.Z. Spivak, Phys. Rev. B **88**, 104412 (2013). https://doi.org/10.1103/PhysRevB.88.104412
67. F. Arnold, C. Shekhar, S.C. Wu, Y. Sun, R.D. dos Reis, N. Kumar, M. Naumann, M.O. Ajeesh, M. Schmidt, A.G. Grushin, J.H. Bardarson, M. Baenitz, D. Sokolov, H. Borrmann, M. Nicklas, C. Felser, E. Hassinger, B. Yan, Nat. Commun. **7**(1), 11615 (2016). https://doi.org/10.1038/ncomms11615
68. M. Knudsen, Annalen der Physik **333**(1), 75 (1909). https://doi.org/10.1002/andp.19093330106. [Ann. Phys. (Leipzig) 28, 75 (1909)]

69. L.J. van der Pauw, Philips Tech. Rev. **20**, 223 (1958)
70. D.A. Abanin, S.V. Morozov, L.A. Ponomarenko, R.V. Gorbachev, A.S. Mayorov, M.I. Katsnelson, K. Watanabe, T. Taniguchi, K.S. Novoselov, L.S. Levitov, A.K. Geim, Science **332**, 328 (2011). https://doi.org/10.1126/science.1199595
71. P. Drude, Annalen der Physik **306**(1), 566 (1900). https://doi.org/10.1002/andp.19003060312. [Ann. Phys. (Leipzig) 1, 566 (1900)]
72. W.J. Skocpol, P.M. Mankiewich, R.E. Howard, L.D. Jackel, D.M. Tennant, A.D. Stone, Phys. Rev. Lett. **58**, 2347 (1987). https://doi.org/10.1103/PhysRevLett.58.2347
73. H. van Houten, C.W.J. Beenakker, J.G. Williamson, M.E.I. Broekaart, P.H.M. van Loosdrecht, B.J. van Wees, J.E. Mooij, C.T. Foxon, J.J. Harris, Phys. Rev. B **39**, 8556 (1989). https://doi.org/10.1103/PhysRevB.39.8556
74. A.K. Geim, P.C. Main, P.H. Beton, P. Steda, L. Eaves, C.D.W. Wilkinson, S.P. Beaumont, Phys. Rev. Lett. **67**, 3014 (1991). https://doi.org/10.1103/PhysRevLett.67.3014
75. K.L. Shepard, M.L. Roukes, B.P. van der Gaag, Phys. Rev. Lett. **68**, 2660 (1992). https://doi.org/10.1103/PhysRevLett.68.2660
76. Y. Hirayama, A.D. Wieck, T. Bever, K. von Klitzing, K. Ploog, Phys. Rev. B **46**, 4035 (1992). https://doi.org/10.1103/PhysRevB.46.4035
77. G. Mihajlović, J.E. Pearson, M.A. Garcia, S.D. Bader, A. Hoffmann, Phys. Rev. Lett. **103**, 166601 (2009). https://doi.org/10.1103/PhysRevLett.103.166601
78. R.V. Gorbachev, J.C.W. Song, G.L. Yu, A.V. Kretinin, F. Withers, Y. Cao, A. Mishchenko, I.V. Grigorieva, K.S. Novoselov, L.S. Levitov, A.K. Geim, Science **346**(6208), 448 (2014). https://doi.org/10.1126/science.1254966
79. P.L. McEuen, A. Szafer, C.A. Richter, B.W. Alphenaar, J.K. Jain, A.D. Stone, R.G. Wheeler, R.N. Sacks, Phys. Rev. Lett. **64**, 2062 (1990). https://doi.org/10.1103/PhysRevLett.64.2062
80. J.K. Wang, V.J. Goldman, Phys. Rev. B **45**, 13479 (1992). https://doi.org/10.1103/PhysRevB.45.13479
81. A. Roth, C. Brune, H. Buhmann, L.W. Molenkamp, J. Maciejko, X.L. Qi, S.C. Zhang, Science **325**(5938), 294 (2009). https://doi.org/10.1126/science.1174736
82. X.P. Zhang, C. Huang, M.A. Cazalilla, 2D Mater. **4**(2), 024007 (2017). https://doi.org/10.1088/2053-1583/aa5e9b
83. K. Komatsu, Y. Morita, E. Watanabe, D. Tsuya, K. Watanabe, T. Taniguchi, S. Moriyama, Sci. Adv. **4**(5), eaaq0194 (2018). https://doi.org/10.1126/sciadv.aaq0194
84. F. Chiappini, S. Wiedmann, M. Titov, A.K. Geim, R.V. Gorbachev, E. Khestanova, A. Mishchenko, K.S. Novoselov, J.C. Maan, U. Zeitler, Phys. Rev. B **94**, 085302 (2016). https://doi.org/10.1103/PhysRevB.94.085302
85. S. Danz, M. Titov, B.N. Narozhny, Phys. Rev. B **102**, 081114(R) (2020). https://doi.org/10.1103/PhysRevB.102.081114
86. M. Titov, R.V. Gorbachev, B.N. Narozhny, T. Tudorovskiy, M. Schütt, P.M. Ostrovsky, I.V. Gornyi, A.D. Mirlin, M.I. Katsnelson, K.S. Novoselov, A.K. Geim, L.A. Ponomarenko, Phys. Rev. Lett. **111**, 166601 (2013). https://doi.org/10.1103/PhysRevLett.111.166601
87. P.S. Alekseev, A.P. Dmitriev, I.V. Gornyi, V.Y. Kachorovskii, B.N. Narozhny, M. Schütt, M. Titov, Phys. Rev. Lett. **114**, 156601 (2015). https://doi.org/10.1103/PhysRevLett.114.156601
88. G.Y. Vasileva, D. Smirnov, Y.L. Ivanov, Y.B. Vasilyev, P.S. Alekseev, A.P. Dmitriev, I.V. Gornyi, V.Y. Kachorovskii, M. Titov, B.N. Narozhny, R.J. Haug, Phys. Rev. B **93**, 195430 (2016). https://doi.org/10.1103/PhysRevB.93.195430
89. M.S. Foster, I.L. Aleiner, Phys. Rev. B **79**, 085415 (2009). https://doi.org/10.1103/PhysRevB.79.085415
90. C.L. Navier, *in Mémoires de l'Académie des sciences de l'Institut de France - Année 1823* (Gauthier-Villars, Paris, 1827), pp. 389–440
91. G.G. Stokes, Trans. Camb. Philos. Soc. **8**, 287 (1845)
92. G.G. Stokes, Trans. Camb. Philos. Soc. **9**, 8 (1851)
93. S. Danz, B.N. Narozhny, 2D Materials **7**(3), 035001 (2020). https://doi.org/10.1088/2053-1583/ab7bfa
94. I. Torre, A. Tomadin, A.K. Geim, M. Polini, Phys. Rev. B **92**, 165433 (2015). https://doi.org/10.1103/PhysRevB.92.165433
95. F.M.D. Pellegrino, I. Torre, A.K. Geim, M. Polini, Phys. Rev. B **94**, 155414 (2016). https://doi.org/10.1103/PhysRevB.94.155414

96. L.S. Levitov, G. Falkovich, Nat. Phys. **12**(7), 672 (2016). https://doi.org/10.1038/nphys3667
97. R. Moessner, P. Surówka, P. Witkowski, Phys. Rev. B **97**, 161112 (2018). https://doi.org/10.1103/PhysRevB.97.161112
98. R. Moessner, N. Morales-Durán, P. Surówka, P. Witkowski, Phys. Rev. B **100**, 155115 (2019). https://doi.org/10.1103/PhysRevB.100.155115
99. J. Mayzel, V. Steinberg, A. Varshney, Nat. Commun. **10**, 937 (2019). https://doi.org/10.1038/s41467-019-08916-5
100. A.V. Shytov, J.F. Kong, G. Falkovich, L.S. Levitov, Phys. Rev. Lett. **121**, 176805 (2018). https://doi.org/10.1103/PhysRevLett.121.176805
101. H. Guo, E. Ilseven, G. Falkovich, L.S. Levitov, Proc. Natl. Acad. Sci. **114**(12), 3068 (2017). https://doi.org/10.1073/pnas.1612181114
102. B.J. van Wees, H. van Houten, C.W.J. Beenakker, J.G. Williamson, L.P. Kouwenhoven, D. van der Marel, C.T. Foxon, Phys. Rev. Lett. **60**, 848 (1988). https://doi.org/10.1103/PhysRevLett.60.848
103. D.A. Wharam, T.J. Thornton, R. Newbury, M. Pepper, H. Ahmed, J.E.F. Frost, D.G. Hasko, D.C. Peacock, D.A. Ritchie, G.A.C. Jones, J. Phys. C **21**(8), L209 (1988). https://doi.org/10.1088/0022-3719/21/8/002
104. Y.V. Sharvin, Zh. Eksp. Teor. Fiz. **48**, 984 (1965). [Sov. Phys. JETP **21**, 655 (1965)]
105. G. Zhang, V. Kachorovskii, K. Tikhonov, I. Gornyi, Phys. Rev. B **104**, 075417 (2021). https://doi.org/10.1103/PhysRevB.104.075417
106. A. Lucas, Phys. Rev. B **95**, 115425 (2017). https://doi.org/10.1103/PhysRevB.95.115425
107. H. Guo, E. Ilseven, G. Falkovich, L. Levitov. Stokes paradox, back reflections and interaction-enhanced conduction (2017). https://doi.org/10.48550/arXiv.1612.09239
108. C.W. Oseen, Ark. f. Mat., Astr. och Fysik (Stockholm) **6**, 29 (1910)
109. P.S. Alekseev, Phys. Rev. Lett. **117**, 166601 (2016). https://doi.org/10.1103/PhysRevLett.117.166601
110. T. Scaffidi, N. Nandi, B. Schmidt, A.P. Mackenzie, J.E. Moore, Phys. Rev. Lett. **118**, 226601 (2017). https://doi.org/10.1103/PhysRevLett.118.226601
111. S. Tarucha, T. Saku, Y. Tokura, Y. Hirayama, Phys. Rev. B **47**, 4064 (1993). https://doi.org/10.1103/PhysRevB.47.4064
112. S. Datta, *Electron transport in mesoscopic systems* (Cambridge University Press, Cambridge, 1997). https://doi.org/10.1017/CBO9780511805776
113. F.M.D. Pellegrino, I. Torre, M. Polini, Phys. Rev. B **96**, 195401 (2017). https://doi.org/10.1103/PhysRevB.96.195401
114. P.S. Alekseev, A.P. Dmitriev, I.V. Gornyi, V.Y. Kachorovskii, B.N. Narozhny, M. Titov, Phys. Rev. B **97**, 085109 (2018). https://doi.org/10.1103/PhysRevB.97.085109
115. P.S. Alekseev, A.P. Dmitriev, I.V. Gornyi, V.Y. Kachorovskii, B.N. Narozhny, M. Titov, Phys. Rev. B **98**, 125111 (2018). https://doi.org/10.1103/PhysRevB.98.125111
116. J.L.M. Poiseuille, C.R. Acad, Science **11**, 961 (1840)
117. E.I. Kiselev, J. Schmalian, Phys. Rev. B **99**, 035430 (2019). https://doi.org/10.1103/PhysRevB.99.035430
118. J.R. Maze, P.L. Stanwix, J.S. Hodges, S. Hong, J.M. Taylor, P. Cappellaro, L. Jiang, M.V. Gurudev Dutt, E. Togan, A.S. Zibrov, A. Yacoby, R.L. Walsworth, M.D. Lukin, Nature **455**, 644 (2008). https://doi.org/10.1038/nature07279
119. B.N. Narozhny, M. Schütt, Phys. Rev. B **100**, 035125 (2019). https://doi.org/10.1103/PhysRevB.100.035125
120. B.N. Narozhny, Ann. Phys. **411**, 167979 (2019). https://doi.org/10.1016/j.aop.2019.167979
121. U. Briskot, M. Schütt, I.V. Gornyi, M. Titov, B.N. Narozhny, A.D. Mirlin, Phys. Rev. B **92**, 115426 (2015). https://doi.org/10.1103/PhysRevB.92.115426
122. M. Schütt, P.M. Ostrovsky, I.V. Gornyi, A.D. Mirlin, Phys. Rev. B **83**, 155441 (2011). https://doi.org/10.1103/PhysRevB.83.155441
123. M. Müller, S. Sachdev, Phys. Rev. B **78**, 115419 (2008). https://doi.org/10.1103/PhysRevB.78.115419
124. B.N. Narozhny, I.V. Gornyi, M. Titov, M. Schütt, A.D. Mirlin, Phys. Rev. B **91**, 035414 (2015). https://doi.org/10.1103/PhysRevB.91.035414
125. B.N. Narozhny, I.V. Gornyi, M. Titov, Phys. Rev. B **104**, 075443 (2021). https://doi.org/10.1103/PhysRevB.104.075443
126. J.P. Eisenstein, in *Perspectives in Quantum Hall Effects*, ed. by S.D. Sarma, A. Pinczuk (Wiley, New York, 1997). https://doi.org/10.1002/9783527617258.ch2

127. S.M. Girvin, A.H. MacDonald, in *Perspectives in Quantum Hall Effects*, ed. by S.D. Sarma, A. Pinczuk (Wiley, New York, 1997). https://doi.org/10.1002/9783527617258.ch5
128. B.A. Bernevig, T.L. Hughes, *Topological insulators and topological superconductors* (Princeton University Press, Princeton, 2013)
129. Y.T. Cui, B. Wen, E.Y. Ma, G. Diankov, Z. Han, F. Amet, T. Taniguchi, K. Watanabe, D. Goldhaber-Gordon, C.R. Dean, Z.X. Shen, Phys. Rev. Lett. **117**, 186601 (2016). https://doi.org/10.1103/PhysRevLett.117.186601
130. J. Chae, S. Jung, S. Woo, H. Baek, J. Ha, Y.J. Song, Y.W. Son, N.B. Zhitenev, J.A. Stroscio, Y. Kuk, Nano Lett. **12**(4), 1839 (2012). https://doi.org/10.1021/nl2041222
131. J.M. Marmolejo-Tejada, J.H. García, M.D. Petrović, P.H. Chang, X.L. Sheng, A. Cresti, P. Plecháč, S. Roche, B.K. Nikolić, J. Phys. Mater. **1**(1), 015006 (2018). https://doi.org/10.1088/2515-7639/aad585
132. M.T. Allen, O. Shtanko, I.C. Fulga, A.R. Akhmerov, K. Watanabe, T. Taniguchi, P. Jarillo-Herrero, L.S. Levitov, A. Yacoby, Nat. Phys. **12**, 128 (2016). https://doi.org/10.1038/nphys3534
133. S.M. Sze, K.K. Ng, Physics of semiconductor devices (Wiley, New York (2006). https://doi.org/10.1002/0470068329
134. W. Schottky, Naturwissenschaften **26**, 843 (1938). https://doi.org/10.1007/BF01774216
135. M.J. Zhu, A.V. Kretinin, M.D. Thompson, D.A. Bandurin, S. Hu, G.L. Yu, J. Birkbeck, A. Mishchenko, I.J. Vera-Marun, K. Watanabe, T. Taniguchi, M. Polini, J.R. Prance, K.S. Novoselov, A.K. Geim, M. Ben Shalom, Nat. Commun. **8**, 14552 (2017). https://doi.org/10.1038/ncomms14552
136. D. Halbertal, M. Ben Shalom, A. Uri, K. Bagani, A.Y. Meltzer, I. Markus, Y. Myasoedov, J. Birkbeck, L.S. Levitov, A.K. Geim, E. Zeldov, Science **358**, 1303 (2017). https://doi.org/10.1126/science.aan0877
137. B.A. Braem, C. Gold, S. Hennel, M. Röösli, M. Berl, W. Dietsche, W. Wegscheider, K. Ensslin, T. Ihn, N J. Phys. **20**(7), 073015 (2018). https://doi.org/10.1088/1367-2630/aad068
138. M. Shavit, A.V. Shytov, G. Falkovich, Phys. Rev. Lett. **123**, 026801 (2019). https://doi.org/10.1103/PhysRevLett.123.026801
139. O.M. Corbino, Nuovo Cimento **1**, 397 (1911). https://doi.org/10.1007/BF02958241
140. A. Tomadin, G. Vignale, M. Polini, Phys. Rev. Lett. **113**, 235901 (2014). https://doi.org/10.1103/PhysRevLett.113.235901
141. R. Franz, G. Wiedemann, Annalen der Physik **165**(8), 497 (1853). https://doi.org/10.1002/andp.18531650802
142. L. Lorenz, Annalen der Physik **223**(11), 429 (1872). https://doi.org/10.1002/andp.18722231107
143. J.G. Hust, A.B. Lankford, *Thermal conductivity of aluminum, copper, iron and tungsten for temperatures from 1 K to the melting point* (1984). National Bureau of Standards, Boulder, Colorado; NBSIR 84-3007
144. Y.M. Zuev, W. Chang, P. Kim, Phys. Rev. Lett. **102**, 096807 (2009). https://doi.org/10.1103/PhysRevLett.102.096807
145. J.G. Checkelsky, N.P. Ong, Phys. Rev. B **80**, 081413(R) (2009). https://doi.org/10.1103/PhysRevB.80.081413
146. A. Block, A. Principi, N.C.H. Hesp, A.W. Cummings, M. Liebel, K. Watanabe, T. Taniguchi, S. Roche, F.H.L. Koppens, N.F. van Hulst, K.J. Tielrooij, Nat. Nanotechnol. **16**, 1195 (2021). https://doi.org/10.1038/s41565-021-00957-6
147. S.A. Hartnoll, P.K. Kovtun, M. Müller, S. Sachdev, Phys. Rev. B **76**, 144502 (2007). https://doi.org/10.1103/PhysRevB.76.144502
148. P.R. Wallace, Phys. Rev. **71**, 622 (1947). https://doi.org/10.1103/PhysRev.71.622
149. G.W. Semenoff, Phys. Rev. Lett. **53**, 2449 (1984). https://doi.org/10.1103/PhysRevLett.53.2449
150. D.P. DiVincenzo, E.J. Mele, Phys. Rev. B **29**, 1685 (1984). https://doi.org/10.1103/PhysRevB.29.1685
151. K.S. Novoselov, A.K. Geim, S.V. Morozov, D. Jiang, M.I. Katsnelson, I.V. Grigorieva, S.V. Dubonos, A.A. Firsov, Nature **438**, 197 (2005). https://doi.org/10.1038/nature04233
152. M. Müller, L. Fritz, S. Sachdev, Phys. Rev. B **78**, 115406 (2008). https://doi.org/10.1103/PhysRevB.78.115406
153. L. Fritz, J. Schmalian, M. Müller, S. Sachdev, Phys. Rev. B **78**, 085416 (2008). https://doi.org/10.1103/PhysRevB.78.085416
154. E.G. Mishchenko, Phys. Rev. Lett. **98**, 216801 (2007). https://doi.org/10.1103/PhysRevLett.98.216801

155. E.G. Mishchenko, EPL (Europhys. Lett.) **83**(1), 17005 (2008). https://doi.org/10.1209/0295-5075/83/17005
156. J. Gooth, F. Menges, N. Kumar, V. Süβ, C. Shekhar, Y. Sun, U. Drechsler, R. Zierold, C. Felser, B. Gotsmann, Nat. Commun. **9**, 4093 (2018). https://doi.org/10.1038/s41467-018-06688-y
157. N. Kumar, Y. Sun, M. Nicklas, S.J. Watzman, O. Young, I. Leermakers, J. Hornung, J. Klotz, J. Gooth, K. Manna, V. Süß, S.N. Guin, T. Förster, M. Schmidt, L. Muechler, B. Yan, P. Werner, W. Schnelle, U. Zeitler, J. Wosnitza, S. Parkin, C. Felser, C. Shekhar, Nat. Commun. **10**(1), 2475 (2019). https://doi.org/10.1038/s41467-019-10126-y
158. H.Y. Xie, M.S. Foster, Phys. Rev. B **93**, 195103 (2016). https://doi.org/10.1103/PhysRevB.93.195103
159. A. Principi, G. Vignale, Phys. Rev. Lett. **115**, 056603 (2015). https://doi.org/10.1103/PhysRevLett.115.056603
160. A. Lucas, S. DasSarma, Phys. Rev. B **97**, 245128 (2018). https://doi.org/10.1103/PhysRevB.97.245128
161. M.R. van Delft, Y. Wang, C. Putzke, J. Oswald, G. Varnavides, C.A.C. Garcia, C. Guo, H. Schmid, V. Süss, H. Borrmann, J. Diaz, Y. Sun, C. Felser, B. Gotsmann, P. Narang, P.J.W. Moll, Nat. Commun. **12**, 4799 (2021). https://doi.org/10.1038/s41467-021-25037-0
162. E.H. Sondheimer, Phys. Rev. **80**, 401 (1950). https://doi.org/10.1103/PhysRev.80.401
163. E. Shuryak, Prog. Part. Nucl. Phys. **62**(1), 48 (2009). https://doi.org/10.1016/j.ppnp.2008.09.001
164. S.N. Shore, Astrophysical hydrodynamics: an introduction (Wiley. Weinheim (2007). https://doi.org/10.1002/9783527619054
165. M.S. Steinberg, Phys. Rev. **109**, 1486 (1958). https://doi.org/10.1103/PhysRev.109.1486
166. M.I. Katsnelson, *Graphene* (Cambridge University Press, Cambridge, 2012). https://doi.org/10.1017/CBO9781139031080
167. M.J. Bhaseen, A.G. Green, S.L. Sondhi, Phys. Rev. B **79**, 094502 (2009). https://doi.org/10.1103/PhysRevB.79.094502
168. L. Euler, Mémoires de l'académie des sciences de Berlin **11**, 274 (1757)
169. T.V. Phan, J.C.W. Song, L.S. Levitov (2013). https://doi.org/10.48550/arXiv.1306.4972
170. L.S. Levitov, A.V. Shtyk, M.V. Feigelman, Phys. Rev. B **88**, 235403 (2013). https://doi.org/10.1103/PhysRevB.88.235403
171. Z. Sun, D.N. Basov, M.M. Fogler, Proc. Natl. Acad. Sci. **115**(13), 3285 (2018). https://doi.org/10.1073/pnas.1717010115
172. D. Svintsov, Phys. Rev. B **97**, 121405(R) (2018). https://doi.org/10.1103/PhysRevB.97.121405
173. A. Lucas, S. Das Sarma, Phys. Rev. B **97**, 115449 (2018). https://doi.org/10.1103/PhysRevB.97.115449
174. E.I. Kiselev, J. Schmalian, Phys. Rev. B **102**, 245434 (2020). https://doi.org/10.1103/PhysRevB.102.245434
175. D.V. Fateev, V.V. Popov, Semiconductors **54**, 941 (2020). https://doi.org/10.1134/S1063782620080084
176. B.N. Narozhny, I.V. Gornyi, M. Titov, Phys. Rev. B **103**, 115402 (2021). https://doi.org/10.1103/PhysRevB.103.115402
177. M. Auslender, M.I. Katsnelson, Phys. Rev. B **76**, 235425 (2007). https://doi.org/10.1103/PhysRevB.76.235425
178. A.A. Kozikov, A.K. Savchenko, B.N. Narozhny, A.V. Shytov, Phys. Rev. B **82**, 075424 (2010). https://doi.org/10.1103/PhysRevB.82.075424
179. D.E. Sheehy, J. Schmalian, Phys. Rev. Lett. **99**, 226803 (2007). https://doi.org/10.1103/PhysRevLett.99.226803
180. M. Müller, J. Schmalian, L. Fritz, Phys. Rev. Lett. **103**, 025301 (2009). https://doi.org/10.1103/PhysRevLett.103.025301
181. J. Gonzalez, F. Guinea, M.A.H. Vozmediano, Nucl. Phys. B **424**(3), 595 (1994). https://doi.org/10.1016/0550-3213(94)90410-3
182. J. González, F. Guinea, M.A.H. Vozmediano, Phys. Rev. B **59**, R2474 (1999). https://doi.org/10.1103/PhysRevB.59.R2474
183. J.M. Link, B.N. Narozhny, E.I. Kiselev, J. Schmalian, Phys. Rev. Lett. **120**, 196801 (2018). https://doi.org/10.1103/PhysRevLett.120.196801
184. I.L. Aleiner, O. Agam, Ann. Phys. **385**, 716 (2017). https://doi.org/10.1016/j.aop.2017.08.017
185. A.H. Castro Neto, F. Guinea, N.M.R. Peres, K.S. Novoselov, A.K. Geim, Rev. Mod. Phys. **81**, 109 (2009). https://doi.org/10.1103/RevModPhys.81.109

186. G. Wagner, D.X. Nguyen, S.H. Simon, Phys. Rev. B **101**, 245438 (2020). https://doi.org/10.1103/PhysRevB.101.245438
187. H.K. Tang, J.N. Leaw, J.N.B. Rodrigues, I.F. Herbut, P. Sengupta, F.F. Assaad, S. Adam, Science **361**(6402), 570 (2018). https://doi.org/10.1126/science.aao2934
188. D.C. Elias, R.V. Gorbachev, A.S. Mayorov, S.V. Morozov, A.A. Zhukov, P. Blake, L.A. Ponomarenko, I.V. Grigorieva, K.S. Novoselov, F. Guinea, A.K. Geim, Nat. Phys. **7**, 701 (2011). https://doi.org/10.1038/NPHYS2049
189. G. Alymov, V. Vyurkov, V. Ryzhii, A. Satou, D. Svintsov, Phys. Rev. B **97**, 205411 (2018). https://doi.org/10.1103/PhysRevB.97.205411
190. A. Tomadin, D. Brida, G. Cerullo, A.C. Ferrari, M. Polini, Phys. Rev. B **88**, 035430 (2013). https://doi.org/10.1103/PhysRevB.88.035430
191. A.B. Kashuba, Phys. Rev. B **78**, 085415 (2008). https://doi.org/10.1103/PhysRevB.78.085415
192. M. Schütt, P.M. Ostrovsky, M. Titov, I.V. Gornyi, B.N. Narozhny, A.D. Mirlin, Phys. Rev. Lett. **110**, 026601 (2013). https://doi.org/10.1103/PhysRevLett.110.026601
193. J.C.W. Song, M.Y. Reizer, L.S. Levitov, Phys. Rev. Lett. **109**, 106602 (2012). https://doi.org/10.1103/PhysRevLett.109.106602
194. M.W. Graham, S.F. Shi, D.C. Ralph, J. Park, P.L. McEuen, Nat. Phys. **9**, 103 (2013). https://doi.org/10.1038/nphys2493
195. A.C. Betz, S.H. Jhang, E. Pallecchi, R. Ferreira, G. Fève, J.M. Berroir, B. Plaçais, Nat. Phys. **9**, 109 (2013). https://doi.org/10.1038/nphys2494
196. K.S. Tikhonov, I.V. Gornyi, V.Y. Kachorovskii, A.D. Mirlin, Phys. Rev. B **97**, 085415 (2018). https://doi.org/10.1103/PhysRevB.97.085415
197. J.F. Kong, L. Levitov, D. Halbertal, E. Zeldov, Phys. Rev. B **97**, 245416 (2018). https://doi.org/10.1103/PhysRevB.97.245416
198. M. Zarenia, A. Principi, G. Vignale, Phys. Rev. B **102**, 214304 (2020). https://doi.org/10.1103/PhysRevB.102.214304
199. P.S. Alekseev, A.P. Dmitriev, I.V. Gornyi, V.Y. Kachorovskii, B.N. Narozhny, M. Schütt, M. Titov, Phys. Rev. B **95**, 165410 (2017). https://doi.org/10.1103/PhysRevB.95.165410
200. R.V. Gorbachev, A.K. Geim, M.I. Katsnelson, K.S. Novoselov, T. Tudorovskiy, I.V. Grigorieva, A.H. MacDonald, S.V. Morozov, K. Watanabe, T. Taniguchi, L.A. Ponomarenko, Nat. Phys. **8**(12), 896 (2012). https://doi.org/10.1038/nphys2441
201. B.N. Narozhny, I.V. Gornyi, Front. Phys. **9**, 108 (2021). https://doi.org/10.3389/fphy.2021.640649
202. R. Bistritzer, A.H. MacDonald, Phys. Rev. Lett. **102**, 206410 (2009). https://doi.org/10.1103/PhysRevLett.102.206410
203. W.K. Tse, S. Das Sarma, Phys. Rev. B **79**, 235406 (2009). https://doi.org/10.1103/PhysRevB.79.235406
204. H.Y. Xie, A. Levchenko, Phys. Rev. B **99**, 045434 (2019). https://doi.org/10.1103/PhysRevB.99.045434
205. O. Kashuba, B. Trauzettel, L.W. Molenkamp, Phys. Rev. B **97**, 205129 (2018). https://doi.org/10.1103/PhysRevB.97.205129
206. B.N. Narozhny, Phys. Rev. B **100**, 115434 (2019). https://doi.org/10.1103/PhysRevB.100.115434
207. G. Falkovich, L.S. Levitov, Phys. Rev. Lett. **119**, 066601 (2017). https://doi.org/10.1103/PhysRevLett.119.066601
208. I.M. Khalatnikov, Zh. Eksp. Teor. Fiz. **29**, 253 (1956). [Soviet Physics JETP-USSR **2**, 169 (1956)]
209. J. Sykes, G.A. Brooker, Ann. Phys. **56**(1), 1 (1970). https://doi.org/10.1016/0003-4916(70)90002-3
210. V.A. Zakharov, I.S. Burmistrov, Phys. Rev. B **103**, 235305 (2021). https://doi.org/10.1103/PhysRevB.103.235305
211. B. Bradlyn, M. Goldstein, N. Read, Phys. Rev. B **86**, 245309 (2012). https://doi.org/10.1103/PhysRevB.86.245309
212. P. Rao, B. Bradlyn, Phys. Rev. X **10**, 021005 (2020). https://doi.org/10.1103/PhysRevX.10.021005
213. L.V. Delacrétaz, A. Gromov, Phys. Rev. Lett. **119**, 226602 (2017). https://doi.org/10.1103/PhysRevLett.119.226602
214. T. Holder, R. Queiroz, A. Stern, Phys. Rev. Lett. **123**, 106801 (2019). https://doi.org/10.1103/PhysRevLett.123.106801
215. J.M. Link, D.E. Sheehy, B.N. Narozhny, J. Schmalian, Phys. Rev. B **98**, 195103 (2018). https://doi.org/10.1103/PhysRevB.98.195103

216. A. Principi, G. Vignale, M. Carrega, M. Polini, Phys. Rev. B **93**, 125410 (2016). https://doi.org/10.1103/PhysRevB.93.125410
217. I.S. Burmistrov, M. Goldstein, M. Kot, V.D. Kurilovich, P.D. Kurilovich, Phys. Rev. Lett. **123**, 026804 (2019). https://doi.org/10.1103/PhysRevLett.123.026804
218. Y. Liao, V. Galitski, Phys. Rev. B **101**, 195106 (2020). https://doi.org/10.1103/PhysRevB.101.195106
219. B.N. Narozhny, A. Levchenko, Rev. Mod. Phys. **88**, 025003 (2016). https://doi.org/10.1103/RevModPhys.88.025003
220. B.N. Narozhny, M. Titov, I.V. Gornyi, P.M. Ostrovsky, Phys. Rev. B **85**, 195421 (2012). https://doi.org/10.1103/PhysRevB.85.195421
221. P.S. Alekseev, Phys. Rev. B **98**, 165440 (2018). https://doi.org/10.1103/PhysRevB.98.165440
222. B. Laikhtman, Phys. Rev. B **45**, 1259 (1992). https://doi.org/10.1103/PhysRevB.45.1259
223. R.N. Gurzhi, A.N. Kalinenko, A.I. Kopeliovich, Phys. Rev. Lett. **74**, 3872 (1995). https://doi.org/10.1103/PhysRevLett.74.3872
224. P. Ledwith, H. Guo, A. Shytov, L. Levitov, Phys. Rev. Lett. **123**, 116601 (2019). https://doi.org/10.1103/PhysRevLett.123.116601
225. P.S. Alekseev, A.P. Dmitriev, Phys. Rev. B **102**, 241409 (2020). https://doi.org/10.1103/PhysRevB.102.241409
226. H. Isobe, B.J. Yang, A. Chubukov, J. Schmalian, N. Nagaosa, Phys. Rev. Lett. **116**, 076803 (2016). https://doi.org/10.1103/PhysRevLett.116.076803
227. A. Kobayashi, Y. Suzumura, F. Piéchon, G. Montambaux, Phys. Rev. B **84**, 075450 (2011). https://doi.org/10.1103/PhysRevB.84.075450
228. V. Pardo, W.E. Pickett, Phys. Rev. Lett. **102**, 166803 (2009). https://doi.org/10.1103/PhysRevLett.102.166803
229. S. Banerjee, R.R.P. Singh, V. Pardo, W.E. Pickett, Phys. Rev. Lett. **103**, 016402 (2009). https://doi.org/10.1103/PhysRevLett.103.016402
230. C. Fang, L. Fu, Phys. Rev. B **91**, 161105 (2015). https://doi.org/10.1103/PhysRevB.91.161105
231. S.M. Huang, S.Y. Xu, I. Belopolski, C.C. Lee, G. Chang, T.R. Chang, B. Wang, N. Alidoust, G. Bian, M. Neupane, D. Sanchez, H. Zheng, H.T. Jeng, A. Bansil, T. Neupert, H. Lin, M.Z. Hasan, Proc. Natl. Acad. Sci. **113**(5), 1180 (2016). https://doi.org/10.1073/pnas.1514581113
232. P.K. Kovtun, D.T. Son, A.O. Starinets, Phys. Rev. Lett. **94**, 111601 (2005). https://doi.org/10.1103/PhysRevLett.94.111601
233. F. Peña Benitez, K. Saha, P. Surówka, Phys. Rev. B **99**, 045141 (2019). https://doi.org/10.1103/PhysRevB.99.045141
234. C. Hoyos, R. Lier, F. Peña Benitez, P. Surówka, Phys. Rev. B **102**, 081303 (2020). https://doi.org/10.1103/PhysRevB.102.081303
235. J.M. Luttinger, Phys. Rev. **102**, 1030 (1956). https://doi.org/10.1103/PhysRev.102.1030
236. A.A. Abrikosov, Zh. Eksp. Teor. Fiz. **66**, 1443 (1974). [Sov. Phys. JETP **39**, 709 (1974)]
237. J.M. Link, I.F. Herbut, Phys. Rev. B **101**, 125128 (2020). https://doi.org/10.1103/PhysRevB.101.125128
238. J.C. Maxwell, Philos. Trans. R. Soc. **170**, 231 (1879). https://doi.org/10.1098/rstl.1879.0067
239. L.A. Falkovsky, Adv. Phys. **32**(5), 753 (1983). https://doi.org/10.1080/00018738300101601
240. T. Holder, R. Queiroz, T. Scaffidi, N. Silberstein, A. Rozen, J.A. Sulpizio, L. Ella, S. Ilani, A. Stern, Phys. Rev. B **100**, 245305 (2019). https://doi.org/10.1103/PhysRevB.100.245305
241. O.E. Raichev, Phys. Rev. B **105**, L041301 (2022). https://doi.org/10.1103/PhysRevB.105.L041301
242. A.i.e.i.f.C. Keser, D.Q. Wang, O. Klochan, D.Y.H. Ho, O.A. Tkachenko, V.A. Tkachenko, D. Culcer, S. Adam, I. Farrer, D.A. Ritchie, O.P. Sushkov, A.R. Hamilton, Phys. Rev. X **11**, 031030 (2021). https://doi.org/10.1103/PhysRevX.11.031030
243. M.P. Marder, *Condensed matter physics* (Wiley, New York, 2010). https://doi.org/10.1002/9780470949955
244. R. Landauer, IBM J. Res. Dev **1**(3), 223 (1957). https://doi.org/10.1147/rd.13.0223
245. A. Lucas, Phys. Rev. B **93**, 245153 (2016). https://doi.org/10.1103/PhysRevB.93.245153
246. M. Semenyakin, G. Falkovich, Phys. Rev. B **97**, 085127 (2018). https://doi.org/10.1103/PhysRevB.97.085127
247. G. Giuliani, G. Vignale, *Quantum theory of the electron liquid* (Cambridge University Press, Cambridge, 2005). https://doi.org/10.1017/CBO9780511619915
248. A. Hill, S.A. Mikhailov, K. Ziegler, EPL (Europhys. Lett.) **87**(2), 27005 (2009). https://doi.org/10.1209/0295-5075/87/27005

249. A. Principi, R. Asgari, M. Polini, Solid State Commun. **151**(21), 1627 (2011). https://doi.org/10.1016/j.ssc.2011.07.015
250. Z. Fei, A.S. Rodin, G.O. Andreev, W. Bao, A.S. McLeod, M. Wagner, L.M. Zhang, Z. Zhao, M. Thiemens, G. Dominguez, M.M. Fogler, A.H.C. Neto, C.N. Lau, F. Keilmann, D.N. Basov, Nature **487**(7405), 82 (2012). https://doi.org/10.1038/nature11253
251. J. Chen, M. Badioli, P. Alonso-González, S. Thongrattanasiri, F. Huth, J. Osmond, M. Spasenović, A. Centeno, A. Pesquera, P. Godignon, A. Zurutuza Elorza, N. Camara, F.J.G. de Abajo, R. Hillenbrand, F.H.L. Koppens, Nature **487**, 77 (2012). https://doi.org/10.1038/nature11254
252. G.X. Ni, L. Wang, M.D. Goldflam, M. Wagner, Z. Fei, A.S. McLeod, M.K. Liu, F. Keilmann, B. Özyilmaz, A.H. Castro Neto, J. Hone, F.M. M., B.D. N., Nat. Photon. **10**, 244 (2016). https://doi.org/10.1038/nphoton.2016.45
253. M.B. Lundeberg, Y. Gao, R. Asgari, C. Tan, B. Van Duppen, M. Autore, P. Alonso-González, A. Woessner, K. Watanabe, T. Taniguchi, R. Hillenbrand, J. Hone, M. Polini, F.H.L. Koppens, Science **357**(6347), 187 (2017). https://doi.org/10.1126/science.aan2735
254. D. Alcaraz Iranzo, S. Nanot, E.J.C. Dias, I. Epstein, C. Peng, D.K. Efetov, M.B. Lundeberg, R. Parret, J. Osmond, J.Y. Hong, J. Kong, D.R. Englund, N.M.R. Peres, F.H.L. Koppens, Science **360**(6386), 291 (2018). https://doi.org/10.1126/science.aar8438
255. P. Novelli, I. Torre, F.H.L. Koppens, F. Taddei, M. Polini, Phys. Rev. B **102**, 125403 (2020). https://doi.org/10.1103/PhysRevB.102.125403
256. T. Giovannini, L. Bonatti, M. Polini, C. Cappelli, J. Phys. Chem. Lett. **11**(18), 7595 (2020). https://doi.org/10.1021/acs.jpclett.0c02051
257. N.C.H. Hesp, I. Torre, D. Rodan-Legrain, P. Novelli, Y. Cao, S. Carr, S. Fang, P. Stepanov, D. Barcons-Ruiz, H. Herzig-Sheinfux, K. Watanabe, T. Taniguchi, D.K. Efetov, E. Kaxiras, P. Jarillo-Herrero, M. Polini, F.H.L. Koppens, Observation of interband collective excitations in twisted bilayer graphene (2021). https://doi.org/10.1038/s41567-021-01327-8
258. A.T. Costa, P.A.D. Gonçalves, D.N. Basov, F.H.L. Koppens, N.A. Mortensen, N.M.R. Peres, PNAS **118**(4), e2012847118 (2021). https://doi.org/10.1073/pnas.2012847118
259. A. Klein, D.L. Maslov, L.P. Pitaevskii, A.V. Chubukov, Phys. Rev. Res. **1**, 033134 (2019). https://doi.org/10.1103/PhysRevResearch.1.033134
260. B.A. Ferreira, B. Amorim, A.J. Chaves, N.M.R. Peres, Phys. Rev. A **101**, 033817 (2020). https://doi.org/10.1103/PhysRevA.101.033817
261. A. Klein, D.L. Maslov, A.V. Chubukov, NPJ Quantum Mater. **5**, 55 (2020). https://doi.org/10.1038/s41535-020-0250-4
262. Z.M. Raines, V.I. Fal'ko, L.I. Glazman, Phys. Rev. B **103**, 075422 (2021). https://doi.org/10.1103/PhysRevB.103.075422
263. I.L. Aleiner, B.I. Shklovskii, Phys. Rev. B **49**, 13721 (1994). https://doi.org/10.1103/PhysRevB.49.13721
264. V. Andreeva, D.A. Bandurin, M. Luskin, D. Margetis, Phys. Rev. B **102**, 205411 (2020). https://doi.org/10.1103/PhysRevB.102.205411
265. R. Cohen, M. Goldstein, Phys. Rev. B **98**, 235103 (2018). https://doi.org/10.1103/PhysRevB.98.235103
266. A. Levchenko, H.Y. Xie, A.V. Andreev, Phys. Rev. B **95**, 121301(R) (2017). https://doi.org/10.1103/PhysRevB.95.121301
267. S. Li, A. Levchenko, A.V. Andreev, Phys. Rev. B **102**, 075305 (2020). https://doi.org/10.1103/PhysRevB.102.075305
268. A. Hui, S. Lederer, V. Oganesyan, E.A. Kim, Phys. Rev. B **101**, 121107 (2020). https://doi.org/10.1103/PhysRevB.101.121107
269. S. Li, M. Khodas, A. Levchenko, Phys. Rev. B **104**, 155305 (2021). https://doi.org/10.1103/PhysRevB.104.155305
270. J.L.M. Poiseuille, Annales de chimie et de physique (Series 3) **21**, 76 (1847)
271. I. Matthaiakakis, D. Rodríguez Fernández, C. Tutschku, E.M. Hankiewicz, J. Erdmenger, R. Meyer, Phys. Rev. B **101**, 045423 (2020). https://doi.org/10.1103/PhysRevB.101.045423
272. A.A. Patel, R.A. Davison, A. Levchenko, Phys. Rev. B **96**, 205417 (2017). https://doi.org/10.1103/PhysRevB.96.205417
273. I. Mandal, A. Lucas, Phys. Rev. B **101**, 045122 (2020). https://doi.org/10.1103/PhysRevB.101.045122

274. E.I. Rashba, Z.S. Gribnikov, V.Y. Kravchenko, Usp. Fiz. Nauk **119**(5), 3 (1976). https://doi.org/10.3367/UFNr.0119.197605a.0003. [Sov. Phys. Usp. 19, 361 (1976)]
275. S. Li, A. Levchenko, A.V. Andreev, Phys. Rev. B **105**, 125302 (2022). https://doi.org/10.1103/PhysRevB.105.125302
276. A. Stern, T. Scaffidi, O. Reuven, C. Kumar, J. Birkbeck, S. Ilani (2021). https://doi.org/10.48550/arXiv.2110.15369
277. O.E. Raichev (2022). https://doi.org/10.48550/arXiv.2202.06623
278. M. Mendoza, H.J. Herrmann, S. Succi, Phys. Rev. Lett. **106**, 156601 (2011). https://doi.org/10.1103/PhysRevLett.106.156601
279. I. Meric, M.Y. Han, A.F. Young, B. Ozylmaz, P. Kim, K.L. Shepard, Nat. Nanotechnol. **3**, 654 (2008). https://doi.org/10.1038/nnano.2008.268
280. P.A. Cherenkov, C.R. Acad, Sci. USSR **2**, 451 (1934). https://doi.org/10.3367/UFNr.0093.196710n.0385. [Dokl. Akad. Nauk SSSR 2, 451 (1934)]
281. S.I. Vavilov, C.R. Acad, Sci. USSR **2**, 457 (1934). https://doi.org/10.3367/UFNr.0093.196710m.0383. [Dokl. Akad. Nauk SSSR 2, 457 (1934)]
282. I.E. Tamm, I.M. Frank, C.R. Acad, Sci. USSR **14**, 107 (1937). https://doi.org/10.3367/UFNr.0093.196710o.0388. [Dokl. Akad. Nauk SSSR 14, 107 (1937)]
283. D. Svintsov, Phys. Rev. B **100**, 195428 (2019). https://doi.org/10.1103/PhysRevB.100.195428
284. D. Svintsov, V. Vyurkov, V. Ryzhii, T. Otsuji, Phys. Rev. B **88**, 245444 (2013). https://doi.org/10.1103/PhysRevB.88.245444
285. T. Zdyrski, J. McGreevy, Phys. Rev. B **99**, 235435 (2019). https://doi.org/10.1103/PhysRevB.99.235435
286. V.E. Dorgan, M.H. Bae, E. Pop, Appl. Phys. Lett. **97**(8), 082112 (2010). https://doi.org/10.1063/1.3483130
287. D. Di Sante, J. Erdmenger, M. Greiter, I. Matthaiakakis, R. Meyer, D. Rodriguez Fernández, R. Thomale, E. van Loon, T. Wehling, Nat. Commun. **11**, 3997 (2020). https://doi.org/10.1038/s41467-020-17663-x
288. R.C.V. Coelho, M. Mendoza, M.M. Doria, H.J. Herrmann, Phys. Rev. B **96**, 184307 (2017). https://doi.org/10.1103/PhysRevB.96.184307
289. O. Furtmaier, M. Mendoza, I. Karlin, S. Succi, H.J. Herrmann, Phys. Rev. B **91**, 085401 (2015). https://doi.org/10.1103/PhysRevB.91.085401
290. Sir W. Thomson, F.R.S., Lond. Edinb. Dublin Philos. Mag. J. Sci. **42**(281), 362 (1871). https://doi.org/10.1080/14786447108640585
291. H. Helmholz, Monatsberichte der Königlichen Preussische Akademie der Wissenschaften zu Berlin **23**, 215 (1868)
292. H. Bénard, Les tourbillons cellulaires dans une nappe liquide propageant de la chaleur par convection en régime permanent. Ph.D. thesis, Collège de France (1901)
293. F.R.S. Lord Rayleigh, Lond. Edinb. Dublin Philos. Mag. Jo. Sci. **32**, 529 (1916). https://doi.org/10.1080/14786441608635602
294. L. Bazzanini, A. Gabbana, D. Simeoni, S. Succi, R. Tripiccione, J. Comput. Sci. **51**, 101320 (2021). https://doi.org/10.1016/j.jocs.2021.101320
295. C.B. Mendl, A. Lucas, Appl. Phys. Lett. **112**(12), 124101 (2018). https://doi.org/10.1063/1.5022187
296. J. Crabb, X. Cantos-Roman, J.M. Jornet, G.R. Aizin, Phys. Rev. B **104**, 155440 (2021). https://doi.org/10.1103/PhysRevB.104.155440
297. K. Li, Y. Hao, X. Jin, W. Lu, J. Phys. D Appl. Phys. **51**(3), 035104 (2017). https://doi.org/10.1088/1361-6463/aa9cd0
298. C.B. Mendl, M. Polini, A. Lucas, Appl. Phys. Lett. **118**(1), 013105 (2021). https://doi.org/10.1063/5.0030869
299. J.H. Farrel, N. Grisouard, T. Scaffidi (2022). https://doi.org/10.48550/arXiv.2112.07683
300. A. Hui, V. Oganesyan, E.A. Kim, Phys. Rev. B **103**, 235152 (2021). https://doi.org/10.1103/PhysRevB.103.235152
301. D. Bernoulli, *Hydrodynamica, sive de viribus et motibus fluidorum commentarii* (Strasbourg, 1738). https://doi.org/10.3931/e-rara-3911
302. C. Eckart, Phys. Rev. **73**, 68 (1948). https://doi.org/10.1103/PhysRev.73.68
303. F.R.S. LordRayleigh, Philos. Trans. **175**, 1 (1884). https://doi.org/10.1098/rstl.1884.0002
304. J. Maldacena, Adv. Theor. Math. Phys. **2**(2), 231 (1998). https://doi.org/10.4310/ATMP.1998.v2.n2.a1

305. A. Donos, S.A. Hartnoll, Nat. Phys. **9**, 649 (2013). https://doi.org/10.1038/nphys2701
306. S.A. Hartnoll, A. Lucas, S. Sachdev, *Holographic quantum matter* (MIT Press, Cambridge, 2018). https://doi.org/10.48550/arXiv.1612.07324
307. T. Schäfer, Annu. Rev. Nucl. Part. Sci. **64**(1), 125 (2014). https://doi.org/10.1146/annurev-nucl-102313-025439
308. J.E. Thomas, Nucl. Phys. A **830**(1–4), 665c (2009). https://doi.org/10.1016/j.nuclphysa.2009.09.055
309. S.A. Hartnoll, Nat. Phys. **11**(1), 54 (2015). https://doi.org/10.1038/nphys3174
310. G.A. Inkof, J.M.C. Küppers, J.M. Link, B. Goutéraux, J. Schmalian, J. High Energy Phys. **2020**(11), 88 (2020). https://doi.org/10.1007/JHEP11(2020)088
311. J.A.N. Bruin, H. Sakai, R.S. Perry, A.P. Mackenzie, Science **339**(6121), 804 (2013). https://doi.org/10.1126/science.1227612
312. J. Zaanen, Nat. Phys. **9**, 609 (2013). https://doi.org/10.1038/nphys2717
313. R.A. Davison, K. Schalm, J. Zaanen, Phys. Rev. B **89**, 245116 (2014). https://doi.org/10.1103/PhysRevB.89.245116
314. C. Proust, L. Taillefer, Annu. Rev. Condens. Matter Phys. **10**(1), 409 (2019). https://doi.org/10.1146/annurev-conmatphys-031218-013210
315. A. Legros, S. Benhabib, W. Tabis, F. Laliberté, M. Dion, M. Lizaire, B. Vignolle, D. Vignolles, H. Raffy, Z.Z. Li, P. Auban-Senzier, N. Doiron-Leyraud, P. Fournier, D. Colson, L. Taillefer, C. Proust, Nat. Phys. **15**(2), 142 (2019). https://doi.org/10.1038/s41567-018-0334-2
316. J. Pagline, R.L. Greene, Nat. Phys. **6**, 645 (2010). https://doi.org/10.1038/nphys1759
317. D.C. Johnston, Adv. Phys. **59**(6), 803 (2010). https://doi.org/10.1080/00018732.2010.513480
318. P. Dai, Rev. Mod. Phys. **87**, 855 (2015). https://doi.org/10.1103/RevModPhys.87.855
319. Q. Si, R. Yu, E. Abrahams, Nat. Rev. Mater. **1**(4), 16017 (2016). https://doi.org/10.1038/natrevmats.2016.17
320. Y. Cao, V. Fatemi, S. Fang, K. Watanabe, T. Taniguchi, E. Kaxiras, P. Jarillo-Herrero, Nature **556**, 45 (2018). https://doi.org/10.1038/nature23160
321. Y. Cao, D. Chowdhury, D. Rodan-Legrain, O. Rubies-Bigorda, K. Watanabe, T. Taniguchi, T. Senthil, P. Jarillo-Herrero, Phys. Rev. Lett. **124**(7), 076801 (2020). https://doi.org/10.1103/PhysRevLett.124.076801
322. G.T. Horowitz, V.E. Hubeny, Phys. Rev. D **62**, 024027 (2000). https://doi.org/10.1103/PhysRevD.62.024027
323. D. Forster, *Hydrodynamic fluctuations, broken symmetry, and correlation functions* (CRC Press, 2018). https://doi.org/10.1201/9780429493683
324. S.c.v. Grozdanov, K. Schalm, V. Scopelliti, Phys. Rev. Lett. **120**, 231601 (2018). https://doi.org/10.1103/PhysRevLett.120.231601
325. A. Bagrov, B. Craps, F. Galli, V. Keränen, E. Keski-Vakkuri, J. Zaanen, Phys. Rev. D **97**, 086005 (2018). https://doi.org/10.1103/PhysRevD.97.086005
326. S. Bhattacharyya, S. Minwalla, J. High Energy Phys. **2009**(09), 034 (2009). https://doi.org/10.1088/1126-6708/2009/09/034
327. J.M. Deutsch, Phys. Rev. A **43**, 2046 (1991). https://doi.org/10.1103/PhysRevA.43.2046
328. M. Srednicki, Phys. Rev. E **50**, 888 (1994). https://doi.org/10.1103/PhysRevE.50.888
329. J. Zaanen, SciPost Phys. **6**(5), 061 (2019). https://doi.org/10.21468/SciPostPhys.6.5.061
330. A. Lucas, Phys. Rev. Lett. **122**, 216601 (2019). https://doi.org/10.1103/PhysRevLett.122.216601
331. D. van der Marel, H.J.A. Molegraaf, J. Zaanen, Z. Nussinov, F. Carbone, A. Damascelli, H. Eisaki, M. Greven, P.H. Kes, M. Li, Nature **425**, 271 (2003). https://doi.org/10.1038/nature01978
332. R.A. Cooper, Y. Wang, B. Vignolle, O.J. Lipscombe, S.M. Hayden, Y. Tanabe, T. Adachi, Y. Koike, M. Nohara, H. Takagi, C. Proust, N.E. Hussey, Science **323**(5914), 603 (2009). https://doi.org/10.1126/science.1165015
333. L. Delacrétaz, B. Goutéraux, S.A. Hartnoll, A. Karlsson, SciPost Phys. **3**(3), 025 (2017). https://doi.org/10.21468/SciPostPhys.3.3.025
334. E.W. Huang, C.B. Mendl, S. Liu, S. Johnston, H.C. Jiang, B. Moritz, T.P. Devereaux, Science **358**(6367), 1161 (2017). https://doi.org/10.1126/science.aak9546
335. T. Andrade, A. Krikun, K. Schalm, J. Zaanen, Nat. Phys. **14**(10), 1049 (2018). https://doi.org/10.1038/s41567-018-0217-6
336. A. Amoretti, D. Areán, B. Goutéraux, D. Musso, Phys. Rev. Lett. **120**, 171603 (2018). https://doi.org/10.1103/PhysRevLett.120.171603
337. D.V. Khveshchenko, Lithuan. J. Phys. **61**, 42 (2021). https://doi.org/10.3952/physics.v61i1.4406

338. J. Erdmenger, I. Matthaiakakis, R. Meyer, D.R. Fernández, Phys. Rev. B **98**, 195143 (2018). https://doi.org/10.1103/PhysRevB.98.195143
339. R. Peierls, Annalen der Physik **404**(2), 154 (1932). https://doi.org/10.1002/andp.19324040203. [Ann. Phys. (5) 12, 154 (1932)]
340. L.E. Gurevich, Zh. Eksp. Teor. Fiz. **16**, 193 (1946). [J. Phys. (USSR) **9**, 857 (1945)]
341. L.E. Gurevich, Zh. Eksp. Teor. Fiz. **16**, 416 (1946). [J. Phys. (USSR) **10**, 67 (1946)]
342. Y.G. Gurevich, O.L. Mashkevich, Phys. Rep. **181**, 327 (1989). https://doi.org/10.1016/0370-1573(89)90011-2
343. C. Fu, T. Scaffidi, J. Waissman, Y. Sun, R. Saha, S.J. Watzman, A.K. Srivastava, G. Li, W. Schnelle, P. Werner, M.E. Kamminga, S. Sachdev, S.S.P. Parkin, S.A. Hartnoll, C. Felser, J. Gooth (2018). https://doi.org/10.48550/arXiv.1802.09468
344. X. Huang, A. Lucas, Phys. Rev. B **103**, 155128 (2021). https://doi.org/10.1103/PhysRevB.103.155128
345. A. Levchenko, J. Schmalian, Ann. Phys. **419**, 168218 (2020). https://doi.org/10.1016/j.aop.2020.168218
346. N. Nandi, T. Scaffidi, P. Kushwaha, S. Khim, M.E. Barber, V. Sunko, F. Mazzola, P.D.C. King, H. Rosner, P.J.W. Moll, M. König, J.E. Moore, S. Hartnoll, A.P. Mackenzie, NPJ Quant. Mater. **3**(1), 66 (2018). https://doi.org/10.1038/s41535-018-0138-8
347. C.Q. Cook, A. Lucas, Phys. Rev. B **99**, 235148 (2019). https://doi.org/10.1103/PhysRevB.99.235148
348. J.M. Link, P.P. Orth, D.E. Sheehy, J. Schmalian, Phys. Rev. B **93**, 235447 (2016). https://doi.org/10.1103/PhysRevB.93.235447
349. N. Levy, S.A. Burke, K.L. Meaker, M. Panlasigui, A. Zettl, F. Guinea, A.H.C. Neto, M.F. Crommie, Science **329**(5991), 544 (2010). https://doi.org/10.1126/science.1191700
350. K. Mnasri, B. Jeevanesan, J. Schmalian, Phys. Rev. B **92**, 134423 (2015). https://doi.org/10.1103/PhysRevB.92.134423
351. N. Prasai, B.A. Trump, G.G. Marcus, A. Akopyan, S.X. Huang, T.M. McQueen, J.L. Cohn, Phys. Rev. B **95**, 224407 (2017). https://doi.org/10.1103/PhysRevB.95.224407
352. C. Ulloa, A. Tomadin, J. Shan, M. Polini, B.J. van Wees, R.A. Duine, Phys. Rev. Lett. **123**, 117203 (2019). https://doi.org/10.1103/PhysRevLett.123.117203
353. J.F. Rodriguez-Nieva, D. Podolsky, E. Demler (2018). https://doi.org/10.48550/arXiv.1810.12333
354. C. Zu, F. Machado, B. Ye, S. Choi, B. Kobrin, T. Mittiga, S. Hsieh, P. Bhattacharyya, M. Markham, D. Twitchen, A. Jarmola, D. Budker, C.R. Laumann, J.E. Moore, N.Y. Yao, Nature **597**, 45 (2021). https://doi.org/10.1038/s41586-021-03763-1
355. E. Ilievski, J. De Nardis, B. Wouters, J.S. Caux, F.H.L. Essler, T. Prosen, Phys. Rev. Lett. **115**, 157201 (2015). https://doi.org/10.1103/PhysRevLett.115.157201
356. T. Langen, S. Erne, R. Geiger, B. Rauer, T. Schweigler, M. Kuhnert, W. Rohringer, I.E. Mazets, T. Gasenzer, J. Schmiedmayer, Science **348**(6231), 207 (2015). https://doi.org/10.1126/science.1257026
357. O.A. Castro-Alvaredo, B. Doyon, T. Yoshimura, Phys. Rev. X **6**, 041065 (2016). https://doi.org/10.1103/PhysRevX.6.041065
358. B. Bertini, M. Collura, J. De Nardis, M. Fagotti, Phys. Rev. Lett. **117**, 207201 (2016). https://doi.org/10.1103/PhysRevLett.117.207201
359. B. Bertini, F. Heidrich-Meisner, C. Karrasch, T. Prosen, R. Steinigeweg, M. Žnidarič, Rev. Mod. Phys. **93**, 025003 (2021). https://doi.org/10.1103/RevModPhys.93.025003
360. J.S. Caux, B. Doyon, J. Dubail, R. Konik, T. Yoshimura, SciPost Phys. **6**, 70 (2019). https://doi.org/10.21468/SciPostPhys.6.6.070
361. M. Schemmer, I. Bouchoule, B. Doyon, J. Dubail, Phys. Rev. Lett. **122**, 090601 (2019). https://doi.org/10.1103/PhysRevLett.122.090601
362. J. Lopez-Piqueres, B. Ware, S. Gopalakrishnan, R. Vasseur, Phys. Rev. B **103**, L060302 (2021). https://doi.org/10.1103/PhysRevB.103.L060302
363. Y. Tserkovnyak, J. Appl. Phys. **124**(19), 190901 (2018). https://doi.org/10.1063/1.5054123
364. John Kerr, LL.D., The London, Edinburgh, and Dublin Philosophical Magazine and Journal of Science **3**(19), 321 (1877). https://doi.org/10.1080/14786447708639245
365. T. Van Mechelen, W. Sun, Z. Jacob, Nat. Commun. **12**, 4729 (2021). https://doi.org/10.1038/s41467-021-25097-2
366. Y. Tserkovnyak, J. Zou, Phys. Rev. Research **1**, 033071 (2019). https://doi.org/10.1103/PhysRevResearch.1.033071

367. V. Galitski, M. Kargarian, S. Syzranov, Phys. Rev. Lett. **121**, 176603 (2018). https://doi.org/10.1103/PhysRevLett.121.176603
368. K. Hattori, Y. Hirono, H.U. Yee, Y. Yin, Phys. Rev. D **100**, 065023 (2019). https://doi.org/10.1103/PhysRevD.100.065023
369. C. Copetti, K. Landsteiner, Phys. Rev. B **99**, 195146 (2019). https://doi.org/10.1103/PhysRevB.99.195146
370. R. Toshio, K. Takasan, N. Kawakami, Phys. Rev. Res. **2**, 032021 (2020). https://doi.org/10.1103/PhysRevResearch.2.032021
371. E.H. Hasdeo, J. Ekström, E.G. Idrisov, T.L. Schmidt, Phys. Rev. B **103**, 125106 (2021). https://doi.org/10.1103/PhysRevB.103.125106
372. M. Moore, P. Surówka, V. Juričcć, B. Roy, Phys. Rev. B **101**, 161111 (2020). https://doi.org/10.1103/PhysRevB.101.161111
373. N.N. Fimin, V.M. Chechetkin, Comput. Math. Math. Phys. **58**, 449 (2018). https://doi.org/10.1134/S0965542518030053
374. A.G. Aksenov, A.V. Babakov, V.M. Chechetkin, Comput. Math. Math. Phys. **58**, 1287 (2018). https://doi.org/10.1134/S096554251808002X
375. I.L. Aleiner, B.L. Altshuler, M.E. Gershenson, Waves Random Media **9**(2), 201 (1999). https://doi.org/10.1088/0959-7174/9/2/308
376. B.L. Altshuler, P.A. Lee, R.A. Webb (eds.), *Mesoscopic phenomena in solids* (North-Holland, New York, 1991)
377. B.N. Narozhny, I.L. Aleiner, Phys. Rev. Lett. **84**, 5383 (2000). https://doi.org/10.1103/PhysRevLett.84.5383
378. B.N. Narozhny, I.L. Aleiner, A. Stern, Phys. Rev. Lett. **86**, 3610 (2001). https://doi.org/10.1103/PhysRevLett.86.3610
379. A.K. Geim, I.V. Grigorieva, Nature **499**, 419 (2013). https://doi.org/10.1038/nature12385
380. E.G. Mishchenko, B.I. Halperin, Phys. Rev. B **68**, 045317 (2003). https://doi.org/10.1103/PhysRevB.68.045317
381. T.S. Nunner, N.A. Sinitsyn, M.F. Borunda, V.K. Dugaev, A.A. Kovalev, A. Abanov, C. Timm, T. Jungwirth, J.i. Inoue, A.H. MacDonald, J. Sinova, Phys. Rev. B **76**, 235312 (2007). https://doi.org/10.1103/PhysRevB.76.235312
382. N.A. Sinitsyn, J. Phys. Condens. Matter **20**, 023201 (2008). https://doi.org/10.1088/0953-8984/20/02/023201
383. I. Žutić, J. Fabian, S. Das Sarma, Rev. Mod. Phys. **76**, 323 (2004). https://doi.org/10.1103/RevModPhys.76.323
384. J. Sinova, S.O. Valenzuela, J. Wunderlich, C.H. Back, T. Jungwirth, Rev. Mod. Phys. **87**, 1213 (2015). https://doi.org/10.1103/RevModPhys.87.1213